

MODELING GALACTIC CHEMICAL EVOLUTION IN COSMOLOGICAL
SIMULATIONS

By

Carolyn Cynthia Peruta

A DISSERTATION

Submitted to
Michigan State University
in partial fulfillment of the requirements
for the degree of

Astrophysics and Astronomy - Doctor of Philosophy

2013

ABSTRACT

MODELING GALACTIC CHEMICAL EVOLUTION IN COSMOLOGICAL SIMULATIONS

By

Carolyn Cynthia Peruta

The most fundamental challenges to models of galactic chemical evolution (GCE) are uncertainties in the basic inputs, including the properties of the stellar initial mass function (IMF), stellar nucleosynthetic yields, and the rate of return of mass and energy to the interstellar and intergalactic medium by Type Ia and II supernovae and stellar winds. In this dissertation, we provide a critical examination of widely available stellar nucleosynthetic yield data, with an eye toward modeling GCE in the broad scope of cosmological hydrodynamical simulations. We examine the implications of uncertain inputs for the Galactic stellar IMF, and nucleosynthetic yields from stellar-evolution calculations, on our ability to ask detailed questions regarding the observed Galactic chemical-abundance patterns. We find a marked need for stellar feedback data from stars of initial mass 8 to 12 M_{\odot} and above 40 M_{\odot} , and for initial stellar metallicities above and below solar, $Z_{\odot}=0.02$. We find the largest discrepancies amongst nucleosynthetic yield calculations are due to various groups' treatment of hot bottom burning, formation of the ^{13}C pocket in asymptotic giant-branch (AGB) stars, and details of mass loss, rotation, and convection in all stars. Our model of GCE is used to post-process simulations to explore in greater detail the nucleosynthetic evolution of the stellar populations and interstellar/intergalactic medium, and to compare directly to the chemical abundances of the Milky Way stellar halo and dwarf spheroidal galaxy stellar populations.

Copyright by
CAROLYN CYNTHIA PERUTA
2013

To Grandma. I bet you'd be wearing a dress today.

ACKNOWLEDGMENTS

I am grateful to an army of friends, family, and co-workers for their encouragement and guidance throughout my academic career.

To my advisor, Brian O'Shea, thank you for your unwavering support and invaluable guidance. *Perfection is the enemy of 'good enough'!* Additionally, I'd like to thank those in my research group and thesis committee for your input and suggestions. Thank you Tim Beers, Jason Tumlinson, Brian Crosby, Hendrik Schatz, S.D. Mahanti, and Mark Voit.

To my mentor and advocate, Stephen Pompea, thank you for helping me build such an extraordinary professional network and for providing sage advice these past ten years.

My family has provided a bottomless well of love and support. Thank you Dad and Linda, Mom and Tony. How could I go wrong with amazing parents like you? Without the strength and love of my siblings, I wouldn't be the person I am today. Steph, you taught me patience. Dean, you taught me to hate the middle seat. Tim, you showed me how to fold amazing water balloons. Cheryl, you are a survivor! It takes serious dedication to fight cancer while earning your PhD. You are a true inspiration. To my fluffy sibling, D.O.G. I miss you.

Lastly, I must express undying gratitude to my partner in crime, Chris Richardson. You have been there for me every step of the way these last four years. I cannot wait to see where the future takes us. Also, we have cats. True story.

This work was completed with support in part by the DoE through the Los Alamos National Laboratory Institute for Geophysics and Planetary Physics and in part by NSF grants PHY 02-16783 and PHY 08-22648: Physics Frontiers Center/JINA.

TABLE OF CONTENTS

LIST OF FIGURES	viii
Chapter 1 Introduction	1
1.1 Origin of the Elements	3
1.1.0.1 Big Bang Nucleosynthesis	3
1.1.0.2 Epoch of Nucleosynthesis	4
1.2 Observed Chemical Abundances	7
1.2.1 The Chemical Composition of the Milky Way	10
1.2.1.1 The Metallicity Distribution Function	10
1.2.2 The Chemical Composition of Dwarf Galaxies	12
1.3 Qualitative Models of GCE	14
1.4 Semi-Analytic Models	18
Chapter 2 Current State of Yields	21
2.1 Definitions and Assumptions	23
2.1.1 Stellar Yields	26
2.1.2 Scaled Solar Compositions	27
2.1.3 Metallicity Effects	28
2.2 Yields of Type II Supernovae	29
2.3 Yields of Hypernovae	31
2.4 Yields of Asymptotic Giant-Branch Stars	32
2.4.1 Uncertainties due to the ^{13}C Pocket	34
2.4.2 Uncertainties due to Mass Loss	34
2.4.3 Super AGB stars	35
2.5 Yields of Type Ia Supernovae	36
2.5.1 Progenitors and Model Assumptions	37
2.6 Neutron-Capture Element Yields	37
Chapter 3 Galactic Chemical Evolution Implementation	40
3.1 Element Coverage	41
3.1.1 Primary ISM Coolants	41
3.1.2 The Alpha Elements	42
3.1.3 The Iron-Peak Elements	42
3.1.4 The Neutron-Capture Elements	43
3.2 Initial Mass Function	43
3.3 Stellar Lifetimes	47
3.4 Stellar Ejecta	47
3.5 Type Ia Supernovae Rates	50

Chapter 4	Analysis of a Simple Stellar Population	54
4.1	Simple Stellar Population Example	54
4.1.1	Milky Way and Dwarf Galaxy Models	61
4.2	Variation in the Initial Mass Function	61
4.2.1	Varying the Characteristic Mass	66
4.2.2	Varying the Stellar Yields	73
4.3	Implications for Numerical Models	79
4.3.1	Effects of Coarse Mass Grids	79
4.3.2	Effects of Coarse Metallicity Grids	80
Chapter 5	Post-Processing Cosmological Simulations with Chemical Evolution Models	85
5.1	Simulation Setup	85
5.2	Chemical Enrichment	87
5.3	Halo Supernova Ejection	93
5.3.1	Results	96
Chapter 6	Summary and Future Work	107
Chapter 7	IMF and Yield Variations	110
BIBLIOGRAPHY		129

LIST OF FIGURES

Figure 1.1	Predicted primordial abundances of light elements as a function of the baryon to photon ratio, $\eta_{10} = 10^{10} n_B/n_\gamma = 274 \Omega_b h^2$. The widths of the bands reflect the uncertainties in reaction rates. Figure reprinted from Steigman (2005). <u>For interpretation of the references to color in this and all other figures, the reader is referred to the electronic version of this dissertation.</u>	6
Figure 1.2	Estimated abundances, $A(\text{El})$, of the chemical elements in the Solar system as a function of their atomic number, Z . Data from Lodders (2003).	9
Figure 1.3	Figure from Beers et al. (2005) showing the observed Metallicity Distribution Functions for the HK survey (left panel) and the HES (right panel) candidate metal-poor stars. Bins are 0.2 dex in width. The numbers of stars with $[\text{Fe}/\text{H}] < 2.0$ and $[\text{Fe}/\text{H}] < 3.0$ in these surveys are listed individually. The selection efficiency of VMP stars in the HES is clearly higher than that of the HK survey.	11
Figure 1.4	Schematic merger tree showing structure growth of halos by mergers and accretion. Each box represents a halo “particle” which is assigned a value for redshift of entry, z_{entry} , and redshift of the host halo z_{host} . Each of these particles is then painted with information about feedback. The chemical evolution driver starts forward from the earliest subhalos, merging them at branch points and evolving them between mergers. Figure from Tumlinson (2010).	20
Figure 2.1	Availability of stellar nucleosynthetic yields, as a function of stellar metal fraction and initial stellar mass.	22
Figure 2.2	Direct comparison of widely used stellar nucleosynthetic yield sets for AGB stars, plotted as a function of initial stellar mass at Solar metallicity. The yields of carbon vary widely between different groups, owing to the uncertainties inherent in treatment of the ^{13}C pocket and the third dredge-up. The yields of SNII vary by up to an order of magnitude between groups due to uncertainties in explosion mechanisms and treatment of rotation and mixing.	24

Figure 2.3	Direct comparison of widely used stellar nucleosynthetic yield sets for SNIa, plotted as a function of initial stellar mass at Solar metallicity. The yields of carbon vary widely between different groups, owing to the uncertainties inherent in treatment of the ^{13}C pocket and the third dredge-up. The yields of SNIa vary by up to an order of magnitude between groups due to uncertainties in explosion mechanisms and treatment of rotation and mixing.	25
Figure 3.1	Seven IMFs with $m_{low} = 0.08 M_{\odot}$ and $m_{high} = 260 M_{\odot}$. All, with the exception of the log-normal function, are empirical fits to the observed stellar population in the local universe. See Section 3.2 for the functional forms.	46
Figure 3.2	Stellar lifetime (duration of H- and He-burning phases) for stellar evolution models with masses between 0.6 and $120 M_{\odot}$ and metallicities $Z = 0.0004$ to 0.05 fit by Raiteri et al. (1996). The lifetime of stars is a strong function of initial stellar mass, and only weakly dependent on stellar metallicity.	48
Figure 3.3	The lifetimes of SNIa are determined by the mass of the main sequence or giant companion to the C-O white dwarf. Here, Type Ia supernovae rates are shown as a function of the mass of the secondary star and its lifetime, plotted for various metallicities. The $Z=0.1 Z_{\odot}$ models is shown as a gray line in each panel for reference.	53
Figure 4.1	Stellar yield of carbon, as a function of time since stellar formation, for various IMFs. The dotted line shows the yield from SNIa, which should be summed with yields from AGB stars and SNIa. Vertical lines are drawn at 12, 8, and $6 M_{\odot}$	56
Figure 4.2	Time-integrated total mass returned to the ISM by a simple stellar population, $Z = 0.02 = Z_{\odot}$, as a function of its age. The feedback model includes mass returned from AGB stars, SNe Ia, SNeII, and the winds from their progenitors assuming two initial mass functions. Stellar yields are obtained from Karakas (2010), Siess (2007), Kobayashi et al. (2006), and Iwamoto et al. (1999).	57
Figure 4.3	Time-integrated total mass returned to the ISM by a simple stellar population, $Z = 0.004 = 0.2 Z_{\odot}$, as a function of its age. The feedback model includes mass returned from AGB stars, SNe Ia, SNeII, and the winds from their progenitors assuming two initial mass functions. Stellar yields are obtained from Karakas (2010), Siess (2007), Kobayashi et al. (2006), and Iwamoto et al. (1999).	58

Figure 4.4	Metallicity, $[\text{Fe}/\text{H}]$ as a function of stellar population age for three IMFs.	59
Figure 4.5	In addition to metals, an SSP ejects energy into the ISM. Here we show the energy feedback from an SSP over the lifetime of the stellar population from AGB stars, SNIa, and SNII. The top row shows the energy feedback calculated from the AGB and SNIa yields of Karakas (2010), Marigo (2001), van den Hoek & Groenewegen (1997) and Iwamoto et al. (1999). while the bottom row shows the SNII feedback calculated from the yields of Kobayashi et al. (2006), Portinari et al. (1998) and Rauscher et al. (2002). Each color corresponds to a different IMF.	60
Figure 4.6	The time derivative of energy feedback from an SSP over the lifetime of the stellar population from AGB stars, SNIa, and SNII. The top row shows the energy feedback calculated from the AGB and SNIa yields of Karakas (2010), Marigo (2001), van den Hoek & Groenewegen (1997) and Iwamoto et al. (1999). while the bottom row shows the SNII feedback calculated from the yields of Kobayashi et al. (2006), Portinari et al. (1998) and Rauscher et al. (2002). Each color corresponds to a different IMF.	62
Figure 4.7	(top) $[\text{Fe}/\text{H}]-[\text{C}/\text{Fe}]$ distribution and (bottom) $[\text{Fe}/\text{H}]-[\text{Mg}/\text{Fe}]$ distribution for our simple stellar population model (red lines) compared with SEGUE dataset (blue circles) of nearly 17,000 nearby stars (Yanny et al., 2009). The SSP model assumes a Kroupa IMF, constant star formation with efficiency, $\epsilon=0.04$, mass outflow from supernovae, and exponentially decreasing primordial gas infall rate, $\tau=12$ Gyr. The red line represents $[\text{X}/\text{Fe}]$ calculated at the end of 14 Gyr for stellar particles with initial $[\text{Fe}/\text{H}]$ ranging from -5 to -1. . .	63
Figure 4.8	The $[\text{X}/\text{Fe}]$ distribution for our simple stellar population model compared with metal poor stars in the MW halo and dwarf galaxies as collected by Frebel (2010) and references therein. The SSP model assumes a Salpeter IMF, Kroupa IMF, Scalo IMF, or Tinsley IMF (black, green, red, magenta respectively) with constant star formation (efficiency, $\epsilon=0.04$), mass outflow from supernovae, and exponentially decreasing primordial gas infall rate, $\tau=12$ Gyr. The red line represents $[\text{X}/\text{Fe}]$ calculated at the end of 14 Gyr for stellar particles with initial $[\text{Fe}/\text{H}]$ ranging from -5 to -1. A blue horizontal line denotes a lower limit for neutron capture abundances from the SSP model. . .	64
Figure 4.9	Star formation history of known satellite galaxies of MW within $1 h^{-1}$ Mpc of the host as parameterized by Orban et al. (2008). . . .	65

Figure 4.10	The characteristic mass, m_c , and mass cut, m_{cut} , between the log-normal and power-law function of the Chabrier IMF is varied, while keeping the overall normalization of the IMF constant. We explore the implications of varying these values on the IMF-weighted yields of AGB stars.	68
Figure 4.11	The first panel displays IMF forms of Figure 4.10 in the mass range of AGB stars. All IMFs are normalized to $1 M_\odot$ in the range 0.08 to $260 M_\odot$, except for the green lines, which have a lower mass limit of $1 M_\odot$. When the AGB stellar yields of Karakas (2010) are weighted with each IMF, we see variation in stellar ejecta up to 0.5 dex. . . .	69
Figure 4.12	The first panel displays IMF forms of Figure 4.10 in the mass range of AGB stars. All IMFs are normalized to $1 M_\odot$ in the range 0.08 to $260 M_\odot$, except for the green lines, which have a lower mass limit of $1 M_\odot$. When the cumulative AGB stellar yields of Karakas (2010) are weighted with each IMF, we see significant variations in the chemical history. See Figure 4.11 for the legend.	70
Figure 4.13	The first panel displays IMF forms of Figure 4.10 in the mass range of SNII. All IMFs are normalized to $1 M_\odot$ in the range 0.08 to $260 M_\odot$, except for green lines, which have a lower mass limit of $1 M_\odot$. When the SNII stellar yields of Rauscher et al. (2002) are weighted with each IMF, we see variation in stellar ejecta up to 1.0 dex. See Figure 4.11 for the legend.	71
Figure 4.14	The first panel displays IMF forms of Figure 4.10 in the mass range of SNII. All IMFs are normalized to $1 M_\odot$ in the range 0.08 to $260 M_\odot$, except for the green lines, which have a lower mass limit of $1 M_\odot$. When the SNII stellar yields of Rauscher et al. (2002) are weighted with each IMF, we see significant variations in the chemical history. See Figure 4.11 for the legend.	72
Figure 4.15	The history of $[C/Fe]$, $[N/Fe]$, $[O/Fe]$, and $[Mg/Fe]$ for two distinct IMFs. The “local” IMF is the Chabrier IMF with the low characteristic mass of $0.079 M_\odot$, while the “high-mass” IMF has a characteristic mass of $2.0 M_\odot$	74

Figure 4.16	Each frame shows a side-by-side comparison of IMF-weighted Carbon yields from two sources, Karakas (2010) and Marigo (2001). First two panels show one yield source for all 5 choices of IMF. Rows 2 through 6 show each yield source overplotted for a single IMF choice. The shaded region denotes the spread of ejected mass of the corresponding yield source due to IMF choice. If the spread due to IMF choice is larger than the spread between two yield sources, we may be able to discern between IMFs from observations. If the yield source spread is larger than the IMF spread, yield uncertainties make it impossible to extract the formation environment from observations. See Section 3.2 for the functional forms.	75
Figure 4.17	Same as Figure 4.16, but for the SNII yields of Kobayashi et al. (2006), Portinari et al. (1998), and Rauscher et al. (2002)	76
Figure 4.18	Each frame shows a side-by-side comparison of IMF-weighted Nitrogen yields from two sources, Karakas (2010) and Marigo (2001). First two panels show one yield source for all 5 choices of IMF. Rows 2 through 6 show each yield source overplotted for a single IMF choice. The shaded region denotes the spread of ejected mass of the corresponding yield source due to IMF choice. If the spread due to IMF choice is larger than the spread between two yield sources, we may be able to discern between IMFs from observations. If the yield source spread is larger than the IMF spread, yield uncertainties make it impossible to extract the formation environment from observations. See Section 3.2 for the functional forms.	77
Figure 4.19	Same as Figure 4.16, but for the SNII Nitrogen yields of Kobayashi et al. (2006), Portinari et al. (1998), and Rauscher et al. (2002) . . .	78
Figure 4.20	An illustration of the problem of coarse mass grids with Nitrogen yield data. When elements are only ejected at specific intervals (e.g., when a $10 M_{\odot}$ star dies, then when a $15 M_{\odot}$ star dies), there are regions in time where mass should be ejected, but is ignored.	81
Figure 4.21	An illustration of the problem of coarse mass grids with Carbon yield data. When elements are only ejected at specific intervals (e.g., when a $10 M_{\odot}$ star dies, then when a $15 M_{\odot}$ star dies), there are regions in time where mass should be ejected, but is ignored.	82

Figure 4.22	The top panel shows the integrated chemical history of carbon, nitrogen, and oxygen over the course of a simple stellar population lifetime. The solid red line shows the chemical history using the full set of available yields for AGB, SNII, and SNIa stars while the blue dashed line is the same calculation performed with the yield data degraded by 50 percent. The bottom panel shows the fractional change between the two calculations. A negative change means a net over-production of the element due to smoothing over the degraded data, while a positive change means a net under-production of the element.	83
Figure 5.1	The global star formation rate of Pop II (blue, solid) and Pop III (red, dashed) stars in the Enzo simulation.	88
Figure 5.2	Temperature for a halo with intense star formation (top) and low star formation (bottom) at $z \approx 7$.	89
Figure 5.3	Density for a halo with intense star formation (top) and low star formation (bottom) at $z \approx 7$.	90
Figure 5.4	Metallicity for a halo with intense star formation (top) and low star formation (bottom) at $z \approx 7$.	91
Figure 5.5	[Fe/H]-[Mg/Fe] distribution of the entire stellar mass in all halos in the simulation at $z = 10$ for the fiducial model with a Salpeter IMF and SFE=0.04. The central panels are the mass-weighted stellar distribution in [Fe/H]-[Mg/Fe] space. White regions have no stellar mass, gray regions have a small, non-zero amount of stellar mass, while red has more stellar mass, and blue is the most common combination of [Fe/H] and [Mg/Fe]. The top and right panels show the distribution of the stellar mass in only [Fe/H] (top) and [Mg/Fe] (right), and share the same axes values as the central panel. SEGUE data is plotted in grayscale contours over the model prediction.	97
Figure 5.6	Same as figure 5.5 but for [C/Fe].	98

Figure 5.7	[Fe/H]-[Mg/Fe] distribution of the entire stellar mass in all halos in the simulation at $z = 10$ for the fiducial model with a Kroupa IMF and $SFE=0.04$. The central panels are the mass-weighted stellar distribution in [Fe/H]-[Mg/Fe] space. White regions have no stellar mass, gray regions have a small, non-zero amount of stellar mass, while red has more stellar mass, and blue is the most common combination of [Fe/H] and [Mg/Fe]. The top and right panels show the distribution of the stellar mass in only [Fe/H] (top) and [Mg/Fe] (right), and share the same axes values as the central panel. SEGUE data is plotted in grayscale contours over the model prediction.	101
Figure 5.8	Same as figure 5.7 but for [C/Fe].	102
Figure 5.9	Same as figure 5.5 but for a Chabrier IMF.	104
Figure 5.10	Same as figure 5.9 but for [C/Fe]	105
Figure 7.1	Each frame shows a side-by-side comparison of IMF-weighted Hydrogen yields from two sources, Karakas (2010) and Marigo (2001). First two panels show one yield source for all 5 choices of IMF. Rows 2 through 6 show each yield source overplotted for a single IMF choice. The shaded region denotes the spread of ejected mass of the corresponding yield source due to IMF choice. If the spread due to IMF choice is larger than the spread between two yield sources, we may be able to discern between IMFs from observations. If the yield source spread is larger than the IMF spread, yield uncertainties make it impossible to extract the formation environment from observations. See Section 3.2 for the functional forms.	111
Figure 7.2	Each frame shows a side-by-side comparison of IMF-weighted Oxygen yields from two sources, Karakas (2010) and Marigo (2001). First two panels show one yield source for all 5 choices of IMF. Rows 2 through 6 show each yield source overplotted for a single IMF choice. The shaded region denotes the spread of ejected mass of the corresponding yield source due to IMF choice. If the spread due to IMF choice is larger than the spread between two yield sources, we may be able to discern between IMFs from observations. If the yield source spread is larger than the IMF spread, yield uncertainties make it impossible to extract the formation environment from observations. See Section 3.2 for the functional forms.	112
Figure 7.3	Same as Figure 7.1, but for the SNII Hydrogen yields of Kobayashi et al. (2006), Portinari et al. (1998), and Rauscher et al. (2002) . . .	113

Figure 7.4	Same as Figure 7.1, but for the SNII Oxygen yields of Kobayashi et al. (2006), Portinari et al. (1998), and Rauscher et al. (2002) . . .	114
Figure 7.5	Same as Figure 7.1, but for the SNII Magnesium yields of Kobayashi et al. (2006), Portinari et al. (1998), and Rauscher et al. (2002) . . .	115
Figure 7.6	Same as Figure 7.1, but for the SNII Calcium yields of Kobayashi et al. (2006), Portinari et al. (1998), and Rauscher et al. (2002) . . .	116
Figure 7.7	Same as Figure 7.1, but for the SNII Iron yields of Kobayashi et al. (2006), Portinari et al. (1998), and Rauscher et al. (2002)	117
Figure 7.8	Each frame shows a side-by-side comparison of integrated history from Hydrogen yields from two sources, Karakas (2010) and Marigo (2001). First two panels show one yield source for all 5 choices of IMF. Rows 2 through 6 show each yield source overplotted for a single IMF choice. See Section 3.2 for the functional forms.	118
Figure 7.9	Each frame shows a side-by-side comparison of integrated history from Carbon yields from two sources, Karakas (2010) and Marigo (2001). First two panels show one yield source for all 5 choices of IMF. Rows 2 through 6 show each yield source overplotted for a single IMF choice. See Section 3.2 for the functional forms.	119
Figure 7.10	Each frame shows a side-by-side comparison of integrated history from Nitrogen yields from two sources, Karakas (2010) and Marigo (2001). First two panels show one yield source for all 5 choices of IMF. Rows 2 through 6 show each yield source overplotted for a single IMF choice. See Section 3.2 for the functional forms.	120
Figure 7.11	Each frame shows a side-by-side comparison of integrated history from Oxygen yields from two sources, Karakas (2010) and Marigo (2001). First two panels show one yield source for all 5 choices of IMF. Rows 2 through 6 show each yield source overplotted for a single IMF choice. See Section 3.2 for the functional forms.	121
Figure 7.12	Same as Figure 7.8, but for the SNII Hydrogen yields of Kobayashi et al. (2006), Portinari et al. (1998), and Rauscher et al. (2002) . . .	122
Figure 7.13	Same as Figure 7.1, but for the SNII Carbon yields of Kobayashi et al. (2006), Portinari et al. (1998), and Rauscher et al. (2002)	123
Figure 7.14	Same as Figure 7.1, but for the SNII Nitrogen yields of Kobayashi et al. (2006)	124

Figure 7.15	Same as Figure 7.1, but for the SNII Oxygen yields of Kobayashi et al. (2006), Portinari et al. (1998), and Rauscher et al. (2002) . . .	125
Figure 7.16	Same as Figure 7.1, but for the SNII Magnesium yields of Kobayashi et al. (2006), Portinari et al. (1998), and Rauscher et al. (2002) . . .	126
Figure 7.17	Same as Figure 7.1, but for the SNII Calcium yields of Kobayashi et al. (2006), Portinari et al. (1998), and Rauscher et al. (2002) . . .	127
Figure 7.18	Same as Figure 7.1, but for the SNII Iron yields of Kobayashi et al. (2006), Portinari et al. (1998), and Rauscher et al. (2002)	128

Chapter 1

Introduction

Understanding galaxy formation and evolution is among the most pressing challenges in astrophysics. In the last decade, projects such as the Sloan Digital Sky Survey (SDSS; York et al. 2000) and the Hubble Ultra Deep Field (Williams et al., 1996) have provided a wealth of observational data on the nature of galaxy populations over the last thirteen billion years of cosmic time – surveys that are complemented by the vast quantities of data that are available for the Milky Way, its satellites, and other galaxies of the Local Group. These surveys, such as the Sloan Extension for Galactic Understanding and Exploration (SEGUE; Yanny et al. 2009), the Radial Velocity Experiment (RAVE; Steinmetz 2003), the Apache Point Observatory Galactic Evolution Experiment (APOGEE; Allende Prieto et al. 2008), the Pan-Andromeda Archeological Survey (PAndAs; McConnachie et al. 2009), and others, include information on the chemical content of individual stars and stellar populations in the Milky Way and Andromeda galaxies. This level of detail allows one to break the degeneracy between stellar metallicity and age, providing a rough chronology of the chemical evolution of local stellar systems. Fully exploiting the available observational data requires cutting-edge models for galactic chemical evolution (GCE), motivated by detailed stellar evolution calculations, and likely requires the use of cosmological simulations that include hydrodynamics, radiative cooling and heating, and prescriptions for star formation, feedback, and the mixing of metal-enriched gas into later generations of stars. With such sophisticated

calculations, one could hope to probe the formation and evolution of the Milky Way and its neighboring galaxies in great detail, and gain invaluable insights into the behavior of galaxies in general. The most fundamental challenge to GCE models are uncertainties in the basic inputs, including the properties of the stellar initial mass function (IMF), stellar nucleosynthetic yields, and the rate of return of mass and energy to the interstellar and intergalactic medium by Type Ia and II supernovae and stellar winds. These observational and theoretical uncertainties limit our ability to use chemical-evolution models to ask basic questions about galactic evolution, e.g., the variation of the stellar IMF over time, and from galaxy to galaxy. Identifying the most important uncertainties is an important step toward identifying and limiting them, and thus improving the predictive capabilities of the models.

A recent study by Romano et al. (2010) quantified uncertainties in chemical-evolution models due to choices of stellar nucleosynthetic yields, and attribute key discrepancies between various groups' calculations to six model assumptions or choices. These attributes are: (1) the adopted location of mass cuts in models of type II supernova explosions, (2) the adopted strength and extent of hot-bottom burning in asymptotic giant-branch stars, (3) the omission of rotation on the chemical composition of stellar surfaces, (4) the adopted mass-loss rates, (5) the adopted nuclear-reaction rates, and (6) the treatment of convection. We repeat the same yield comparisons of Romano et al. (2010) within a cosmological simulation, rather than a two-infall disk chemical-evolution model, as they adopted, and extend our analysis to models of simple stellar populations. The unique challenges for the inclusion of GCE in cosmological simulations require that we expand the discussion of yield uncertainties to include coverage of multiple initial stellar metallicities and stellar masses.

In this dissertation, I present a chemical evolution model that includes the feedback of mass, metals, and energy from a stellar population with an arbitrary IMF and metallicity.

Using this model, we jointly examine uncertainties in the observed Galactic stellar IMF and nucleosynthetic yields from stellar-evolution calculations, with an eye toward understanding the degeneracy between the theoretical and observational uncertainties (and thus our ability to ask detailed questions about galactic evolution using chemical probes).

The remainder of Chapter 1 introduces the general concepts of galactic chemical evolution along with historical context and motivation. Chapter 2 explores the current state of stellar nucleosynthetic yields from various literature sources for asymptotic giant branch stars and super asymptotic giant branch stars, type Ia supernovae, and type II supernovae. Chapter 3 details the process of implementing a model of galactic chemical evolution in cosmological simulation and includes information on all input parameters. Chapter 4 contains results from this implementation in a scaffold of test cases including simple stellar populations, isolated galaxies, and models for the Milky Way and its dwarf galaxy satellites. In Chapter 5 an Enzo cosmological simulation is post-processed to include chemical evolution of several galaxies. Parts of Chapters 2 through 4 have been submitted as Peruta et al. (2013; in review) and Chapter 5 will be submitted as Crosby, Peruta, et al. (in prep).

1.1 Origin of the Elements

1.1.0.1 Big Bang Nucleosynthesis

Primordial nucleosynthesis provides a unique opportunity to test the assumptions of the standard model BBN. The pertinent era of the Big Bang for the formation of light elements is known as the era of nucleosynthesis, which spans from .0001 seconds to 3 minutes. This time period describes a less energetic time when the first subatomic structures are formed in the Universe. Since temperature are still relatively high, most of the nuclei break apart

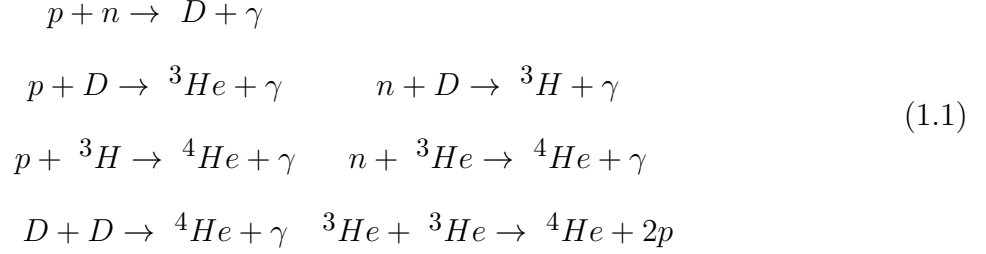
soon after formation. However, by the five minute mark, the matter forms into hydrogen, helium, deuterium, and trace amounts of lithium. This fusion establishes the basic chemical composition of the Universe today. The era ended due to the expansion of the Universe, even though the temperature, at 10^9 K, is still high enough for fusion to occur. Following that period was the era of atoms, in which the Universe had cooled and expanded so that nuclei could indeed hold onto electrons, and photons were now more freely moving. These newly freed photons can still be seen today as part of the CMB which has been mapped by WMAP (Bennett et al., 2003). During this time, neutral atoms and the remaining plasma from the earlier stages formed into protogalactic clouds which eventually formed into stars. The end of the era of atoms brings the age of the Universe to 1 billion years, making it the second longest era. The first stars created were made out of only the elements which were formed in the first billion years: hydrogen, helium, and lithium. Since these primordial abundances set up the initial conditions for GCE, it is worthwhile to understand their formation during the epoch of nucleosynthesis.

1.1.0.2 Epoch of Nucleosynthesis

During the nucleosynthesis era, the Universe is a dilute gas of photons, neutrinos, electron-positron pairs, and trace amounts of nucleons with MeV energy scales and Fermi length scales. Boesgaard & Steigman (1985) calculate the number density of blackbody photons as $n_\gamma = 10^{-7.5} T_{MeV}^3 f^{-3}$, which implies a characteristic distance between photons as $l_\gamma \equiv n_\gamma^{-1/3} \approx 300 T_{MeV}^{-1} f$. At high temperatures and in the relativistic limit, the densities of neutrinos and electron positron pairs are close to that of photons, so $l_e \approx l_\nu \approx l_\gamma$. During this era, $0.1 < T_{MeV} < 10$, and the ratio of baryons to photons, $\eta \equiv n_N/n_\gamma$, is approximately 10^{-10} , which shows the characteristic distance between nucleons is $l_N > 10^3 l_\gamma \approx 10^5 T_{MeV}^{-1} f$.

This term, η , is essentially the only free parameter in the epoch of nucleosynthesis and is usually listed with $\eta = 274/10^{10} \Omega_b h^2$ (Kneller & Steigman, 2004). Additionally, this quantity is conserved as the Universe expands, up to and including the present epoch.

Light element formation proceeded according to the following reactions:



As shown, nearly all neutrons were combined with protons to form helium. In a universe with high baryon number densities, there is time for all neutrons to combine into Deuterium nuclei which then form ${}^4\text{He}$ leading to a low Deuterium abundance. A universe with low baryon density would not have the time to complete all stages of helium synthesis resulting in higher abundances of both ${}^3\text{He}$ and D. These elemental abundances are therefore strong indicators of the current baryon density. Furthermore, the trace amounts of Deuterium needed to sustain this reaction could only survive provided the background radiation was less than its binding energy. At 2.23 MeV, this means the temperature must be lower than $2.6 \times 10^9 K$. Since radiation temperature changes as $T_r = T_0(1+z)$, the time at which light elements could form was after 100 seconds. Detailed calculations by Steigman (2005) predict the primordial abundances of H, D, He, and Li as a function of η (see Figure 1.1). Heavier elements could not be synthesized during Big Bang Nucleosynthesis due to the bottleneck of unstable nuclei with atomic number 5 or 8. All heavier elements must be created and released by stars; the formation and feedback of which is the focus of this dissertation.

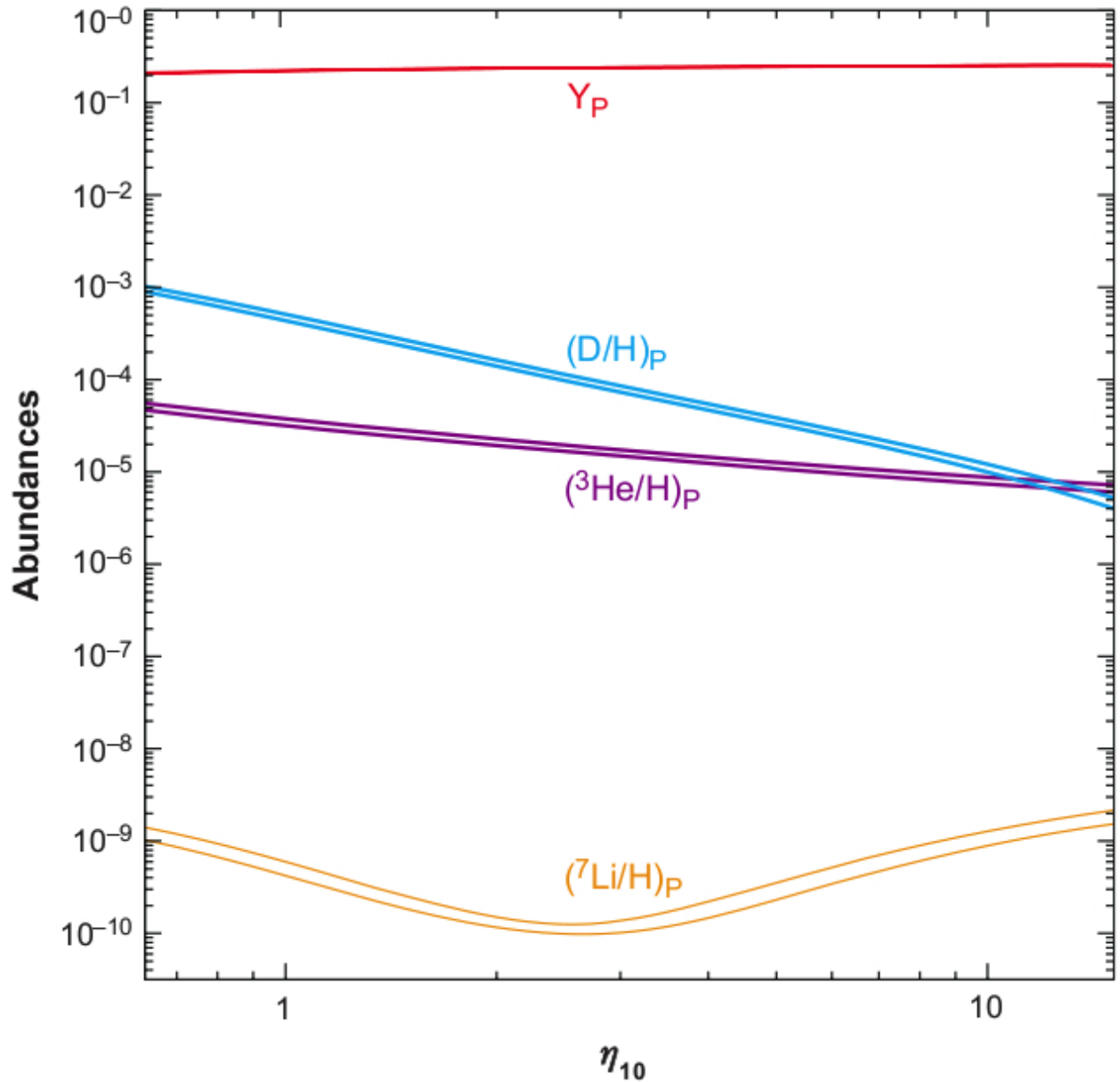


Figure 1.1: Predicted primordial abundances of light elements as a function of the baryon to photon ratio, $\eta_{10} = 10^{10} n_B/n_\gamma = 274 \Omega_b h^2$. The widths of the bands reflect the uncertainties in reaction rates. Figure reprinted from Steigman (2005). For interpretation of the references to color in this and all other figures, the reader is referred to the electronic version of this dissertation.

1.2 Observed Chemical Abundances

The relative abundances of the chemical elements can be measured in a number of astronomical objects primarily using spectroscopic techniques; however, photometric estimations can also be made. These abundances can be measured in stellar photospheres from the strengths of absorption lines. The observed strengths of lines in a stellar spectrum depend on the abundance of the element responsible, on the effective temperature of the star, T_{eff} , on the acceleration due to gravity at its surface, $\log g$, and on small-scale turbulence in the atmosphere of the star, ν_t . All of these parameters can be determined if there is a spectroscopic observation with sufficient signal-to-noise. Equally, abundances can be determined from the strengths of emission lines from interstellar gas, most notably from HII regions.

Before going further there are a few common terms and parameters to define with regards to chemical abundances. In astronomy, we affectionately (yes, there are historical reasons too) refer to all elements heavier than Helium as *metals*. Under this definition even elements such as carbon, oxygen, nitrogen and sulphur are called metals. The term *metallicity* is used for the fraction of elements heavier than Helium and is usually expressed as a fraction by mass. The baryonic mass budget of any object consists of some fraction, by mass, of Hydrogen, Helium, and all other metals. These mass fractions are typically denoted by X, Y, and Z, respectively. Naturally, these fractions sum to 1 ($X+Y+Z\equiv 1$). One can also denote chemical abundances through number of nuclei, typically expressed relative to hydrogen. The most common number fraction quoted in the literature is $N(Fe)/N(H)$, the iron to hydrogen ratio. Furthermore, one can ground these abundance parameters to a familiar object, the Sun. Solar abundances are roughly $X=0.70$, $Y=0.28$, and $Z=0.02$ by mass or 92%, 8.5%, and 0.09% by number (Lodders, 2003). Bracket notation shows abundances of elements relative

to solar. For example, the ratio of Iron to Hydrogen in a star when compared to the Sun is,

$$[Fe/H] = \log_{10} \left(\frac{N(Fe)}{N(H)} \right)_* - \log_{10} \left(\frac{N(Fe)}{N(H)} \right)_{\odot}. \quad (1.2)$$

By definition the value of [Fe/H] is zero for the Sun. A star with 100 times more Iron to Hydrogen than the sun would have an [Fe/H] value of 2. Since it is essentially impossible to determine the exact abundance of every element in a star and Iron is readily observable in many astrophysical environments, we tend to use it as a proxy for total metallicity. For reference, the solar abundances determined by Lodders (2003) are shown in Figure 1.2. This figure plots elements according to their atomic number, Z , rather than atomic mass number, A , against the atomic abundances. Along with the number of neutrons, N , $A=Z+N$. The value for an element, “El”, on the logarithmic astronomical scale is designated as $A(El) = \log \epsilon(El)$. On this scale, the number of H atoms is set to $A(H) = \log n(H) = 12$, so that

$$A(El) = \log \epsilon(El) = \log[n(El)/n(H)] + 12. \quad (1.3)$$

The origin of elemental abundances in this figure were first analyzed in Burbidge et al. (1957) and updated by Woosley et al. (2002). Big Bang Nucleosynthesis is responsible for all the Hydrogen and most of the Helium, while cosmic ray spallation (Reeves, 1970) accounts for the observed abundances of Lithium, Beryllium, and Boron. A minimum occurs in the region of these nuclei because they are easily destroyed in the interiors of stars. Other than spallation, they can only be brought to a stellar surface through convective or meridional mixing. All heavier elements ($A \geq 12$) are produced in stars. Increasingly stronger Coulomb repulsion leads to the decline in abundances with heavier nuclei. Beyond the energetically stable Iron peak at $Z=28$, production of elements must proceed solely through neutron captures.

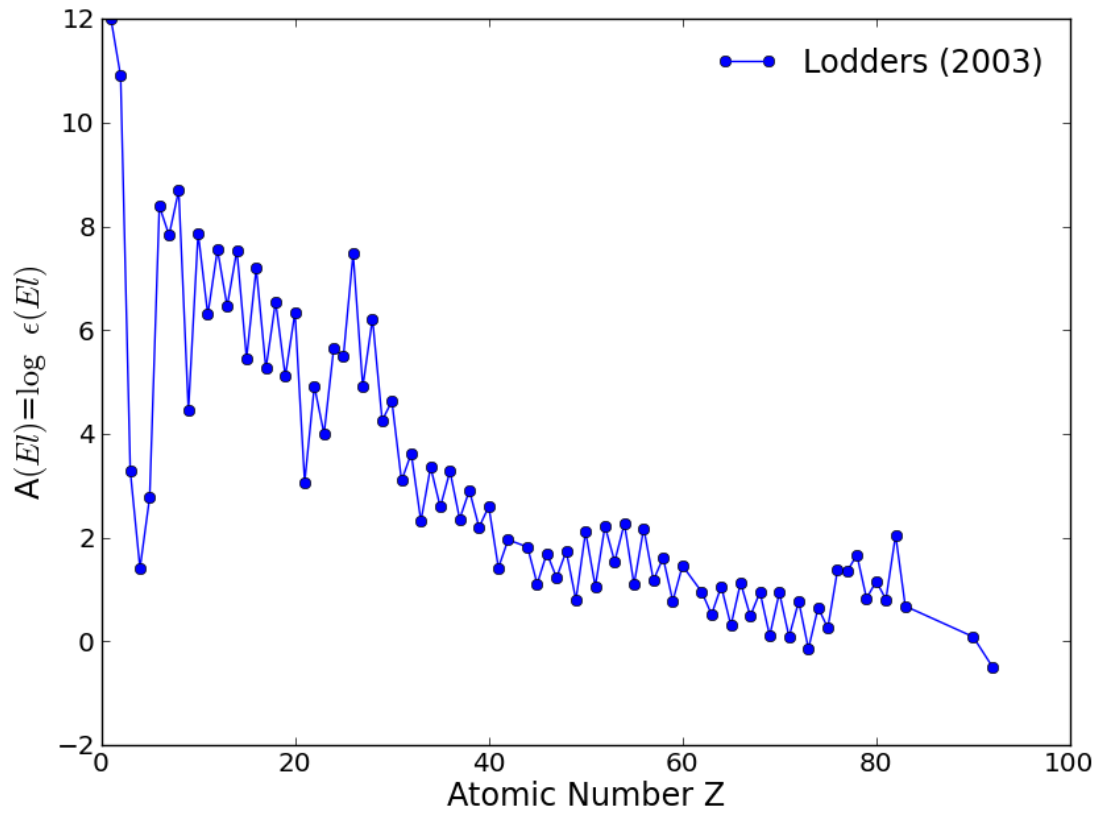


Figure 1.2: Estimated abundances, $A(EI)$, of the chemical elements in the Solar system as a function of their atomic number, Z . Data from Lodders (2003).

1.2.1 The Chemical Composition of the Milky Way

1.2.1.1 The Metallicity Distribution Function

The distribution of stellar metallicities in the Galaxy can be used to test models of galactic chemical evolution. The Simple Model (Schmidt, 1963, see Section 1.3 for more detail) predicts several features for the Metallicity Distribution Function (MDF) of galaxies due to gas outflow, gas infall, star formation rates, and stellar IMF. The MDF for the Milky Way halo determined by Beers et al. (2005) is shown in Figure 1.3. Data for this figure comes from the HK survey of Beers et al. (1985), Beers et al. (1992), and Beers (1999) and the Hamburg/ESO Survey of Christlieb (2003). Due to low sampling rates, it is not possible to precisely determine the shape of the MDF at the lowest metallicities using these surveys. Additionally, due to the survey search techniques, there is a bias introduced for metallicity above $[\text{Fe}/\text{H}]=-2.5$.

Hartwick (1976) find a mean of $[\text{Fe}/\text{H}]\approx-1.6$ for the Galactic halo. This low value could be reproduced assuming gas outflow is high enough that no future generations of stars could further process the material. On the other hand, a later study by Russell & Dopita (1990) looked at the MDF of stars in the Small and Large Magellanic Clouds and found evidence that multiple stellar populations with extended stellar evolution and a low star formation rate caused low $[\text{Fe}/\text{H}]$ for each dwarf galaxy.

Another feature of the Galaxy MDF, the suppression of stars at low metallicity, leads to what is known as the *G-dwarf problem*. Observationally, there are too few metal-poor G-dwarf stars than are expected from a simple model of the galaxy with long-lived stars. G-dwarfs are main sequence stars with sufficiently long lifetimes that they should survive from the earliest times in the evolution of a galaxy to the present day. Current GCE models have

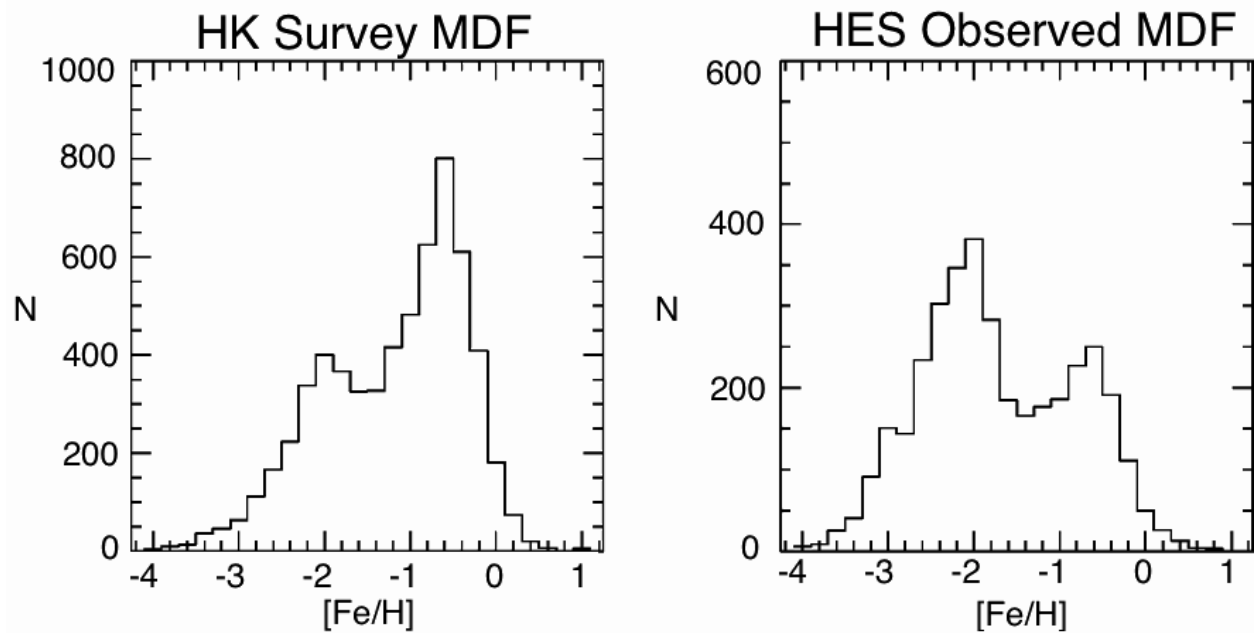


Figure 1.3: Figure from Beers et al. (2005) showing the observed Metallicity Distribution Functions for the HK survey (left panel) and the HES (right panel) candidate metal-poor stars. Bins are 0.2 dex in width. The numbers of stars with $[\text{Fe}/\text{H}] < 2.0$ and $[\text{Fe}/\text{H}] < 3.0$ in these surveys are listed individually. The selection efficiency of VMP stars in the HES is clearly higher than that of the HK survey.

demonstrated that the lack of low-metallicity dwarf stars can be explained if the Galactic halo formed first on a rapid timescale, followed by a slow build-up of the thin disk (e.g. Chiappini, Matteucci & Gratton 1997; Alibes, Labay & Canal 2001; Fenner & Gibson 2003). The excess of metal-poor stars predicted by simple closed-box models can also be avoided by assuming prompt initial enrichment by a first generation of stars having primordial composition. It has also been suggested that there are no very metal-poor stars left because they all had relatively short lifetimes due to low metallicity environments favoring the formation of higher mass stars (Nakamura & Umemura 2001). Lastly, the influence of the initial mass function must be shown in the Galaxy metallicity distribution function since the yield of iron from massive stars and the amount of gas locked up by low mass dwarfs is directly dependent on the numbers of such stars.

1.2.2 The Chemical Composition of Dwarf Galaxies

According to Λ CDM cosmology, the Milky Way's stellar halo must have formed from many smaller stellar systems (Press & Schechter, 1974). During the epoch of inflation the Universe was nearly homogenous with tiny density perturbations imprinted on all scales. As the Universe expanded, these perturbations grew in size and influence by means of gravitational instabilities. This Press-Schechter formalism successfully describes many properties of the dark matter halo population in both simulations of structure formation and observations of halo mass functions (Mo & White, 2002). Eventually, the first gravitationally bound halos formed and then subsequently merged into galaxies, clusters, and the other large scale structures we observe today.

As our nearest galactic neighbors, it is tempting to assume the dwarf galaxies of the Local Group are similar to those proto-galactic halos that merged to form the Milky Way.

All dwarf spheroidal satellites of the Milky Way show evidence of old stellar populations and have low mean metallicities that are on par with the Galactic halo stars (Grebel & Gallagher, 2004). Despite agreement on these two characteristics, present-day dwarf spheroidal galaxies have been ruled out as progenitors of the Galactic halo based on details of their chemical abundance patterns (Pritzl et al., 2005). Stars in dwarf galaxies have a statistically significant underabundance of Mg, Ca, and Ti in comparison to the galactic halo. Overall, the α -element abundances span a range of $0.02 \lesssim [\alpha/\text{Fe}] \lesssim 0.13$ while Milky Way halo field stars have a nearly constant $[\alpha/\text{Fe}] \sim 0.28$ over the same range of $[\text{Fe}/\text{H}]$ (Shetrone et al., 2001). If the star formation in a galaxy proceeds by a series of bursts, rather than constant star formation, then this should lead to clear differences in evolution of the α/Fe ratio. Oxygen is produced primarily in the high-mass stars of negligible lifetimes and ejected by SNe II, while iron is produced in both SNe II and SNe Ia. Stars that form shortly after the interstellar medium has been enriched by SNe II may have enriched $[\alpha/\text{Fe}]$ ratios, while those that form sometime after the SNe Ia contribute will have lower $[\alpha/\text{Fe}]$. Since bursts of star formation allow SNe II to contribute α -elements, and long inactive periods allow SNe Ia to contribute iron, then the total $[\alpha/\text{Fe}]$ ratios in a galaxy should be able to vary over time. The abundance patterns shown in Pritzl et al. (2005) indicate preferential outflow of SNII ejecta from the stellar system.

Helmi et al. (2006) rule out any scenario in which the earliest mergers of dwarf galaxy progenitors build up the galactic halo by examining the metal-poor tail of the metallicity distribution functions. Since stars in this tail are likely to represent the first generation of stars in each population, they are ideal for comparison. Even the dwarf galaxy which best fits the metallicity distribution function, Fornax, has only a fractional probability of 8×10^{-3} that it shares its first generation stars with that of the Milky Way in this study. Helmi

et al. (2006) devise two explanations for the lack of very low metallicity stars in the dwarf galaxies. In the first scenario one the Milky Way could have formed from the collapse of a higher-density fluctuation while the dwarf galaxies formed from a lower-density environment collapsing at a much lower redshift. As a consequence of their smaller potential wells, these dwarf galaxies lose more gas to winds, leading to less efficient star formation. Another possibility is that the IMF could be bimodal with very low mass stars forming early on at low metallicity in the Milky Way. Both of these instances can be modeled with galactic chemical evolution in models that are incorporated into in cosmological simulations, but would require high resolution spectra to confirm observational trends.

1.3 Qualitative Models of GCE

Understanding of some simple models and qualitative concepts of GCE is crucial to interpreting the general trends in abundance that are observed in the Galaxy. The most basic of these models, the Simple Model of Schmidt (1963) and van den Bergh (1995), involves a closed box of some quantity of metal-free gas. This gas undergoes constant star formation with stellar masses distributed according to an initial mass function (IMF). Each stellar generation yields the same mass of metals, which are instantaneously and homogeneously mixed back into the box as fodder for future generations of star formation.

In more general terms, the total mass evolution of any system is given by,

$$\frac{dm}{dt} = [I - O] \tag{1.4}$$

If the system evolves without any inflow or mass loss, the right hand side of the equation

is zero and we have the closed box model mentioned previously. The optional variables, I and O , represent infall of extragalactic material at a rate $I(t)$ and outflow of mass from the system at a rate $O(t)$ respectively.

The evolution of gas mass, $m_G(t)$, of a system is given by:

$$\frac{dm_G}{dt} = -\Psi + E + [I - O] \quad (1.5)$$

where $\Psi(t)$ is the star formation rate (SFR). The negative sign indicates gas is leaving the reservoir to be locked up in stars. $E(t)$ is the rate of feedback in the form of ejected material, given by:

$$E(t) = \int_{M_t}^{M_U} (M_i - M_f) \Psi(t - \tau_M) \Phi(M) dM \quad (1.6)$$

where the star of mass M_i , created at the time $t - \tau_M$, where τ_M is the stellar lifetime, dies at time t (if $\tau_M < t$) and leaves a compact object (white dwarf, neutron star, black hole) of mass M_f . The integral is weighted by the initial mass function of the stars $\Phi(M)$ and the bounds include all stars that are of a mass that is large enough that they will die by time t until an upper mass limit, M_U .

The stellar mass $m_S(t)$ of the system is:

$$m_S = m_{total} - m_G. \quad (1.7)$$

As time goes on, a progressively larger part of the mass of stars is found in the form of compact objects, effectively removing that gas from the system. The mass of element/isotope i in the gas is $m_i = m_G X_i$, where X_i is the element/isotope mass fraction, and its evolution

is given by:

$$\frac{d(m_G X_i)}{dt} = -\Psi X_i + E_i + [IX_{i,I} - OX_{i,O}] \quad (1.8)$$

Star formation at a rate Ψ removes element i from the ISM at a rate ΨX_i , while at the same time stars re-inject in the ISM that element at a rate $E_i(t)$. If infall is assumed, the same element i is added to the system at a rate $IX_{i,I}$, where $X_{i,I}$ is the abundance of nuclide i in the in-falling gas (typically, but not necessarily, assumed to be primordial). If outflow takes place, element i is removed from the system at a rate $OX_{i,O}$ where $X_{i,O}$ is the abundance in the outflowing gas; usually the outflowing gas has the composition of the average ISM, but in some cases it may be assumed to be ejecta from energetic supernovae which leave the system. Additionally, the instantaneous mixing approximation is used. Efficient mixing ensures the ISM is of uniform composition and all stars that form at a given time are of the same composition.

The *rate of ejection of element i by stars* is given by:

$$E_i(t) = \int_{M_t}^{M_U} Y_i(M) \Psi(t - \tau_M) \Phi(M) dM \quad (1.9)$$

where $Y_i(M)$ is the stellar yield, the mass ejected in the form of that element by the star of mass M .

These systems of equations can be solved analytically by adopting the Instantaneous Recycling Approximation (IRA) in which all stars more massive than $1M_\odot$ die immediately (Tinsley, 1980). Assuming that equation 1.5 is set to zero (no infall/outflow), and the IMF is constant in time, the metallicity of the gas, Z , evolves as,

$$Z = Y \ln \frac{M_{tot}}{M_{gas}} \quad (1.10)$$

If we plot the observed metallicity, Z , at different points within galactic disks against the logarithm of the fraction of the local mass density that is in gaseous form, we will obtain a straight line. Conflicting with this rather elegant relationship is the metallicity distribution function discussed earlier in this chapter, which is logarithmic. More complex models of chemical evolution allow inflow and outflow of gas, include time dependent metal return, and relax the constraint of homogenous mixing.

Matteucci (2001) calculated the analytic solution for models with both infall and outflow. With outflow alone, the effective yield decreases over time as,

$$Z = \frac{Y}{1 + \lambda} \ln \left[(1 + \lambda) \frac{M_{tot}}{M_{gas}} - 1 \right] \quad (1.11)$$

where λ is the dimensionless wind parameter characterizing the rate of expelled gas, wind-rate = $\lambda \times \text{SFR}$. If we add a term showing the rate of in falling gas, Λ (again, dimensionless), the analytic solution becomes

$$Z = \frac{Y}{\Lambda} \left[1 - \left((\Lambda - \lambda) - (\Lambda - \lambda - 1) \frac{M_{tot}}{M_{gas}} \right)^{\Lambda / (\Lambda - \lambda - 1)} \right]. \quad (1.12)$$

Matteucci (2001) suggested that an outflow with $\lambda = 8$ as well as a formation of the halo by early infall are necessary to reproduce the observed halo metallicity distribution of the Milky Way. Dwarf galaxies are shown to require higher outflow rates to produce their MDFs (Helmi et al., 2006) .

1.4 Semi-Analytic Models

One-zone models of galactic chemical evolution lack the sophistication necessary to capture all the nuances of structure formation and feedback processes in halos. Cosmological simulations allow for a much larger degree of complexity; however, they can be time consuming and computationally expensive. Semi-analytic models bridge the gap between these two, allowing for rapid exploration of parameter space while still capturing important physical processes. With the GALACTICUS model of Benson (2012) and the ChemTreeN model of Tumlinson (2006), analytic approximations and empirical calibrations are used to represent complex physics. As in other semi-analytic models, structure growth is modeled according to the extended Press-Schechter formalism (Press & Schechter, 1974). The extended Press-Schechter treatment of structure formation begins with a power spectrum of Fourier modes, $P(k)$, that describes the probability distribution of small ($\delta \equiv \rho/\langle\rho\rangle \ll 1$) density fluctuations in the early Universe. From early times these fluctuations grow linearly until $\delta \sim 1$, when the fluctuation enters the nonlinear regime, “turns around” and virializes. The overdensity of turnaround corresponds to a critical linear overdensity, δ_c . This critical density separates regions in the evolving linear field that have collapsed from those that have not. The number density of collapsed regions as a function of mass is given in the Press-Schechter formula,

$$ndM = \sqrt{\frac{2}{\pi}} \frac{\bar{\rho}}{M} \frac{\delta_c(z)}{\sigma^2(M)} \exp\left[-\frac{\delta_c^2(z)}{2\sigma^2(M)}\right] dM, \quad (1.13)$$

where $\bar{\rho}$ is the mean matter density and $\sigma^2(M)$ is the variance of the random field fluctuation. With further manipulations, this formula describes the probability distribution of halos that merge to form larger halos at redshift, z , thereby allowing for the creation of a merger tree for structure growth. This analytically-created merger tree is then decomposed

back to individual halos as some earlier redshift. From this point, one can stochastically assign chemical and mechanical feedback according to assumptions of the stellar initial mass function, star formation rates, and efficiency with which metals are mixed back into the ISM. For a schematic view of this merger tree process, see Figure 1.4. While faster to run, the primary disadvantage of these models is that they involve a significant amount of approximations and assumptions. ChemTreeN now uses N-body simulations which provide both temporal and spatial information about halo mergers (Gómez et al., 2012).

ChemTreeN now uses N-body simulations of structure formation, which provide both temporal and spatial information about halo mergers (Tumlinson 2010; Gomez et al. 2012). While this requires one to perform a cosmological simulation and to generate halo catalogs and merger trees prior to using the ChemTreeN code (as these are taken as inputs to ChemTreeN), the advantages are tremendous – one can predict the positional behavior of stellar populations (e.g., the radial metallicity gradient and variation of the stellar halo, or the metallicity variation between different satellite galaxies).

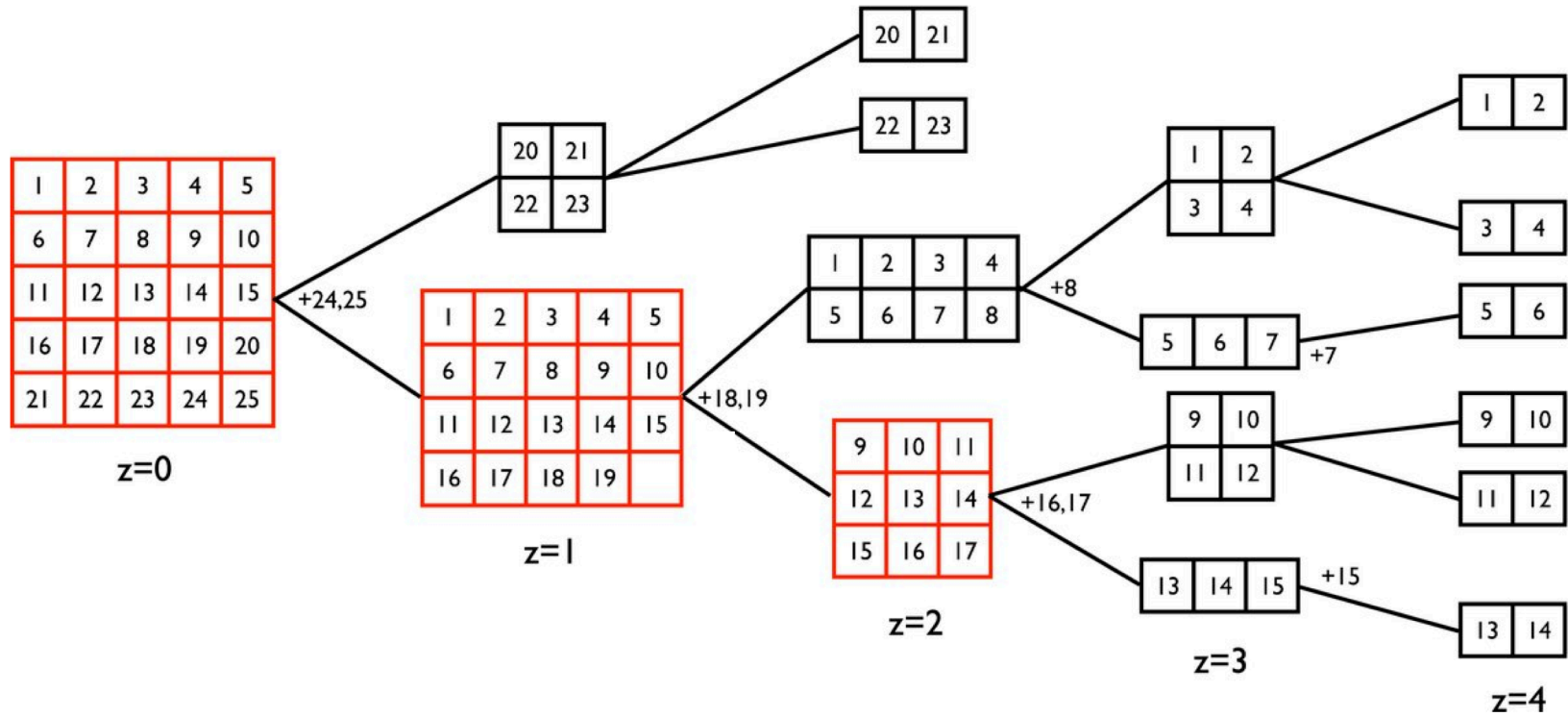


Figure 1.4: Schematic merger tree showing structure growth of halos by mergers and accretion. Each box represents a halo “particle” which is assigned a value for redshift of entry, z_{entry} , and redshift of the host halo z_{host} . Each of these particles is then painted with information about feedback. The chemical evolution driver starts forward from the earliest subhalos, merging them at branch points and evolving them between mergers. Figure from Tumlinson (2010).

Chapter 2

Current State of Yields

In this section, we discuss the various astrophysical sites for producing the heavy elements, and provide a guide to the literature, including sources for the yields for each nucleosynthesis process. Our overall goal is to determine a complete set of yields covering a wide range of masses ($0.08 < M/M_{\odot} < 260$) and metallicities ($10^{-4} < Z < 0.05$), such that a numerical GCE model can follow multiple populations of stars over the age of the Universe. Many of the yield sources discussed here have also been analyzed by Romano et al. (2010). This section serves to recap the key discrepancies between the datasets used by separate groups, with an eye toward selection of a minimum consistent stellar nucleosynthetic-yield set for inclusion in hydrodynamical models. We direct the interested reader to Romano et al. (2010) for a full analysis of yield variations and the nucleosynthetic model assumptions of each research group.

There is a great deal of data at roughly solar metallicity for intermediate-mass stars in the literature; however, stellar nucleosynthetic yields for stars above roughly $20 M_{\odot}$, and for substantially sub- or super-solar metallicity, are sparse. Figure 2.1 clearly shows the large regions of metallicity and initial stellar mass parameter space without available yields. Additional datasets exist, aside from the ones shown here, but they do not substantially fill in the vacant parameter space.

Subtle differences in the included physics and theoretical assumptions can lead to large

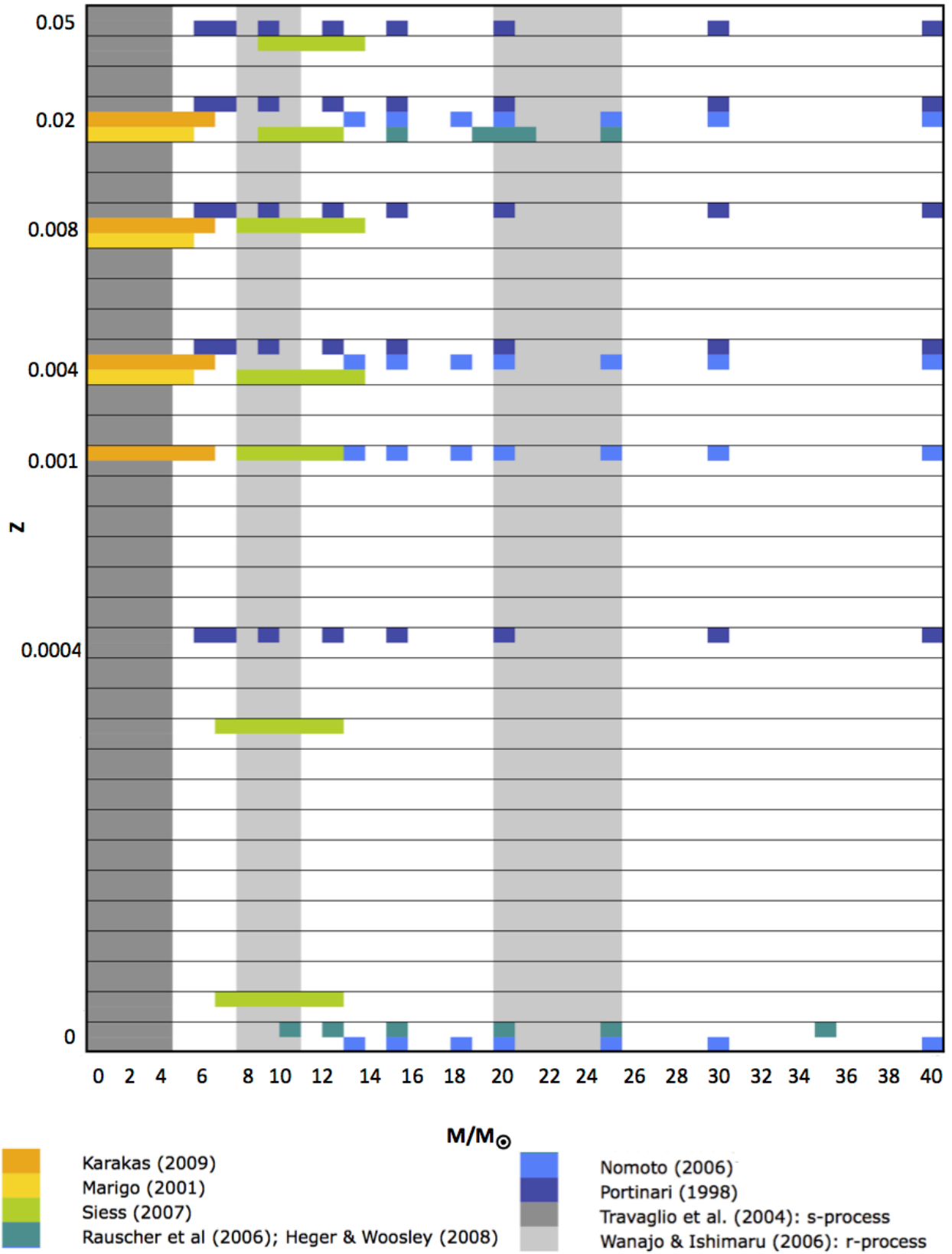


Figure 2.1: Availability of stellar nucleosynthetic yields, as a function of stellar metal fraction and initial stellar mass.

discrepancies in yield calculations. A subset of available yields with similar input physics are shown in Figure 2.2, in order to highlight these differences. In panel A, we compare three sets of asymptotic giant-branch (AGB) stellar yields. Each of these sets covers different ranges in initial mass and metallicity, and have remarkably different carbon yields, which highlight the difficulty in key physical phenomena (see Section 2.4.1). In panel B, we show three sets of type II supernovae yields, with differences up to an order of magnitude at a given initial mass. Details on each of these sets of yields are discussed in Section 2.2 and Section 2.4.

2.1 Definitions and Assumptions

Stellar yields are defined by Tinsley (1980) as the mass fractions of stars which are returned to the ISM in the form of newly produced elements during the entire stellar lifetimes. Each GCE study or stellar nucleosynthesis calculation is performed with internally consistent definitions for terms such as *yield* or *ejected mass*, and the treatment of various physical phenomena. However, different groups often employ different nomenclature and definitions for their terms. For the sake of combining results from multiple research groups into one cohesive set, one must note the assumptions made, and determine transformations from one study to another. As a note, there are many other studies with reported nucleosynthetic yields, however we have omitted those with nearly identical results, those with limited mass and metallicity ranges, and those which lack the important physical processes considered in modern calculations.

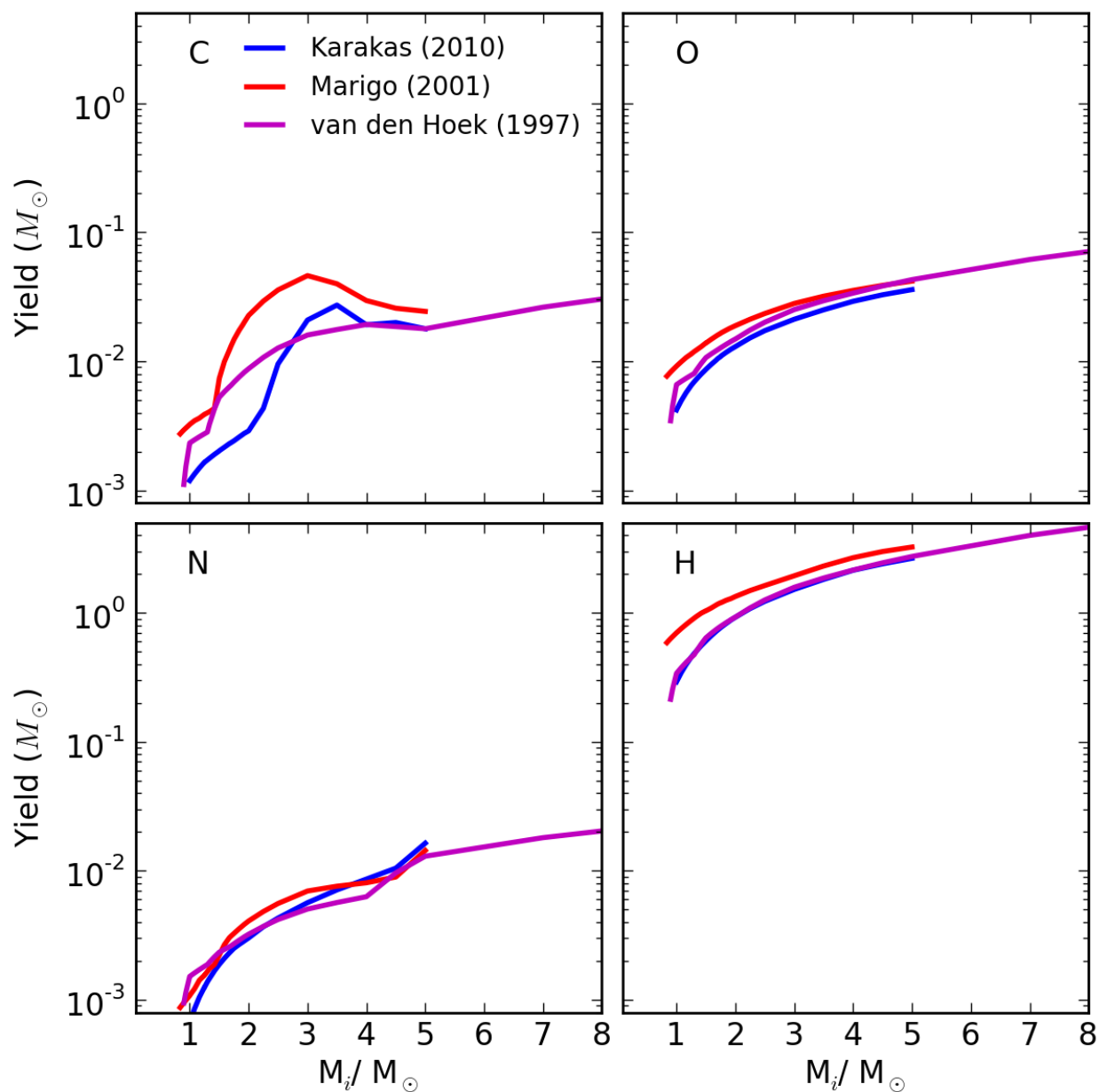


Figure 2.2: Direct comparison of widely used stellar nucleosynthetic yield sets for AGB stars, plotted as a function of initial stellar mass at Solar metallicity. The yields of carbon vary widely between different groups, owing to the uncertainties inherent in treatment of the ^{13}C pocket and the third dredge-up. The yields of SNII vary by up to an order of magnitude between groups due to uncertainties in explosion mechanisms and treatment of rotation and mixing.

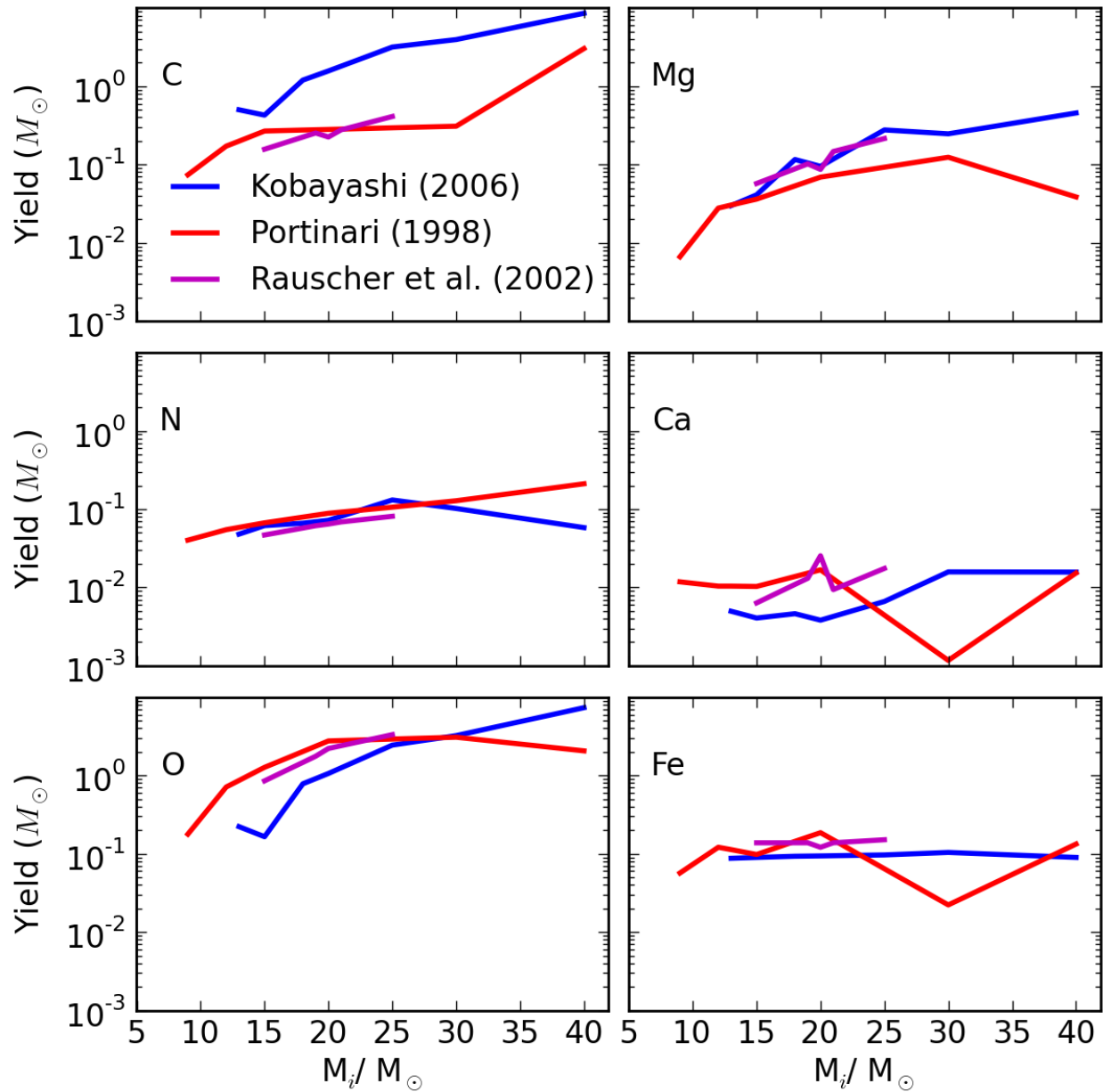


Figure 2.3: Direct comparison of widely used stellar nucleosynthetic yield sets for SNII, plotted as a function of initial stellar mass at Solar metallicity. The yields of carbon vary widely between different groups, owing to the uncertainties inherent in treatment of the ^{13}C pocket and the third dredge-up. The yields of SNII vary by up to an order of magnitude between groups due to uncertainties in explosion mechanisms and treatment of rotation and mixing.

2.1.1 Stellar Yields

Talbot & Arnett (1973) define a stellar production matrix, which describes the production of each isotope in a star of initial mass m . One element of this matrix, $Q_{i,j}(m)$, represents the fraction of stellar mass which was originally present in the form of species j , and is eventually ejected by the star in the form of element i ,

$$Q_{ij} = (m_{ej})_{ij}(m)/mX_j, \quad (2.1)$$

where X_j is the abundance by mass of element j already present in the star when it is formed. The total contribution of a star of mass M to the ejected mass of element i is then

$$(M_{ej})_i = \sum_{j=1,n} Q_{ij}(M)X_jM. \quad (2.2)$$

While this method of tracking the total production minus destruction of species j takes into effect relative abundances, it is a complicated computation, and relies on accurate input abundance patterns. Most yields are given only as a function of metallicity, and are computed for scaled solar-abundance patterns.

Throughout the literature, there are several ways to define the term *yield*, whether it refers to only newly synthesized elements, or takes into account the masses of the total ejecta. In this paper we use yields, $Y_i(M)$, to represent the mass ejected in the form of element i by a star of mass M . These quantities are zero in the case of an isotope that is totally destroyed in stellar interiors, and positive otherwise. Most papers report *net yields*, which represent the newly created mass of nuclide i from a star. Net yields are used in analytical models of GCE, rather than numerical models, where the emphasis is on quantifying newly produced

species rather than following the history of recycled species. The transformation between the two is simply

$$y_i(M) = Y_i(M) - M_{0,i}(M) \quad (2.3)$$

where $M_{0,i}(M)$ is the mass of nuclide i that is originally present in the star, and is ejected unprocessed.

2.1.2 Scaled Solar Compositions

The initial composition of stars used in many stellar-evolution models are scaled solar values.

If, for a given star, we know $[\text{Fe}/\text{H}]$ and if its composition is scaled solar, we have

$$\left(\frac{\chi_j}{\chi_{Fe}} \right)_* = \left(\frac{\chi_j}{\chi_{Fe}} \right)_\odot. \quad (2.4)$$

By summing over the index j ,

$$\left(\frac{Z}{\chi_{Fe}} \right)_* = \left(\frac{Z}{\chi_{Fe}} \right)_\odot. \quad (2.5)$$

By definition,

$$\left[\frac{Fe}{H} \right] = \log \left(\frac{Z}{\chi_H} \right)_* - \log \left(\frac{Z}{\chi_H} \right)_\odot. \quad (2.6)$$

This can be inverted to find Z , as a function of $[\text{Fe}/\text{H}]$,

$$Z_* = 10^{[\text{Fe}/\text{H}]} \chi_* \left(\frac{Z}{\bar{X}} \right)_\odot. \quad (2.7)$$

2.1.3 Metallicity Effects

The formation and evolution of the first generation of stars jump starts the process of chemical evolution with initial conditions set solely by cosmological parameters. The fate of zero metallicity stars is set by the familiar mass ranges determined solely by gravitational considerations and the Chandrasekhar limit. Consequently, nucleosynthetic production within these stars trace the condition of the early universe, signatures of which can still be detected in the most metal-poor stars of our Galaxy. Primordial stars less massive than $8 M_{\odot}$ form white dwarfs at the end of their lives. Those with mass $8 M_{\odot}$ to $130 M_{\odot}$ explode as core collapse supernovae leaving neutron stars or black holes behind. Stars with mass between $130 M_{\odot}$ and $300 M_{\odot}$ disrupt completely as pair-instability supernovae leaving behind no remnant while stars more massive than $300 M_{\odot}$ collapse to black holes without explosion. If a primordial cloud of gas of $10^5 M_{\odot}$ can collapse without fragmentation, it will form a black hole before ignition of hydrogen can even occur. While these general mass ranges work for primordial stars, the moment enriched gas enters calculations of stellar evolution the story becomes much more complicated. Gas with metals has many more available channels to cool and fragment.

Stars can be characterized into broad populations according to metallicity (Baade, 1944). Population III stars (Pop III) are those which, by definition, contain primordial gas. This first generation of stars is followed by Population II (Pop II) stars which have a nonzero metallicity that exceeds a critical metallicity. This critical metallicity is defined as the heavy element abundance at which metal line cooling begins to dominate over cooling by H (and H_2 , HD) and He (Smith & Sigurdsson, 2007). Many simulations have been performed to determine the value of this critical metallicity with typical values ranging from $10^{-6} <$

$Z/Z_{\odot} < 10^{-4}$ (Santoro & Shull, 2006). Population I (Pop I) stars are metal rich and relatively young stars in the disk of our Galaxy.

Nuclides with yields independent of initial metallicity, *primary* species, are produced from the initial H and He of the star at birth. In stellar models without mass loss, initial metallicity plays a negligible role in the yields of most isotopes up to the iron peak. When mass loss is considered, chemical species that formed early on in the star can be ejected through winds. For example, C and O yields are directly influenced by mass loss from high-metallicity stars that undergo a Wolf-Rayet phase (Meynet, 2008). Large amounts of He and C are ejected with a small core left to produce O. In a similar low-metallicity star, one would see higher O and lower C yields.

Secondary species, those whose yields depend on the initial metallicity of the star, are more complicated to model. For example, s-process nuclei are produced by neutron captures on iron-peak elements, and therefore depend critically on the initial composition, stellar density, pressure, and temperature. Similarly, ^{14}N and ^{13}C depend on the efficiency of the CNO cycle and the initial abundances of the seed nuclei.

Subtle differences between various groups' treatment of these metallicity dependent yields account for much of the discrepancies between the quoted final abundances. Details pertaining to each set of yields are discussed in the following sections.

2.2 Yields of Type II Supernovae

Stars of $8 M_{\odot}$ or more are responsible for quickly polluting the ISM with metals, and are the primary source of the alpha elements. Despite their importance as Galactic polluters, large uncertainties in the explosion mechanism and pre-supernova evolution limit the ability

to calculate robust yields. These yields, for iron in particular, are sensitive to choice of the explosion energy and mass cut (the location that delineates matter which collapses inward to that which explodes). It is known that C, N, Mg, and Ne yields depend on pre-supernova models including convection, mixing, mass loss, and nuclear reaction rates, while Al, Si, S, Ar, and Ca are additionally sensitive to shock wave energies.

Early work by Arnett (1978) estimated absolute yields for stars in the mass range $8.3 \leq M/M_{\odot} \leq 115$ evolved past silicon burning, electron capture, and thermal disintegration. Chiosi & Caimmi (1979) adjusted the yields of Arnett (1978), by inclusion of stellar winds during the core H- and He-burning phases of evolution. Further work on the yields of massive stars added metallicity-dependent mass-loss rates and rotation (Maeder, 1992; Dray et al., 2003; Dray & Tout, 2003). The classic set of nucleosynthetic calculations used in models of GCE are from Woosley & Weaver (1995) (hereafter, WW95). Mass loss is not included prior to explosion. The explosion is modeled using an artificial piston that is introduced in the innermost cell of the calculation, and is designed to result in an explosion energy of 10^{51} ergs. Yields are presented for masses in the range 11 - 40 M_{\odot} and metallicities, Z/Z_{\odot} , $^1 = 0, 0.0001, 0.01, 0.1$ and 1. Several groups have improved upon these calculations by adding metallicity-dependent opacities and mass-loss rates (Maeder, 1992), adding effects due to rotation (Hirschi et al., 2005), using updated reaction rates (Limongi & Chieffi, 2003) and increasing the range of masses and metallicities (Chieffi & Limongi, 2004); (13-35 M_{\odot} , $Z/Z_{\odot} = 0, 10^{-6}, 10^{-4}, 10^{-3}, 6 \times 10^{-3}$, and 2×10^{-2}). Kobayashi et al. (2006) calculated yields for stars of metallicity $Z = 0, 0.001, 0.004, 0.02$ and masses in the range 13 - 40 M_{\odot} . Final yields are tuned to produce 0.07 M_{\odot} of ejected iron. Portinari et al. (1998) calculated

¹ Z_{\odot} is typically set at 0.02 while some groups prefer to quote absolute Z rather than Z/Z_{\odot} .

a set of yields ranging from low-mass AGB stars to massive stars undergoing explosive nucleosynthesis with a different approach to the explosion mechanism. When paired with Marigo (2001), these yields cover all stars necessary for a GCE model. In Portinari et al. (1998), supernovae are triggered by electron captures on heavy nuclei, photo-dissociation of iron into α -particles, and rapid neutralization of collapsing material. We direct the interested reader to the appendix of Portinari et al. (1998) for a full discussion of the key differences between their models and WW95. Rauscher et al. (2002) further improved upon WW95, with temperature-dependent mass loss, updated opacities, plasma neutrino losses, and convection with core overshooting. In addition, they highlight the difficulties caused by uncertain α -capture and neutron-capture rates. In particular, they discuss how the rate for $^{12}\text{C}(\alpha, \gamma)^{16}\text{O}$ could completely alter their stellar model, and dominate over other nuclear physics inputs, as well as how alteration of the neutron-capture rates leads to a drastic over-production of ^{62}N .

2.3 Yields of Hypernovae

From the observed light curves and spectra of nearby core-collapse supernovae, Kobayashi et al. (2006) find evidence for the existence of hypernovae (HNe), which eject more than ten times the typical explosion energy of 10^{51} ergs. These HNe play a major role in reproducing the observed $[\text{Zn}/\text{Fe}]$ trend, where $[\text{Zn}/\text{Fe}] \approx 0$ for $-2 \lesssim [\text{Fe}/\text{H}] \lesssim 0$. Kobayashi et al. (2006) calculated yields for HNe of various metallicities ($Z = 0, 0.001, 0.004, 0.02$) and masses in the range 13 - 40 M_{\odot} . Their models include metallicity-dependent mass loss and are tuned to produce $[\text{O}/\text{Fe}] \simeq 0.5$. This constraint is set by the abundance ratios observed in extremely metal-poor stars (Cayrel et al., 2004).

2.4 Yields of Asymptotic Giant-Branch Stars

Intermediate-mass stars are presumed to be the main producers of heavy s-process nuclides, and also contribute substantially to the yields of several other nuclides (Siess, 2007), most notably carbon and nitrogen, during their AGB phase. Dredge-up and hot-bottom burning require detailed computations of transport mechanisms, and depend strongly on stellar lifetimes, which in turn depend on the mass-loss rate. Dredge-up refers to a period in stellar evolution where the convective zone extends down to the lower layers of nuclear fusion. *First dredge-up* occurs at the beginning of the red giant-branch, and penetrates the region of the CN-cycle processed material. *Second dredge-up* occurs at the base of the AGB phase of stellar evolution, and decreases the surface abundances of ^{12}C , ^{13}C , ^{15}N , ^{16}O , and ^{17}O , while increasing ^{14}N (Siess, 2006). *Third dredge-up* (TDU) occurs after the star enters the AGB phase. In this stage, ashes from helium burning are transported from the interior to the stellar surface, whereas previous dredge-ups only brought hydrogen-burning products to the surface. *Hot-bottom burning* (HBB) refers to the evolutionary stage when the bottom of the convective envelope overlaps with the hydrogen-burning shell, such that part of the nuclear energy is transported directly to the outer layers of the star (Scalo et al., 1975). Since these periods in stellar evolution depend critically on the adopted stellar lifetimes and mass-loss rates, order of magnitude discrepancies in element production between authors are found, even at solar metallicity.

Karakas & Lattanzio (2007) and Karakas (2010) calculated detailed stellar models and post-process nucleosynthetic data to produce AGB yields. Their models cover a range in mass from $1.0 M_{\odot}$ to $6 M_{\odot}$ and compositions $Z = 0.02$, 0.008 , 0.004 , and $Z = 0.0001$. All models were evolved from the zero-age main sequence to near the tip of the thermally

pulsing AGB (TP-AGB) phase. The TDU efficiency governs nucleosynthesis in the lower-mass models, which varies as a function of the H-exhausted core mass, metallicity, and envelope mass. Karakas (2010) used an updated set of proton- and α -capture rates, and assumed scaled-solar abundances for low-metallicity models, rather than adopting the initial abundances of the Small and Large Magellanic Clouds as was done in Karakas & Lattanzio (2007). Marigo (2001) determined yields for low- and intermediate-mass stars ($0.8 M_{\odot} < M < 5-8 M_{\odot}$). Their models include a metallicity dependent core mass-luminosity relationship, with mass loss following the semi-empirical prescription described by Vassiliadis & Wood (1993), and treatment of HBB and TDU efficiency, but no extra mixing. They adopted a TDU with more efficiency at lower metallicity, and HBB with more efficiency at higher masses. van den Hoek & Groenewegen (1997) employed the stellar evolution results of the Geneva group to produce AGB yields for stars of initial mass $0.8 M_{\odot}$ to $8 M_{\odot}$ for various metallicities, $Z = 0.001, 0.004, 0.008, 0.02,$ and 0.04 , through to the TDU. Their calculations include HBB and a mass-loss scaling parameter based on Reimers (1975). We compare these three yield sets side-by-side in Figure 2.2. The clearest difference, the carbon yield, arises from the treatments of the TDU and HBB.

Yields of s-process nuclides as a function of AGB metallicity were computed by Goriely & Mowlavi (2000), based on previous models with diffusive overshooting and rotation, and the effect on partial mixing of protons and dredge-up efficiencies. They produced a set of elemental overabundance ratios, $[el/Fe]$, for $1.5-3 M_{\odot}$ stars with compositions $Z = 0.001, 0.004, 0.008,$ and 0.018 , with initially solar p- and r- process patterns. These authors warned that their assumptions of proton abundances mixed into carbon-rich layers may be oversimplified, and they cannot conclusively identify low-mass AGB stars as the main site of the s-process. Nevertheless, their model has put constraints on the partial mixing of protons,

and illustrates the significance of neutron-capture processes in AGB stars.

2.4.1 Uncertainties due to the ^{13}C Pocket

The ^{13}C pocket is essential to understanding the s-process abundance patterns observed in AGB stars. Key differences amongst stellar-yield calculations from various groups can be attributed to the model assumptions associated with this process. Neutrons released in these stars are required for the *s*-process, but can also affect the abundance of lighter elements in the He intershell (the region between the helium-burning and hydrogen-burning shells). In TP-AGB stars, two major neutron sources operate within the intershell, $^{22}\text{N}(\alpha, n)^{25}\text{Mg}$ and $^{13}\text{C}(\alpha, n)^{16}\text{O}$. During the TDU in TP-AGB stars, a sharp discontinuity between the H-rich envelope and the He- and C-rich intershell forms. This condition is maintained until H burning is reignited. At H reignition, the top layers of the He intershell heat up, and a ^{13}C pocket forms (Gallino et al., 1998).

Karakas & Lattanzio (2007) did not include a partial mixing zone of protons to produce a ^{13}C pocket. Once this was included in Karakas (2010), the result was higher ^{22}Ne and ^{23}Na , and dramatically more ^{31}P and ^{60}Fe .

2.4.2 Uncertainties due to Mass Loss

During the AGB phase of stellar evolution, the star may become unstable against large amplitude pulsations driving a strong stellar wind. This mass loss affects the strength of thermal pulsations, efficiency of the TDU, and consequently, the final yields of the star. Observations have shown no clear correlation between mass loss and any stellar parameters except

pulsation period. Consequently, it is typically parameterized with the Reimers formula,

$$\dot{M}(M_{\odot}/yr) = 1.34 \times 10^{-5} \eta \frac{L^{3/2}}{MT_{eff}^2}, \quad (2.8)$$

where η is an efficiency factor, L and M are the stellar luminosity and mass, and T_{eff} is the effective temperature of the star. This is tuned to match observed luminosity functions (Reimers, 1975). Different groups employ either a metallicity dependent or constant η in their AGB calculations.

2.4.3 Super AGB stars

Super-AGB stars (sAGB) are defined by a specific mass range between the minimum mass for carbon ignition and the mass limit above which the star ignites neon at its center, and evolves through all nuclear burning stages up to an iron-core collapse supernovae (Siess, 2007). When taking into account the stellar-mass distribution, it is clear that these stars represent a significant fraction of all stars in a population. Romano et al. (2010) estimated that more than 30% of all newly-produced He and N may come from stars with masses in this range.

The fraction of sAGB stars that evolve into WD or neutron stars depends critically on the interaction between mass loss and core growth. Evolution is sensitive to core overshooting (extended convective mixing), first and second dredge-up, and mass-loss rate. As Siess (2010) points out, sAGB stars in the range of 7-11 M_{\odot} are as numerous as stars above 11 M_{\odot} , and are therefore quite significant for GCE models. However, typical calculations require \sim 1200-2500 numerical shells and more than 3×10^7 time steps. This enormous computational expense is the main reason few yields for sAGB stars exist in the literature. In addition, the

uncertainties regarding the TDU have a strong impact on the fraction of chemical species that can reach the envelope.

It is worth discussing the input physics for the latest Siess (2010) model, in order to better understand the paucity of sAGB yields in the literature. Yields are computed in a post-processing step, with initial mass ranges focused on covering the computationally demanding thermal pulses. The envelope structure between pulses is described by T_{env} , luminosity, T_{eff} , and radius. The model computes the evolution of convective-zone abundances, with instantaneous mixing of chemical species, and allows for different nuclear reaction rates and uncertainties within the TDU and convection. It implements a linearly decreasing mass-loss rate and T_{env} and variable mixing lengths. A larger mixing-length parameter leads to a higher luminosity and mass-loss rate, thereby shortening the thermally pulsing phase.

2.5 Yields of Type Ia Supernovae

Thermonuclear supernovae are important contributors to the chemical enrichment of the ISM, primarily with iron-peak nuclei and some intermediate-mass nuclei (from silicon to calcium). SNIa are usually modeled as explosions of white dwarfs that have approached the Chandrasekhar limit ($M_{ch} \sim 1.39M_{\odot}$) through accretion from a companion in a binary system, although a different mechanism, the merging of two carbon-oxygen (C-O) white dwarfs, is also possible. Since details depend on the accretion rates from a companion of various masses, among other parameters, SNIa yields are difficult to calculate. The deflagration model W7 (Nomoto et al., 1997) is used most widely, and it successfully reproduces observed spectra. Most models are spherically symmetric; however, turbulence is expected to play an important role at all stages of a thermonuclear supernova (Schmidt et al., 2010).

The 3D calculations that have become more prominent (Travaglio et al., 2004) are necessary if stellar yields are to be determined from first principles. Iwamoto et al. (1999) compares several SNIa models against W7, including delayed detonations and carbon deflagration; we direct the interested reader to this paper for details.

2.5.1 Progenitors and Model Assumptions

Progenitor models are classified as single degenerate (SD), in which a white dwarf grows in mass due to accretion from an evolving binary companion, and double degenerate (DD), in which two C-O white dwarfs merge. The single-degenerate channel for SNe Ia can be made to match the observed SN Ia rate-SFR relation, but only if white dwarfs are converted to SNe Ia with a uniform efficiency of $\sim 1\%$ (Pritchett et al., 2008).

Type Ia supernovae explosions are believed to occur as soon as the compact object reaches the Chandrasekhar mass. Consequently, yields from these explosions will be independent of the initial stellar mass of either the compact object or its binary companion. Models typically assume that the final fractions of carbon, nitrogen, and oxygen do not vary significantly between white dwarfs of different initial masses.

2.6 Neutron-Capture Element Yields

The observed heavy elements (above the iron-peak) distribution in the Solar System exhibits the presence of two main components, associated with at least two different nucleosynthetic processes: known as the s- (slow) process and the r- (rapid) process. When the neutron flux is so large that the decay of an unstable nucleus created after neutron capture is small compared to the β -decay rate, the nucleosynthesis path will undergo successive β decays until

the most neutron-rich, stable element is reached (Burbidge et al., 1957). These r-process elements, which are close to the neutron drip line, require a large neutron flux in a small amount of time. While the r-process occurs in explosive environments, the s-process can take place inside stars. The s-process is characterized by a neutron-capture rate that is slow with respect to the corresponding β decay, and produces elements close to the group of stable nuclei.

Low-mass ($1.5 \leq M/M_{\odot} \leq 3$) AGB stars account for nearly all production of s-process nuclei from Zr to Pb due to the neutron-rich ^{13}C pocket (Travaglio et al., 2004). During the TP-AGB phase, a recurrent dredge-up of the convective envelope in the H-exhausted core brings protons in a region where the chemical composition is dominated by C and He. As the temperature rises, a ^{13}C pocket forms. The dominant reaction in this pocket, $^{13}\text{C}(\alpha, n)^{16}\text{O}$, releases neutrons between thermal pulses, while the $^{22}\text{Ne}(\alpha, n)^{25}\text{Mg}$ reaction is active during pulses (Gallino et al., 1998). These reactions give rise to the main component of s-process nucleosynthesis. The s-process depends strongly on the efficiency of the main neutron source, ^{13}C . An additional component, the weak s-process, is thought to be responsible for nuclides up to $A \sim 90$. While the main s-process produces heavy elements beyond Sr, up to Pb, in low-mass TP-AGB stars, the weak s-process comes from core He and shell C burning in massive stars (Travaglio et al., 2004). In this work, we adopt the metallicity-dependent yields of Travaglio et al. (2004) for the s-process element Ba and Sr produced in AGB stars.

The site of the astrophysical r-process is still unknown. In this work, the constant r-process yields suggested by Wanajo & Ishimaru (2006) are used to follow the enrichment history of europium. Wanajo & Ishimaru (2006) discuss possible scenarios, including neutrino winds and the prompt explosion of low-mass supernovae. Specifically, they show how a neutrino wind can increase entropy sufficiently to overcome the r-process bottleneck reaction,

at $Z \sim 6$. This produces three clear peaks in the abundance pattern of r-process elements at $A=80$, 130 , and 195 . The prompt explosion scenario involves a massive star that explodes prior to neutrino heating, resulting in neutron-rich ejecta. Models of this phenomenon can produce the observed r-process pattern; however, making the necessary stellar explosion happen consistently has been a major challenge (Sumiyoshi et al., 2001).

Chapter 3

Galactic Chemical Evolution

Implementation

Our ultimate goal is to model GCE within cosmological hydrodynamical simulations of galaxy formation. This drives our fundamental requirements – namely, the ability to model the nucleosynthetic and energetic feedback from stellar populations of highly variable metallicity, and possibly variable IMF, over a period of up to 14 billion years. In cosmological simulations, star formation is approximated in a relatively simple way. Gas in a grid cell or smoothed particle hydrodynamics (SPH) particle reaches a certain set of conditions (density threshold, cooling time, metal fraction, Jeans’ mass, or some subset thereof), and some of that gas in that cell or particle is removed and turned into a *star particle*. This star particle is assumed to have a constant metallicity, inherited from the gas from which it forms. Since simulations inherently have limited resolution, the star particles are typically much more massive than a single star, and are thus assumed to represent an ensemble of stars. We refer to such a particle as a *simple stellar population* (SSP) with a known IMF, constant metallicity, and single formation time. Given these assumptions, a star particle is the perfect platform for implementing a chemical evolution model, and exploring the effects of IMF, nucleosynthetic yields, stellar lifetimes, and feedback rates.

3.1 Element Coverage

Tracking all elemental and isotopic species in a cosmological simulation is presently not feasible, due to the practical limitations of finite computing resources and the availability of stellar nucleosynthetic yields. Since only a fraction of elements significantly contribute to cooling and heating, one can implement simple cooling models, based on tabulated cooling curves, or solutions to smaller reaction networks [involving only a few species. Radiative-cooling models used in cosmological simulations vary in complexity, and could follow several species of H, He, and D, but typically only require an overall metallicity to characterize all higher-mass elements. Our goal is to reduce the set of all elements and isotopes down to a finite number that are representative of the important ISM and nucleosynthetic processes that we wish to capture in our calculations. For this reason, we have elected to follow the chemical history of 12 elements, due to their observational accessibility and representation of the major nucleosynthetic groups. We have selected a *minimum* set of elements responsible for the cooling of the ISM and IGM, elements that are tracers of AGB, Type II, and Type Ia supernovae, elements which contribute a substantial mass fraction to the ISM, and which are important to later stellar-evolution episodes.

3.1.1 Primary ISM Coolants

Carbon, nitrogen, and oxygen are primary coolants, and abundant in the majority of stars. Carbon is known to form through the triple-alpha process; however, it is still uncertain whether massive stars or intermediate-mass stars are the main carbon-production sites. Nitrogen is synthesized mainly in intermediate-mass stars through the CNO cycle in the hydrogen-burning layers. Oxygen forms in the interior of massive stars.

3.1.2 The Alpha Elements

Magnesium, calcium, and titanium are chosen to represent the α -element group. The α -element nuclei are integer multiples of helium nuclei, built up by successive α -captures, from O to Ti. Since no single nuclear reaction is responsible for the synthesis of the α -elements, their abundances are not rigidly coupled. Plots of $[\alpha/\text{Fe}]$ versus $[\text{Fe}/\text{H}]$ in the solar neighborhood show a plateau below $[\text{Fe}/\text{H}] \sim -1$, followed by a steady decline to $[\alpha/\text{Fe}] \sim 0$ at $[\text{Fe}/\text{H}] \sim 0$. Tinsley (1979) proposed the relation between $[\text{O}/\text{Fe}]$ and $[\text{Fe}/\text{H}]$ resulted from the time delay between SNII and SNIa. At early times $[\text{Fe}/\text{H}]$ is inherently low and SNII production of O dominated. At later times, SNIa eject Fe but no O. While SNIa yields show little O and Mg, they do show production of Ca such that the trend of $[\text{Ca}/\text{Fe}]$ versus $[\text{Fe}/\text{H}]$ should show a smaller amplitude trend than $[\text{O}/\text{Fe}]$ and $[\text{Fe}/\text{H}]$.

Magnesium is primarily produced during carbon burning and explosive neon burning stages in massive stars (Woosley & Weaver, 1995); calcium production is a result of incomplete silicon- and oxygen-burning episodes in massive stars (Woosley & Weaver, 1995). Titanium is a product of complete and incomplete silicon burning (Woosley & Weaver, 1995). These elements trace both the hydrostatic (Mg) and explosive stages (Ca, Ti) of stellar nucleosynthesis.

3.1.3 The Iron-Peak Elements

Iron, cobalt, and zinc are observable elements that trace the explosive nucleosynthesis of massive stars. Cobalt is produced from complete silicon burning at high pressure and temperature. Zinc can be found in high-redshift damped Lyman- α systems, and traces iron over three orders of magnitude in $[\text{Fe}/\text{H}]$ (Nissen et al., 2004). Iron and cobalt abundance

patterns in stars provide tracers of SNIa delay times, while zinc and cobalt over-abundances at low stellar metallicities trace highly energetic supernovae (Umeda & Nomoto, 2002).

3.1.4 The Neutron-Capture Elements

Europium, an almost exclusively r-process element in the Solar System, barium, a mostly s-process only element, and strontium, a combined r- and s-process element, are readily observed with high-resolution spectroscopy of most metal-poor stars, excluding perhaps only the very lowest metallicity examples. While they are not typically represented in yield calculations, simple models may be able to distinguish between neutron-capture sites and production mechanisms.

3.2 Initial Mass Function

The Initial Mass Function, IMF, is the most important input to chemical evolution models as it sets the possible elemental yield limits. This initial distribution tells us how many low mass stars can survive until the present epoch as well as the overall mass budget for chemical feedback. The number of stars created within a given mass range is calculated through integration of the stellar IMF. Common parameterizations of this function are a log-normal distribution with a characteristic mass, a simple power-law form, and combinations of broken power-law and log-normal distributions. Each distribution is normalized such that

$$\int_{M_{low}}^{M_{high}} M \frac{dN}{dm} = 1M_{\odot}, \quad (3.1)$$

where dN/dm represents the number of stars within a given mass range. The stellar IMF cannot, at present, be calculated from first principles, and must be derived from observations. Current IMFs are typically obtained from counts of real stars, and hence are subject to numerous uncertainties. Since it is not known which one most accurately represents the actual mass distribution of stars in the local universe, seen and unseen, it is worthwhile to investigate a variety of IMFs, and note the effect their variation has on the resulting nucleosynthetic production. We consider the IMFs of Salpeter (1955); Scalo (1998, 1986); Tinsley (1980); Kroupa (2002); Chabrier (2003), and Tumlinson (2006). The IMFs implemented in this model are as follows:

$$\frac{dN}{dm} = \Phi_{Tinsley} = \begin{cases} Am^{-2.0} & m < 2M_{\odot} \\ Bm^{-2.3} & 2 < m/M_{\odot} < 10 \\ Cm^{-3.3} & m > 10M_{\odot} \end{cases} \quad (3.2)$$

$$\Phi_{Kroupa} = \begin{cases} Am^{-1.3} & m < 0.5M_{\odot} \\ Bm^{-2.2} & 0.5 < m/M_{\odot} < 1 \\ Cm^{-2.7} & m > 1M_{\odot} \end{cases} \quad (3.3)$$

$$\Phi_{Scalo98} = \begin{cases} Am^{-1.2} & m < 1M_{\odot} \\ Bm^{-2.7} & 1 < m/M_{\odot} < 10 \\ Cm^{-2.3} & m > 10M_{\odot} \end{cases} \quad (3.4)$$

$$\Phi_{Scalo86} = \begin{cases} Am^{-2.35} & m < 2M_{\odot} \\ Bm^{-2.7} & m > 2M_{\odot} \end{cases} \quad (3.5)$$

$$\Phi_{Chabrier} = \begin{cases} Ae^{-(\log m/m_c)^2/2\sigma^2} & m \leq 1M_{\odot} \\ Bm^{-1.3} & m > 1M_{\odot} \end{cases} \quad (3.6)$$

$$\Phi_{Salpeter} = Am^{-2.35} \quad (3.7)$$

$$\Phi_{Lognormal} = Ae^{-(\log m/m_c)^2/2\sigma^2} \quad (3.8)$$

The normalization constants (A,B,C) are Tinsley = (0.201, 0.248, 2.48), Kroupa = (0.56, 0.3, 0.3), Scalo98 = (0.378, 0.378, 0.151), Scalo86 = (0.174, 0.221, -), Salpeter = (0.154, -, -), Chabrier = (0.799, 0.223, -), log-normal = (0.678, -, -). For the Chabrier IMF, the characteristic mass, m_c , is $0.079 M_{\odot}$ and the dispersion, σ , is $0.69 M_{\odot}$. For the log-normal IMF, the characteristic mass is $8 M_{\odot}$ and the dispersion is $1 M_{\odot}$.

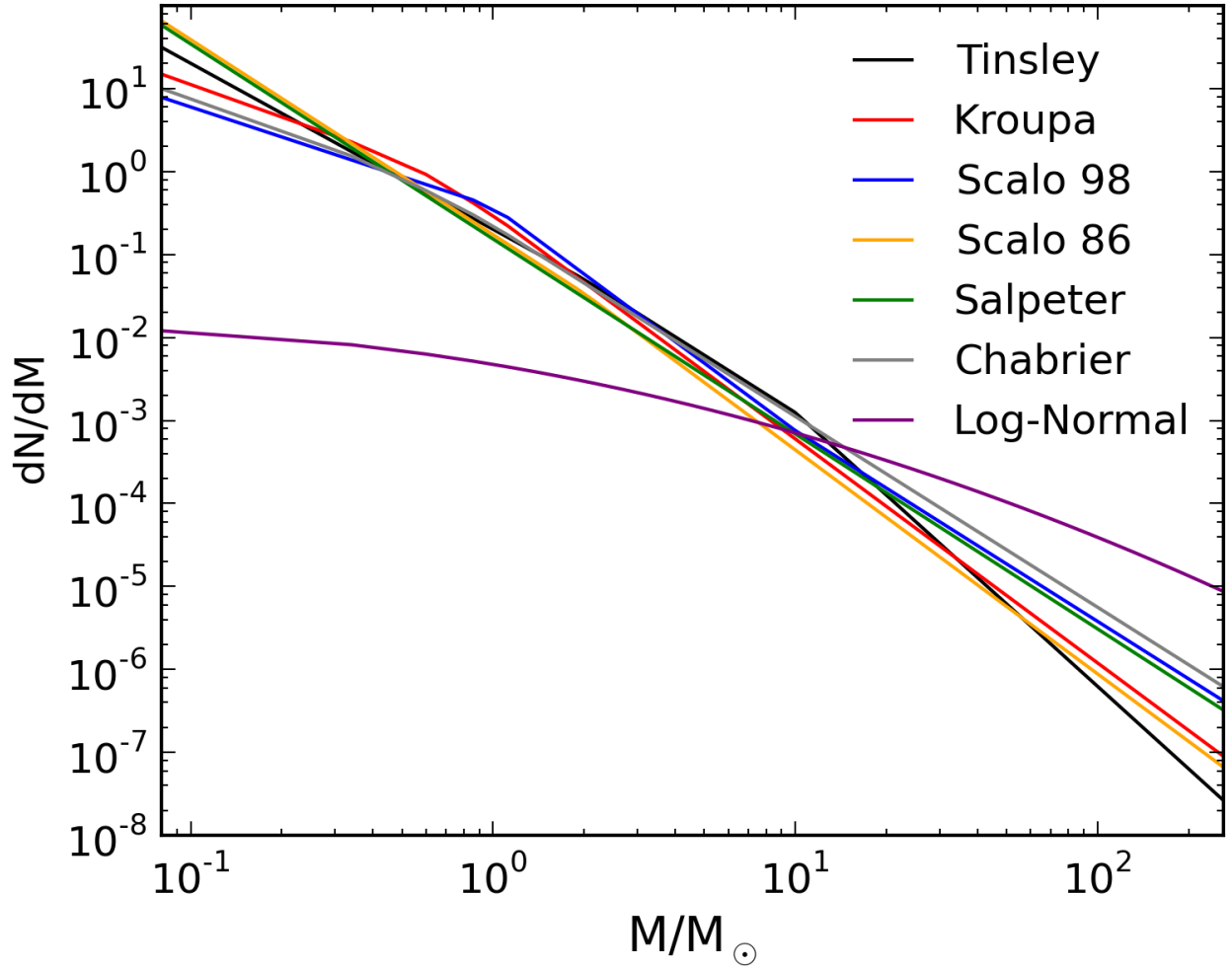


Figure 3.1: Seven IMFs with $m_{low} = 0.08 M_{\odot}$ and $m_{high} = 260 M_{\odot}$. All, with the exception of the log-normal function, are empirical fits to the observed stellar population in the local universe. See Section 3.2 for the functional forms.

3.3 Stellar Lifetimes

Following the stellar mass – lifetime scale relation of Raiteri et al. (1996), stellar lifetimes are calculated for all stars as follows:

$$\log_{10} \tau_* = a_0(Z) + a_1(Z) \log_{10} M + a_2(Z) (\log_{10} M)^2 \quad (3.9)$$

$$a_0(Z) = 10.13 + 0.07547 \log_{10} Z - 0.008084 (\log_{10} Z)^2 \quad (3.10)$$

$$a_1(Z) = -4.424 - 0.7939 \log_{10} Z - 0.1187 (\log_{10} Z)^2 \quad (3.11)$$

$$a_2(Z) = 1.262 + 0.3385 \log_{10} Z + 0.05417 (\log_{10} Z)^2. \quad (3.12)$$

The stellar lifetime, τ_* , has units of years, while M has units of M_\odot , and is valid in the metallicity range $7 \times 10^{-5} \leq Z \leq 3 \times 10^{-2}$. Lower and higher metallicities are changed to the interval extrema (i.e., stars are assumed to have the same lifetime as $Z=0.004$ stars if Z is lower than 0.004).

3.4 Stellar Ejecta

Feedback occurs in three key forms; mechanical, chemical, and radiative. Mechanical feedback is associated with the ejection of energy from AGB winds or supernovae explosions and tends to quench star formation by raising the temperature of proto-stellar gas. Chemical feedback of newly formed metals allows for the transition from primordial star formation where cooling is dominated by H_2 and HD cooling to modern star formation where cooling is dominated by metal line cooling. Feedback of ionizing radiation also tends to inhibit star formation by heating protostellar gas. This model includes both mechanical and chemical feedback in the form of injected kinetic energy and returned metals. We assume all of the

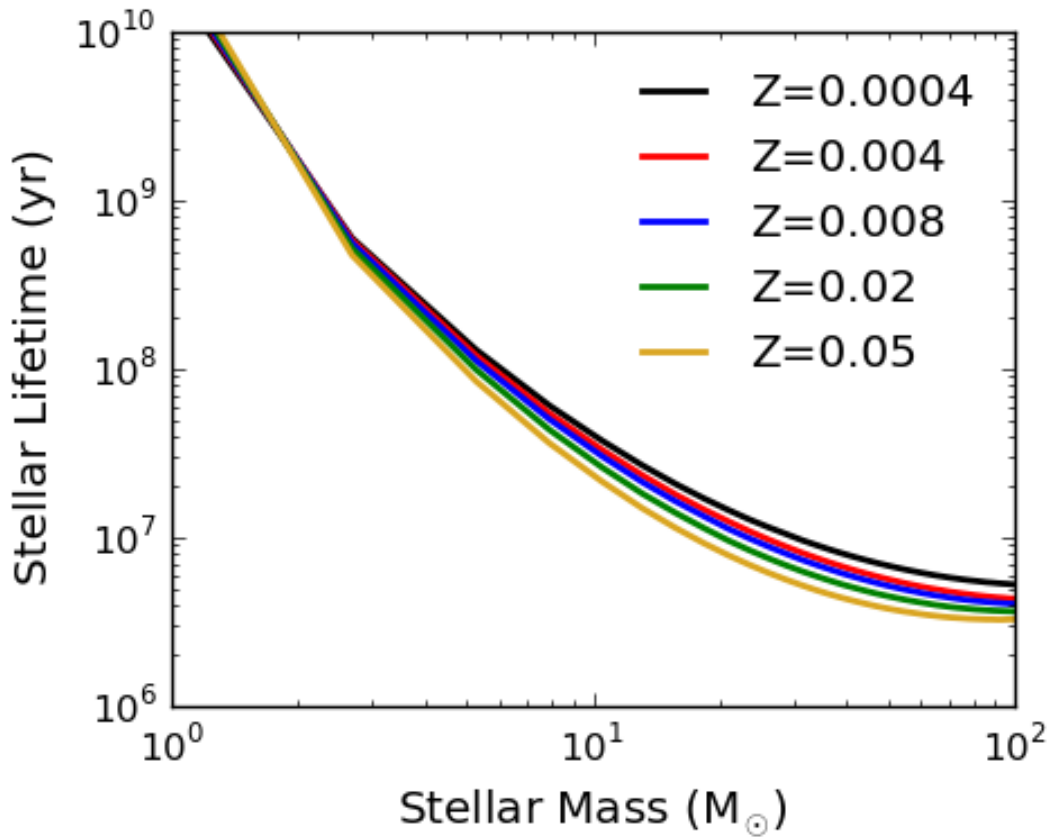


Figure 3.2: Stellar lifetime (duration of H- and He-burning phases) for stellar evolution models with masses between 0.6 and $120 M_{\odot}$ and metallicities $Z = 0.0004$ to 0.05 fit by Raiteri et al. (1996). The lifetime of stars is a strong function of initial stellar mass, and only weakly dependent on stellar metallicity.

mass is ejected in the final time step of a star’s lifetime.

The mass of species, j , that is ejected during a time interval $(t, t + \Delta t)$ by an SSP with total initial mass, $m_{*,0}$, and metallicity, Z , that was created at time $t_* < t$, is given by

$$\Delta m_{*,j} = m_{*,j}(t) - m_{*,j}(t + \Delta t) \quad (3.13)$$

$$= m_{*,0} \int_{M_Z(t-t_*+\Delta t)}^{M_Z(t-t_*)} \frac{dN}{dM} m_{ej,j}(M, Z) dM, \quad (3.14)$$

where $M_Z(\tau)$ is the inverse of the lifetime function $\tau_Z(M)$, and $m_{ej,j}(M, Z)$ is the mass ejected of species j by a single star. The functions $\tau_Z(M)$ and $m_{ej,j}(M, Z)$ need to be taken from stellar evolution and nucleosynthesis calculations provided in the literature.

The ejected mass of element j can be written as the sum of three components. The first is the mass that would have been ejected without nucleosynthetic processing. The second tracks the newly produced elements, and the third represents the newly destroyed elements,

$$m_{j,ej}(M) = [\chi_j Y_{tot}(M)]_{sim} + Y_j(M) - [\chi_j Y_{tot}(M)]_{table}, \quad (3.15)$$

where $\chi_j Y_{tot}$ is the initial fraction of mass of element j as tracked by the simulation, and Y_j is the yield of element j from a star of mass M , according to published tables. Negative values for $m_{j,ej}$, summed over all stellar populations, are set to zero to avoid unphysical negative total abundances.

3.5 Type Ia Supernovae Rates

Type Ia supernovae contribute substantially to the nucleosynthetic history of galaxies. They contribute approximately 50% of all iron, and substantial amounts of other elements (Hillebrandt & Niemeyer, 2000). As opposed to Type II supernovae, whose rates closely track the star formation rates in galaxies over a wide range of redshifts, the observed rates of SNIa are much more difficult to understand, since they substantially lag star formation (Kobayashi & Nomoto, 2009). The Supernova Legacy Survey (SNLS) studied ~ 500 spectroscopically confirmed Type Ia Supernovae, and provided measurements of rates and placed constraints on the physical nature of their progenitor systems over five years. Results from the first three years of this survey place the SNIa rate at approximately 1% of the white dwarf formation rate, with a time delay distribution proportional to $t^{-0.5 \pm 0.2}$ for a wide range of populations (Pritchett et al., 2008). Neill et al. (2007) show a SNIa rate of,

$$\frac{R_{Ia}(z = 0.5)}{10^{-4} \text{yr}^{-1} \left(h_{70}^{-1} \text{Mpc}\right)^3} = 0.42 \pm 0.6_{-0.09}^{+0.13}. \quad (3.16)$$

Sullivan et al. (2006) found rates with respect to the host galaxy star formation rate and total mass as the sum of:

$$R(SNIa) = 5.3 \pm 1.1 \times 10^{-14} \text{yr}^{-1} M_{\odot}^{-1} \quad (3.17)$$

$$R(SNIa) = 3.9 \pm 0.7 \times 10^{-4} \text{yr}^{-1} \text{SFR}^{-1}. \quad (3.18)$$

One can attempt to model scenarios that would lead to these observed rates, based on various formation mechanisms. Assuming Type Ia supernova progenitors are C-O white

dwarfs that accrete mass from binary companions, the number of SNIa events within an SSP during a given time interval is calculated based on the binary fraction, IMF, lifetime of the secondary star, and the total mass of the binary system, as followed by Matteucci & Recchi (2001). This number is

$$N_{SNIa} = \int_{m_i}^{m_{i-1}} \tilde{\Phi}(M_2) dM_2, \quad (3.19)$$

where m_i and m_{i-1} are the masses of the stars that end their lifetimes at the end and beginning of the time step, respectively, M_2 is the mass of the secondary, and $\tilde{\Phi}$ represents the IMF of the secondary, including the distribution function its mass relative to the total mass of the binary system. The secondary object's IMF is described as

$$\tilde{\Phi}(M_2) = M_s A \int_{M_{inf}}^{M_{sup}} \left(\frac{M_2}{M_b} \right)^2 M_b^{-2.7} dM_b \quad (3.20)$$

$$M_{inf} = \max(2M_2, 3M_\odot) \quad (3.21)$$

$$M_{sup} = M_2 + 8M_\odot, \quad (3.22)$$

where M_s is the star particle mass, M_b is the total binary mass, and A is tuned to set the binary fraction. The minimum mass of the binary system is assumed to be $3 M_\odot$ to ensure that the WD and its companion are sufficiently massive to allow the C-O WD with the minimum possible mass, $0.5 M_\odot$, to reach the Chandrasekhar mass after accretion. The smallest possible secondary mass is $0.8 M_\odot$. The range from largest to smallest binary mass gives a timescale ranging from 3×10^7 yr to the current age of the universe:

$$\mathcal{R}_{\text{Ia}} = b \int_{\max[m_{\text{p},\ell}, m_t]}^{m_{\text{p},u}} \frac{1}{m} \phi(m) dm \times \int_{\max[m_{\text{d},\ell}, m_t]}^{m_{\text{d},u}} \frac{1}{m} \psi(t - \tau_m) \phi_{\text{d}}(m) dm. \quad (3.23)$$

With a goal of matching the observed rates and reproducing the $[(\alpha, \text{Mn}, \text{Zn}) / \text{Fe}]$ - $[\text{Fe}/\text{H}]$ relations in the solar neighborhood, Kobayashi & Nomoto (2009) produced a metallicity-dependent SNIa rate model based on the same formalism as Matteucci & Recchi (2001). Metallicity dependencies arise from the WD wind and mass-stripping effect on the binary companion star. These rates, plotted as a function of mass and SNIa lifetime, are shown in Figure 3.3, with the $0.1 Z_{\odot}$ rates plotted in each panel for reference.

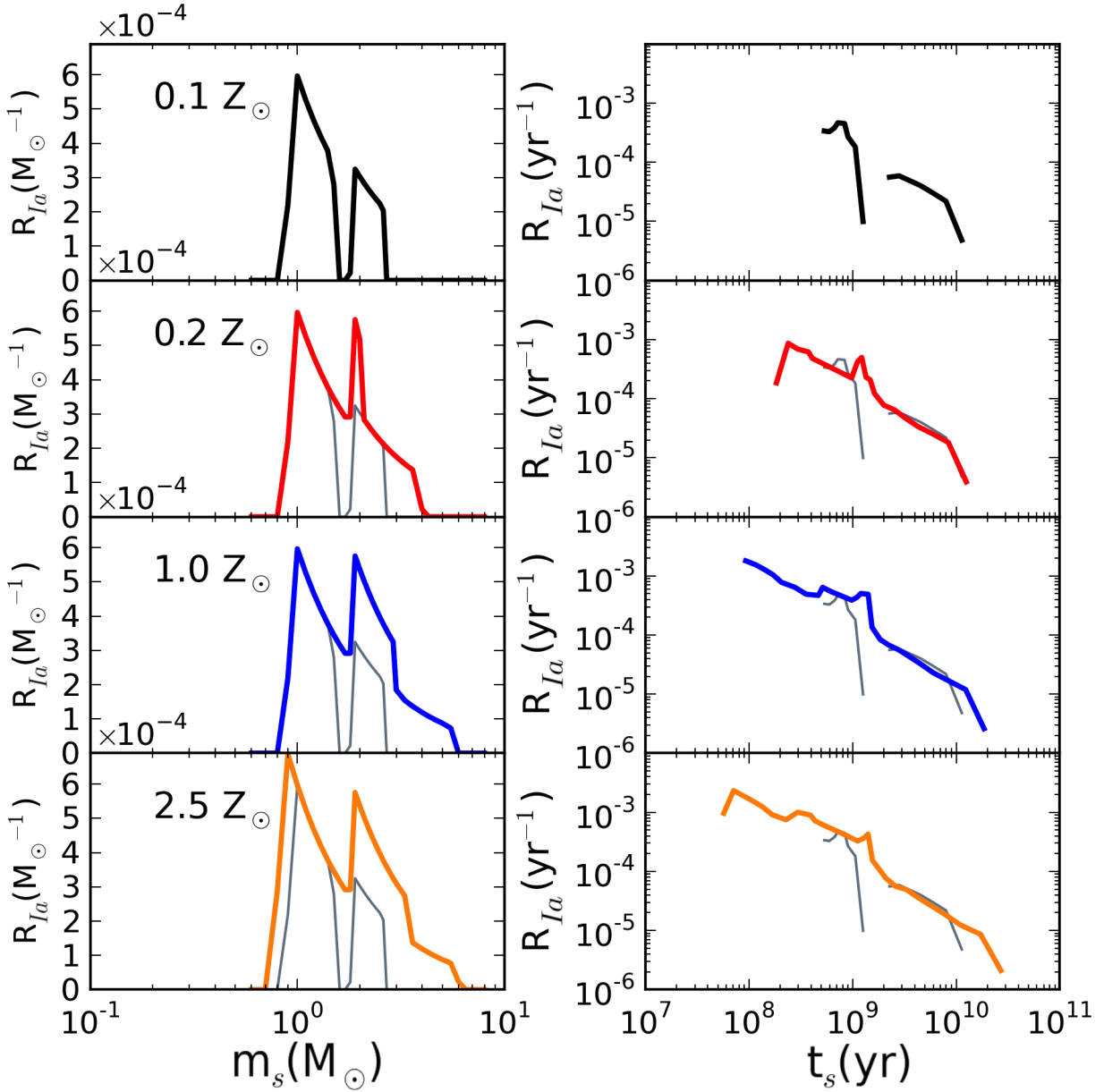


Figure 3.3: The lifetimes of SNIa are determined by the mass of the main sequence or giant companion to the C-O white dwarf. Here, Type Ia supernovae rates are shown as a function of the mass of the secondary star and its lifetime, plotted for various metallicities. The $Z=0.1 Z_{\odot}$ models is shown as a gray line in each panel for reference.

Chapter 4

Analysis of a Simple Stellar Population

The fundamental unit of stellar modeling within a cosmological simulation of galaxy formation is the star particle, which is meant to model a simple stellar population (SSP); a sample of stars of a single metallicity, IMF, and creation time. These star particles are created at a variety of metallicities and redshifts, and enrich the ISM with metals, creating the environment for future generations of star particles. Given the fundamental nature of the SSPs modeled with star particles, it is worthwhile to understand the limits of what properties of stellar populations can be constrained when using the outputs of modern astronomical observations and stellar-evolution calculations. In this section, we examine the effects that uncertainties in the observed IMF and simulated stellar nucleosynthetic yields have on our ability to model the outputs of SSP.

4.1 Simple Stellar Population Example

We have decided to model SSP composed of gas at solar metallicity. The actual total mass is immaterial, because the numbers are all scaled as a fraction of the total SSP mass. We chose to either vary the IMF *or* the yields. In all cases, the minimum and maximum stellar masses

in the IMF are $0.08 M_{\odot}$ and $260 M_{\odot}$; the overall normalization of each IMF is calculated under this assumption.

We determine stellar yields as a function of stellar age using the lifetime-initial mass relation (see Section 3.3). Figure 4.1 shows the carbon yields of Karakas (2010), Siess (2007), Kobayashi et al. (2006), and Iwamoto et al. (1999), each representing a different portion of the IMF, converted to total ejected mass, plotted as a function of stellar age for several choices of IMF. From these, we notice several important features. First, there is a jagged discontinuity at approximately 10^7 years, which highlights the transition between AGB yields and SNII yields and the complicated sAGB stellar mass range. Next, there is a dotted line to represent yields of SNIa. Since ejecta are released according to the time delay functions derived in Section 3.5, rather than according to stellar age, the SNIa yields are recorded separately on this plot. The total amount of ejected carbon is therefore the sum of this dotted line with each of the solid lines.

The enrichment history for this SSP is shown in Figure 4.2, where the ejecta are integrated throughout the lifetime of the population. This same exercise has been repeated for each of the 12 selected elements for various metallicities (see Figure 4.3). Additionally, figure 4.4 shows the evolution of $[\text{Fe}/\text{H}]$ as a function of stellar population age. Each supernovae event adds 10^{51} erg of energy to the ISM. While the mass and metallicity feedback from AGB stars is substantial, energy feedback is negligible, since the winds from these stars are typically under 100 km s^{-1} . The energy released by an SSP is shown in Figure 4.5, as a function of the age of the stellar population. The change in energy released from one time step to the next is shown in figure 4.6, plotted separately for AGB stars, and SNII for each set of available yields weighted by 5 IMFs.

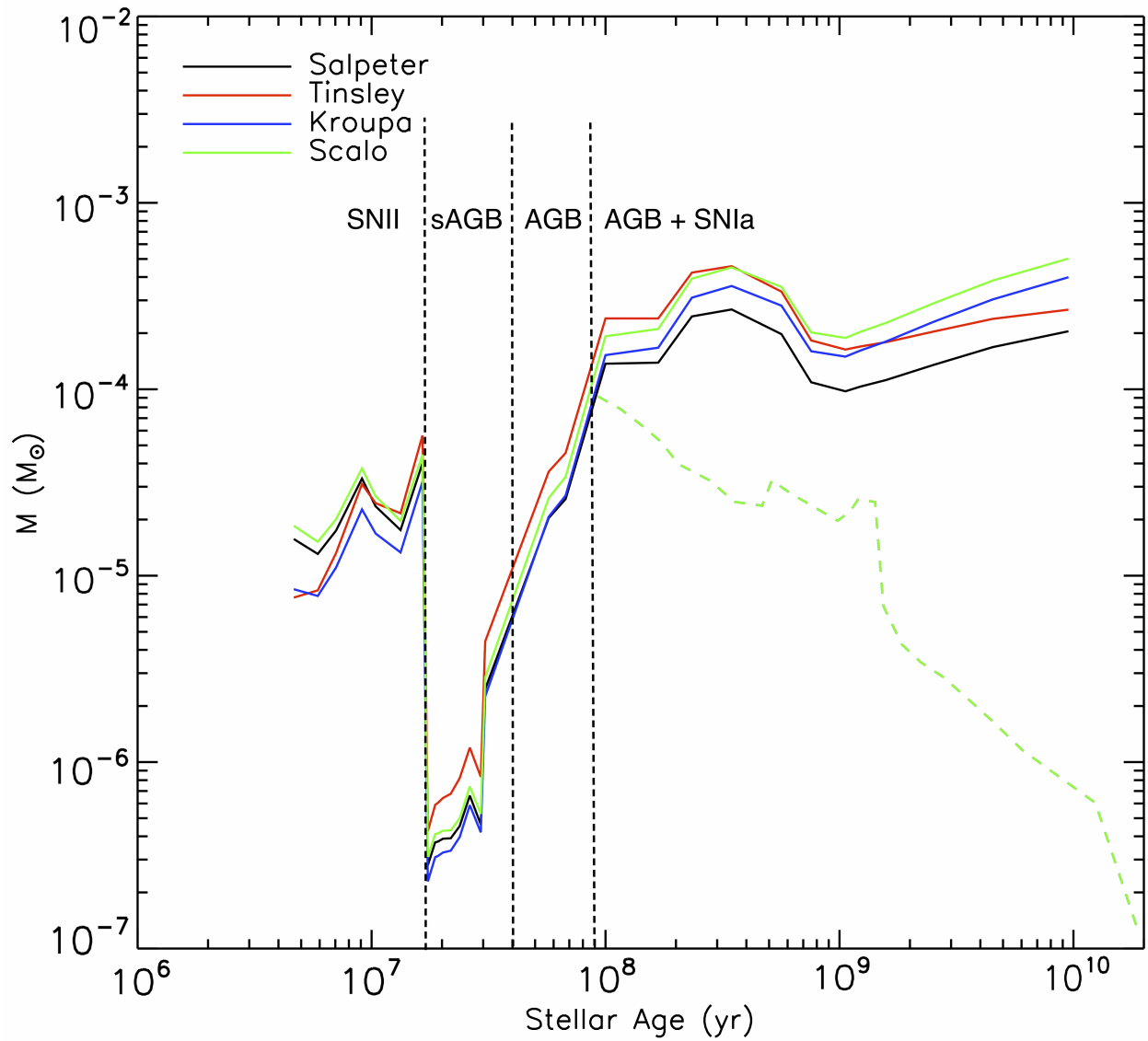


Figure 4.1: Stellar yield of carbon, as a function of time since stellar formation, for various IMFs. The dotted line shows the yield from SNIa, which should be summed with yields from AGB stars and SNIi. Vertical lines are drawn at 12, 8, and 6 M_{\odot} .

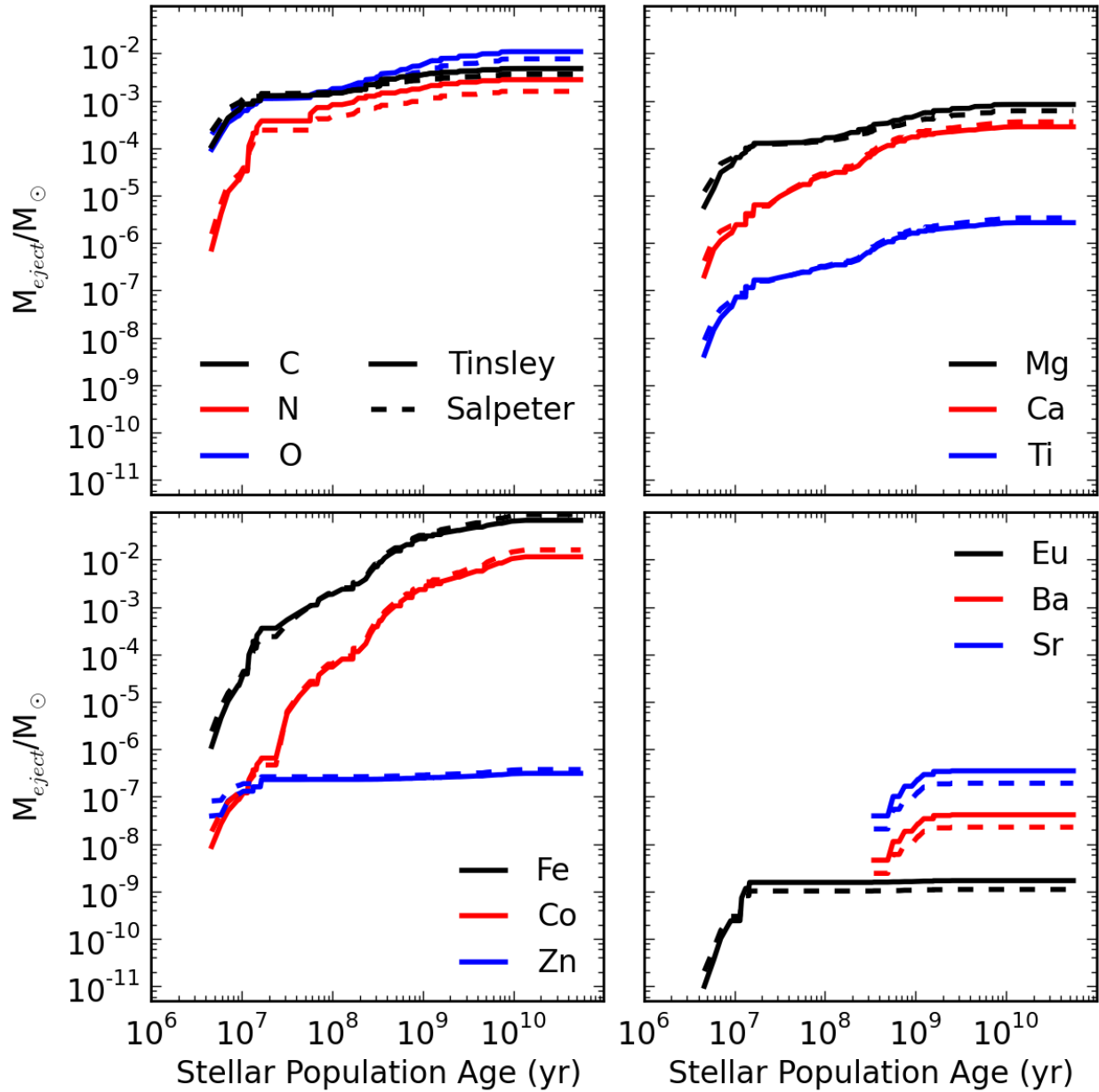


Figure 4.2: Time-integrated total mass returned to the ISM by a simple stellar population, $Z = 0.02 = Z_{\odot}$, as a function of its age. The feedback model includes mass returned from AGB stars, SNe Ia, SNeII, and the winds from their progenitors assuming two initial mass functions. Stellar yields are obtained from Karakas (2010), Siess (2007), Kobayashi et al. (2006), and Iwamoto et al. (1999).

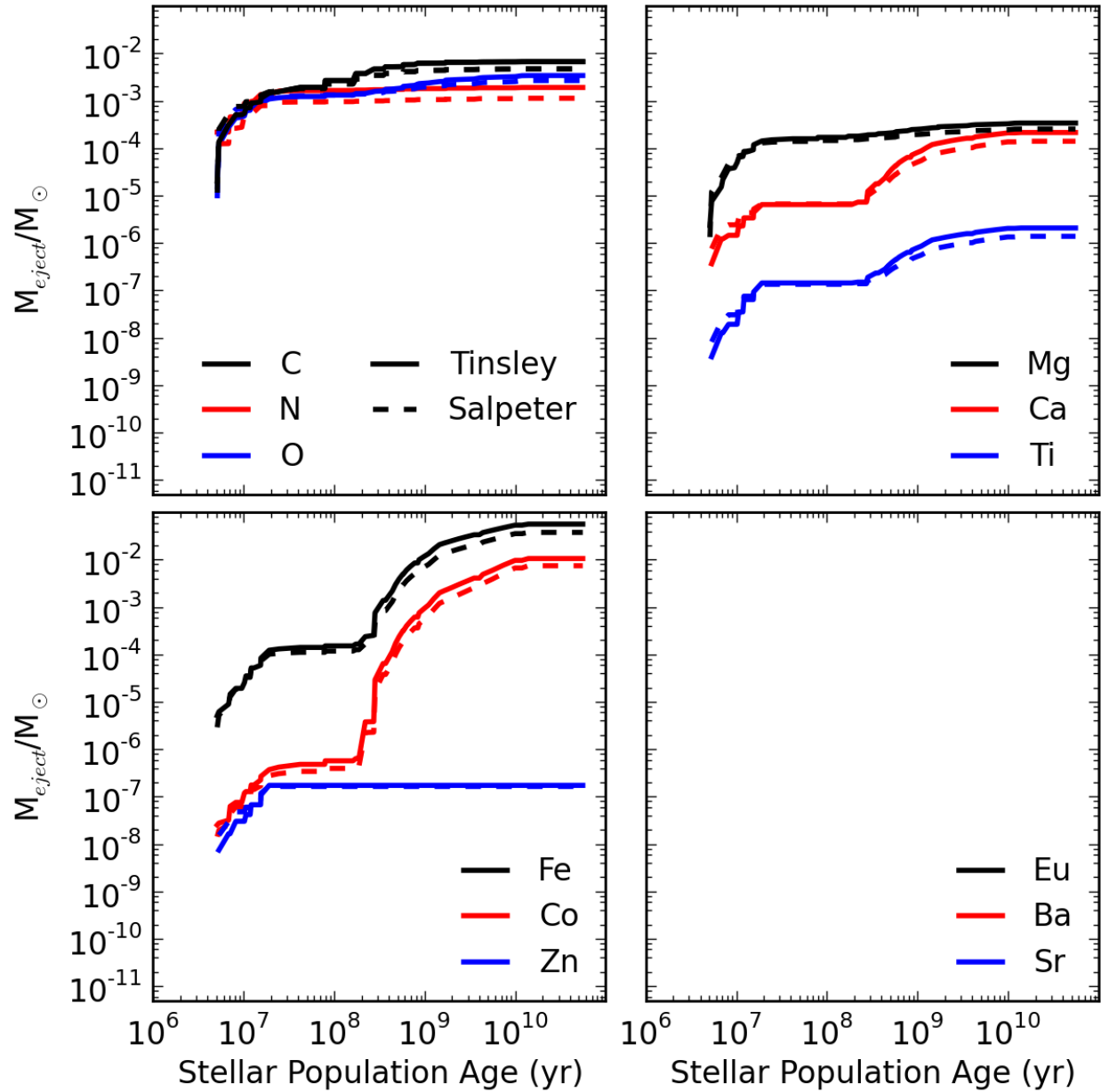


Figure 4.3: Time-integrated total mass returned to the ISM by a simple stellar population, $Z = 0.004 = 0.2 Z_{\odot}$, as a function of its age. The feedback model includes mass returned from AGB stars, SNe Ia, SNeII, and the winds from their progenitors assuming two initial mass functions. Stellar yields are obtained from Karakas (2010), Siess (2007), Kobayashi et al. (2006), and Iwamoto et al. (1999).

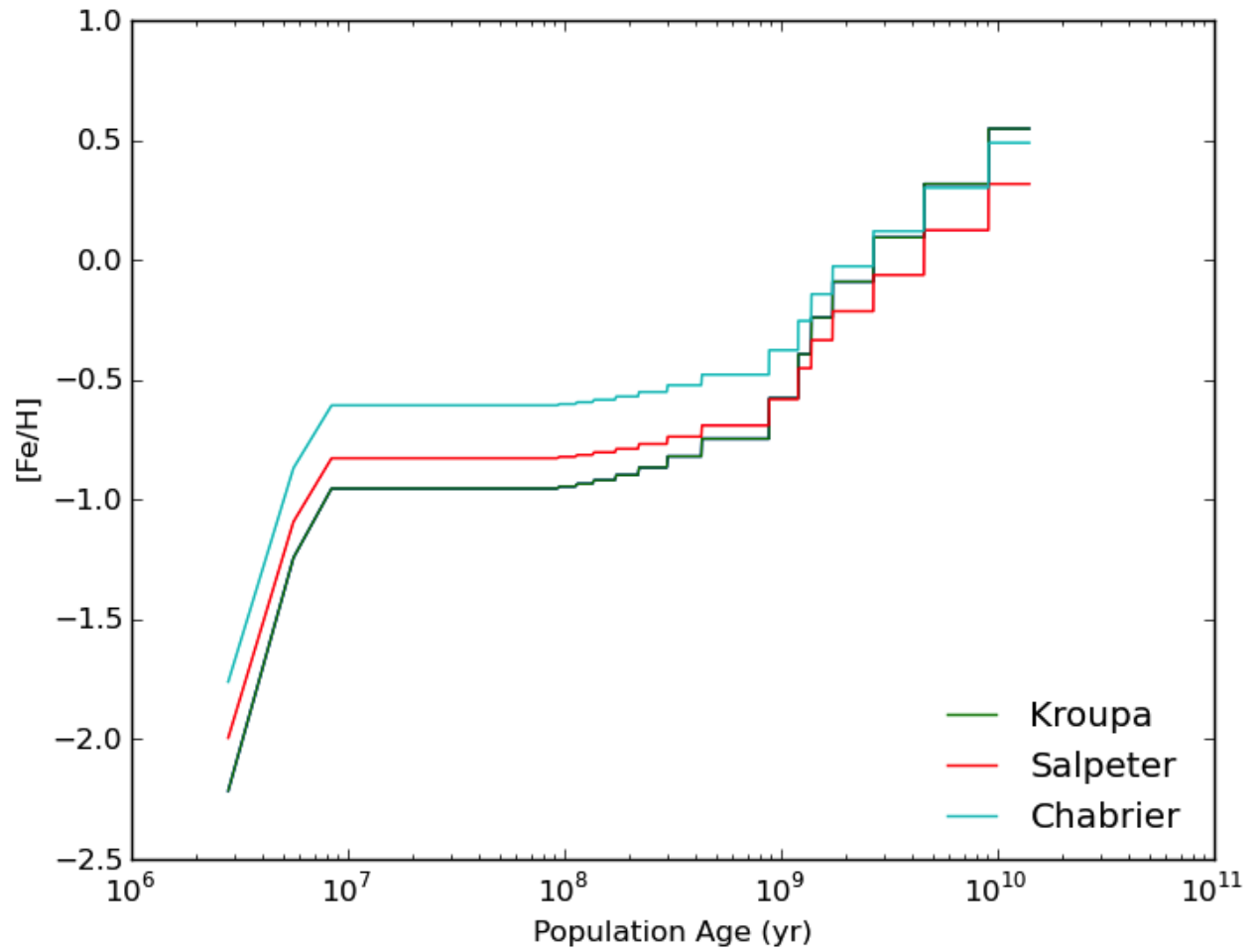


Figure 4.4: Metallicity, $[\text{Fe}/\text{H}]$ as a function of stellar population age for three IMFs.

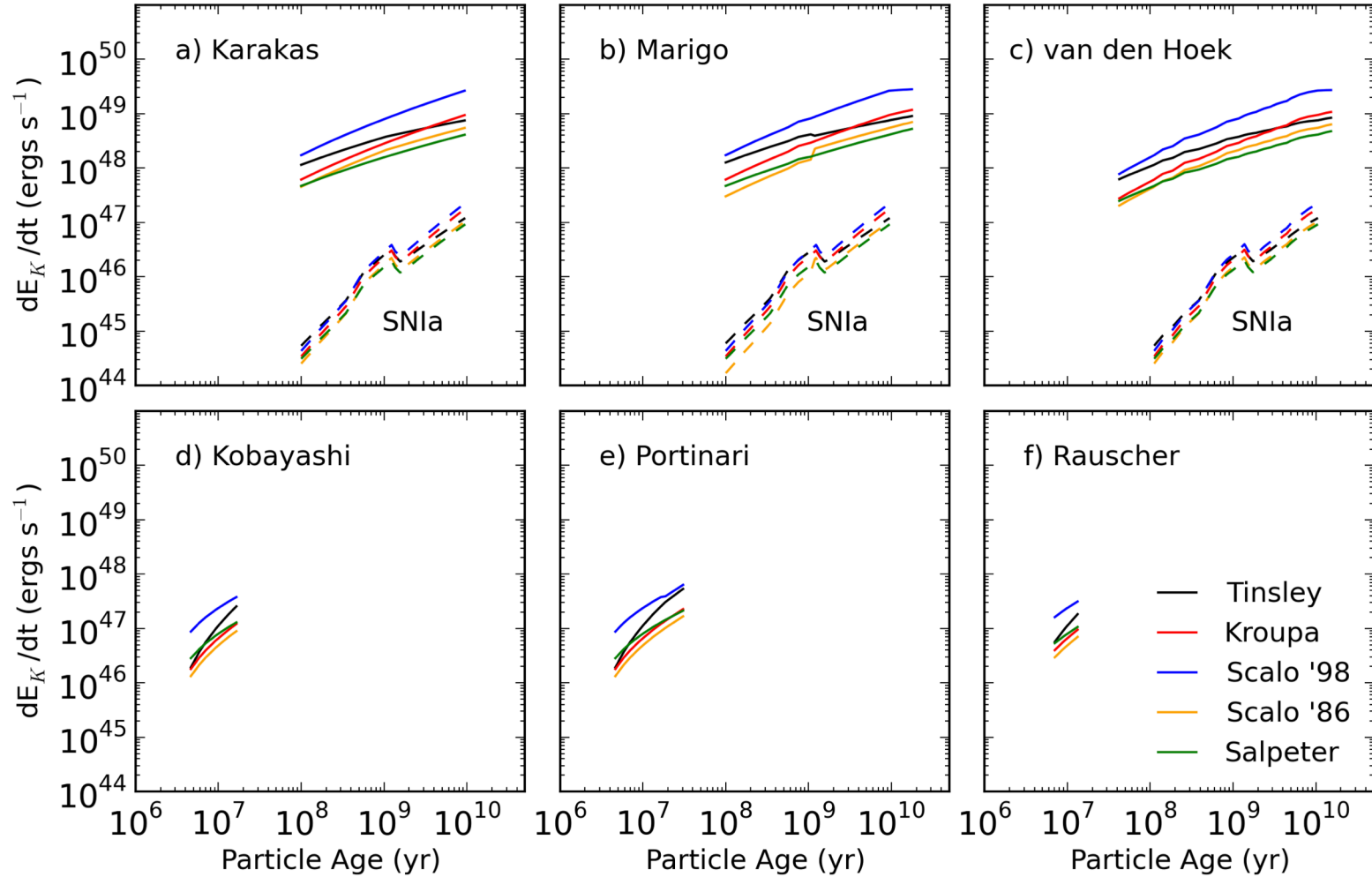


Figure 4.5: In addition to metals, an SSP ejects energy into the ISM. Here we show the energy feedback from an SSP over the lifetime of the stellar population from AGB stars, SNIa, and SNIi. The top row shows the energy feedback calculated from the AGB and SNIa yields of Karakas (2010), Marigo (2001), van den Hoek & Groenewegen (1997) and Iwamoto et al. (1999), while the bottom row shows the SNIi feedback calculated from the yields of Kobayashi et al. (2006), Portinari et al. (1998) and Rauscher et al. (2002). Each color corresponds to a different IMF.

4.1.1 Milky Way and Dwarf Galaxy Models

We have developed an isolated galaxy model with constant star formation with efficiency $\epsilon=0.04$, mass outflow from supernovae, and an exponentially decreasing primordial gas infall rate, $\tau=12$ Gyr. This infall rate matches that of the MW halo. Our model allows for choice of an IMF and initial values of $[X/Fe]$ (typically set to primordial abundances). With this, we compare star formation histories and chemical abundance trends of the Milky Way halo from the SEGUE dataset of 17,000 nearby stars (Yanny et al., 2009) and the numerous metal poor star

Furthermore, we have developed a model to include observed star formation rates of the local dwarf galaxy population. Orban et al. (2008) as shown in Figure 4.9. The dwarf galaxy model assumes a chemically homogenous stellar population with gas infall and outflow.

4.2 Variation in the Initial Mass Function

In a fully cosmological simulation, many generations of star particles form according to the chosen IMF. This mass distribution governs the proportions of high- to low-mass stars, and the ratios of elemental abundances, leading to an overall trend in galactic chemical properties. If we are to create a valid feedback model, it is essential to understand how variations in this selected IMF imprints onto the chemical patterns of stellar populations.

Each IMF, with the exception of the entirely log-normal form, represents an empirical fit to observations of main-sequence stars in the solar neighborhood. Whether the mass distribution of stars is universal, or varies with time or environment, is an open question; however, evidence suggests uniformity. Kroupa (2002) found that the IMF holds over a wide range of masses, from brown dwarfs to massive stars, present-day formation in molecular

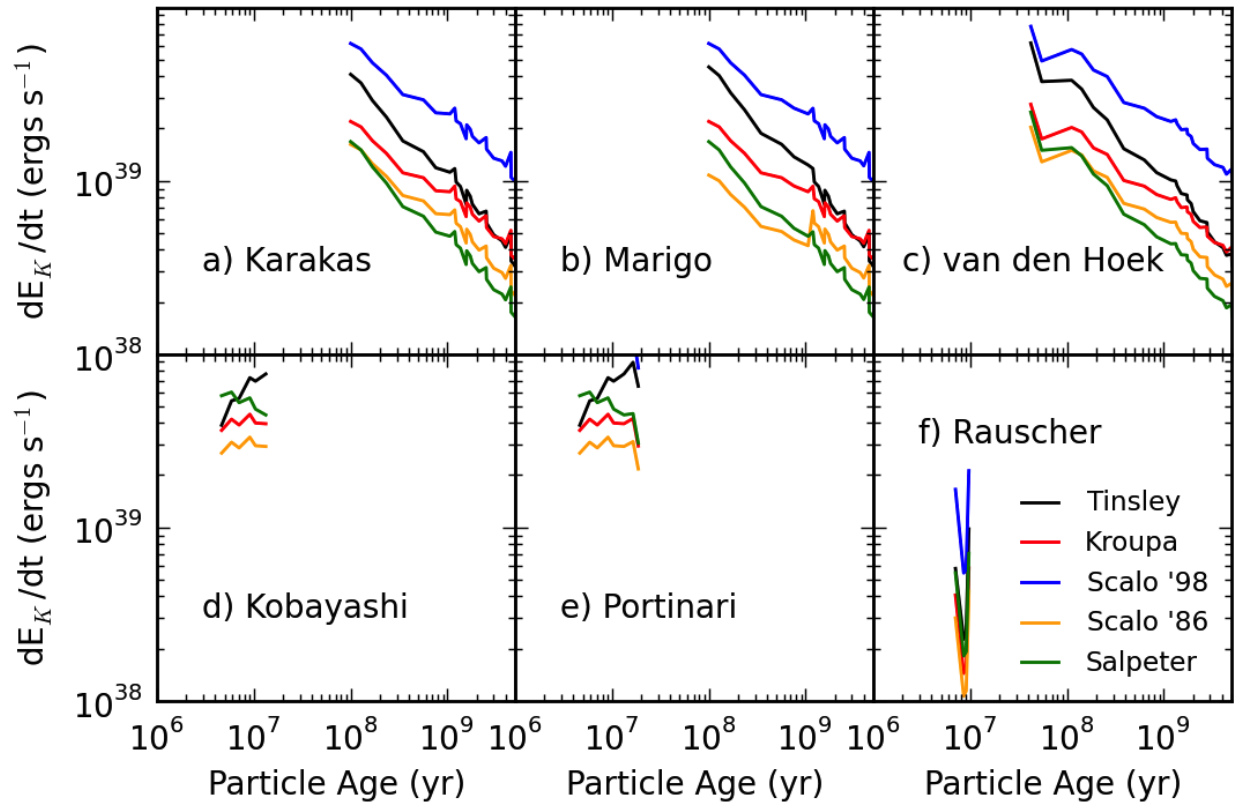


Figure 4.6: The time derivative of energy feedback from an SSP over the lifetime of the stellar population from AGB stars, SNIa, and SNIi. The top row shows the energy feedback calculated from the AGB and SNIa yields of Karakas (2010), Marigo (2001), van den Hoek & Groenewegen (1997) and Iwamoto et al. (1999). while the bottom row shows the SNIi feedback calculated from the yields of Kobayashi et al. (2006), Portinari et al. (1998) and Rauscher et al. (2002). Each color corresponds to a different IMF.

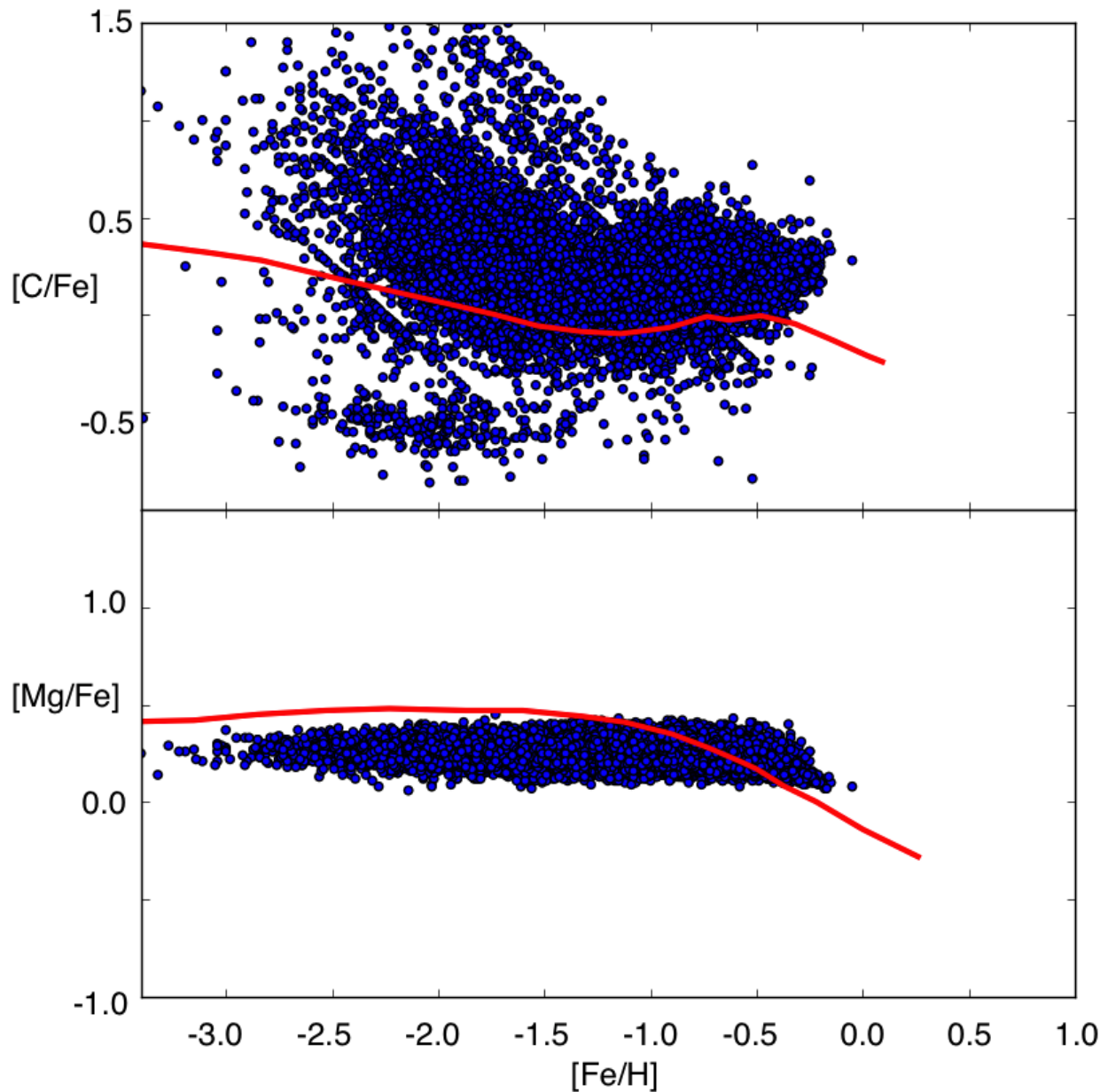


Figure 4.7: (top) $[\text{Fe}/\text{H}]-[\text{C}/\text{Fe}]$ distribution and (bottom) $[\text{Fe}/\text{H}]-[\text{Mg}/\text{Fe}]$ distribution for our simple stellar population model (red lines) compared with SEGUE dataset (blue circles) of nearly 17,000 nearby stars (Yanny et al., 2009). The SSP model assumes a Kroupa IMF, constant star formation with efficiency, $\epsilon=0.04$, mass outflow from supernovae, and exponentially decreasing primordial gas infall rate, $\tau=12$ Gyr. The red line represents $[\text{X}/\text{Fe}]$ calculated at the end of 14 Gyr for stellar particles with initial $[\text{Fe}/\text{H}]$ ranging from -5 to -1.

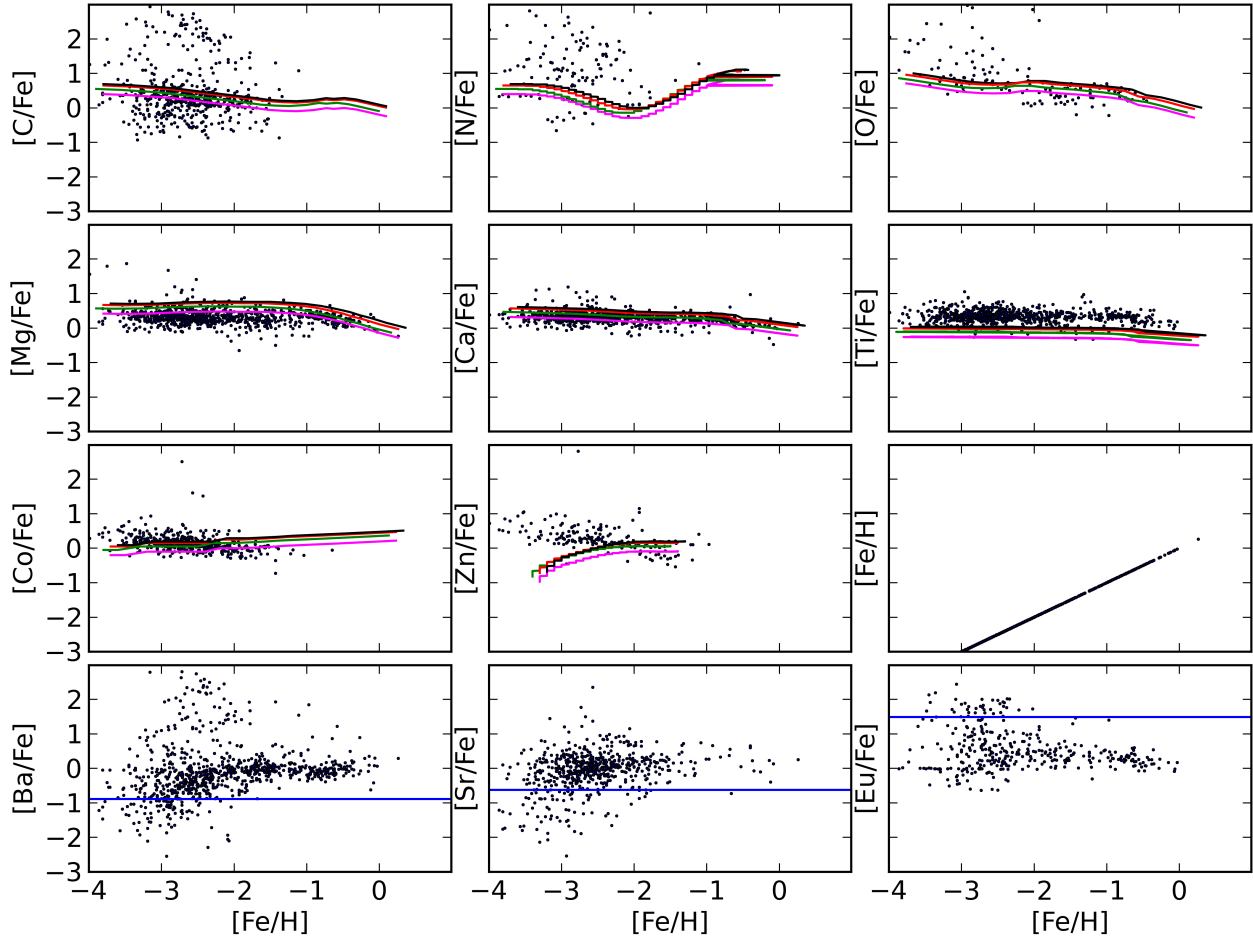


Figure 4.8: The $[X/Fe]$ distribution for our simple stellar population model compared with metal poor stars in the MW halo and dwarf galaxies as collected by Frebel (2010) and references therein. The SSP model assumes a Salpeter IMF, Kroupa IMF, Scalo IMF, or Tinsley IMF (black, green, red, magenta respectively) with constant star formation (efficiency, $\epsilon=0.04$), mass outflow from supernovae, and exponentially decreasing primordial gas infall rate, $\tau=12$ Gyr. The red line represents $[X/Fe]$ calculated at the end of 14 Gyr for stellar particles with initial $[Fe/H]$ ranging from -5 to -1. A blue horizontal line denotes a lower limit for neutron capture abundances from the SSP model.

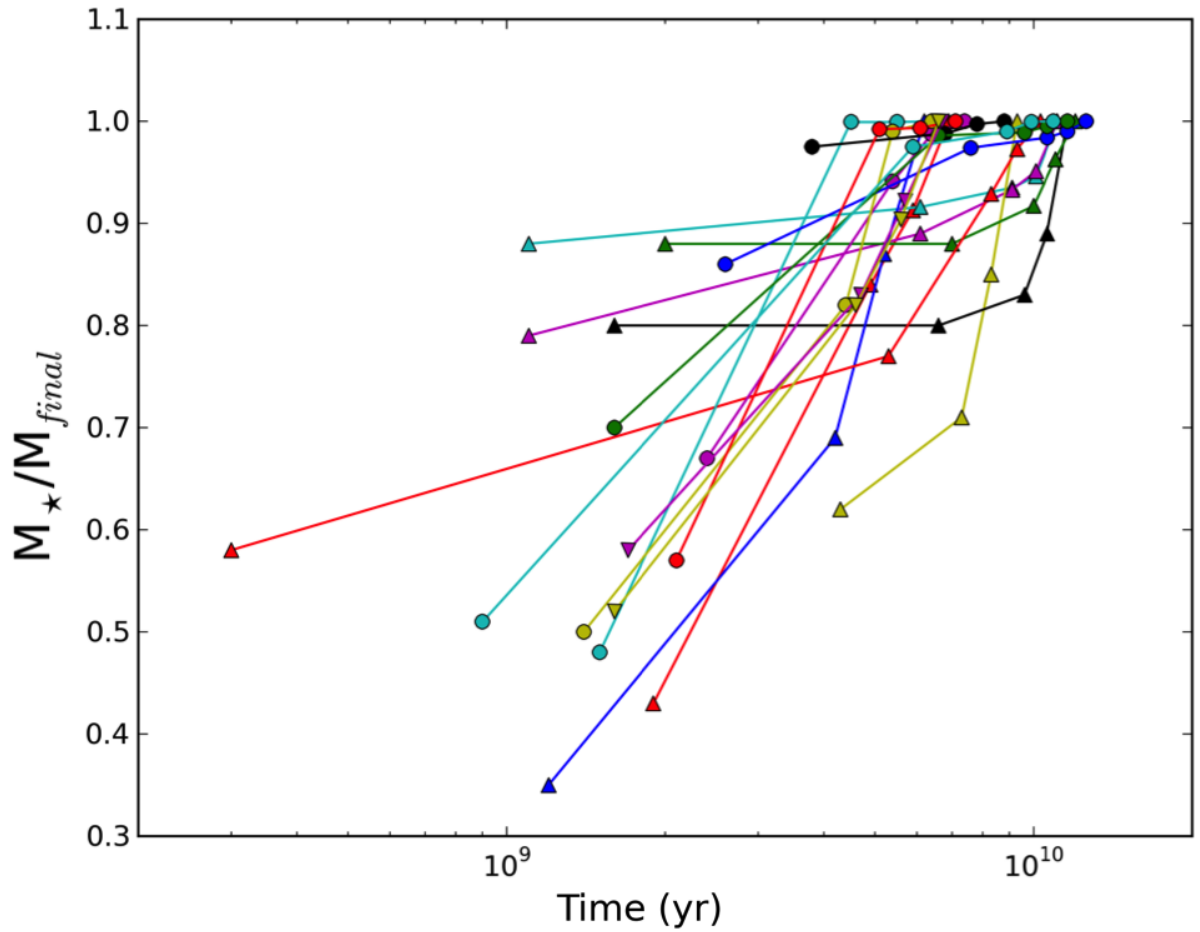


Figure 4.9: Star formation history of known satellite galaxies of MW within $1 h^{-1}$ Mpc of the host as parameterized by Orban et al. (2008).

clouds, dense formation in giant clouds, and throughout the most metal-poor Galactic halo stars. A simple test of the ubiquity of the IMF would be to search for systematic abundance variations amongst stellar populations. First and foremost, we need to recognize the influence an IMF has on the chemical history of a population. The currently considered IMFs vary most clearly at the low stellar mass end, where observations are lacking. The Salpeter (1955) and Scalo (1986) functions are steep below $2 M_{\odot}$, where metals become locked up in stars. The Scalo (1998) and Chabrier (2003) functions put more emphasis on intermediate-mass stars, which are the primary producers of carbon. Using only the empirical IMFs and several stellar-nucleosynthesis calculations, one can examine how large an effect IMF variation can have on the nucleosynthetic output of stellar populations as they age.

4.2.1 Varying the Characteristic Mass

The Galactic stellar IMF is usually fit by a power law at high mass ($M > 1 M_{\odot}$), with a rollover at low mass. The peak in the Galactic IMF is at $\sim 0.3 M_{\odot}$. We can think of this as a *characteristic mass* for star formation, M_c . Globular clusters and the Milky Way bulge have about the same mass range in the IMF plateau as local clusters. Since this same characteristic mass occurs for low-density and low-pressure regions, as well as for high-density and high-pressure regions, there must be some physical mechanisms whose interplay results in a constant characteristic mass (Elmegreen, 2009; Bastian et al., 2010).

The characteristic mass of the IMF may evolve at higher redshifts. Tumlinson (2006) and Tumlinson (2008) explore the implications of the thermal history of our universe on this characteristic mass. In the early cooling phase of collapse the temperature density relation can be expressed with a simple power-law dependence, $\rho = 10^{-18}(4.4K/T)^{3.7} \text{g cm}^{-3}$. The CMB temperature can be written as an explicit function of redshift, $T = 2.73K(1+z)$.

These two relations create, in effect, a floor limiting the minimum size of stars as a function of redshift in the early universe.

Several observations offer evidence for higher values of m_c . For example, Getman et al. (2007) has asserted that triggered star formation in globular clusters indicated preferential triggering by massive stars. van Dokkum (2008) found that early-type galaxies in the redshift range $0.02 < z < 0.83$ exhibit a flat IMF at $1M_\odot$, and may be redshift dependent. Narayanan & Davé (2012) suggested $M_c = 0.5(1 + z)^3$, with $\dot{M} = 0.5(1 + z)^{3-0.75z} M_\odot$. Komiya et al. (2007) consider the IMF of the most extreme metal-poor stars, which agrees with observations only when $M_c \sim 5M_\odot$. Our treatment of redshift-dependent IMFs will be discussed in Section 4.3.

If the characteristic or average mass of stars is variable in time, we can explore the implications of shifting the value of m_c and the transition between the power-law and log-normal segments of the Chabrier IMF, as presented in Section 3.2. This exercise is illustrated in Figure 4.11, using the IMFs shown in Figure 4.10. We have focused on the low-mass regime up to the middle of the AGB mass range. As expected, shifting this characteristic mass to higher masses results in higher stellar yields from the numerous low-mass stars. Although more ejecta are released into the ISM from these stars, this enrichment is delayed further, as the stars are long lived.

Adjusting the IMF such that the characteristic mass is shifted to higher values (from $m_c=0.079$ to $m_c=2.0$), we see the delayed onset of significant chemical enrichment as well as significantly more feedback, as much as 0.5 dex, at each SSP age for the AGB population. Chemical enrichment from the SNII population is simply shifted to higher stellar mass at each SSP age. The effect of varying the characteristic mass is most clearly seen in the ratios of elements. Figure 4.15 shows the history of [C/Fe], [N/Fe], [O/Fe], and [Mg/Fe] for two

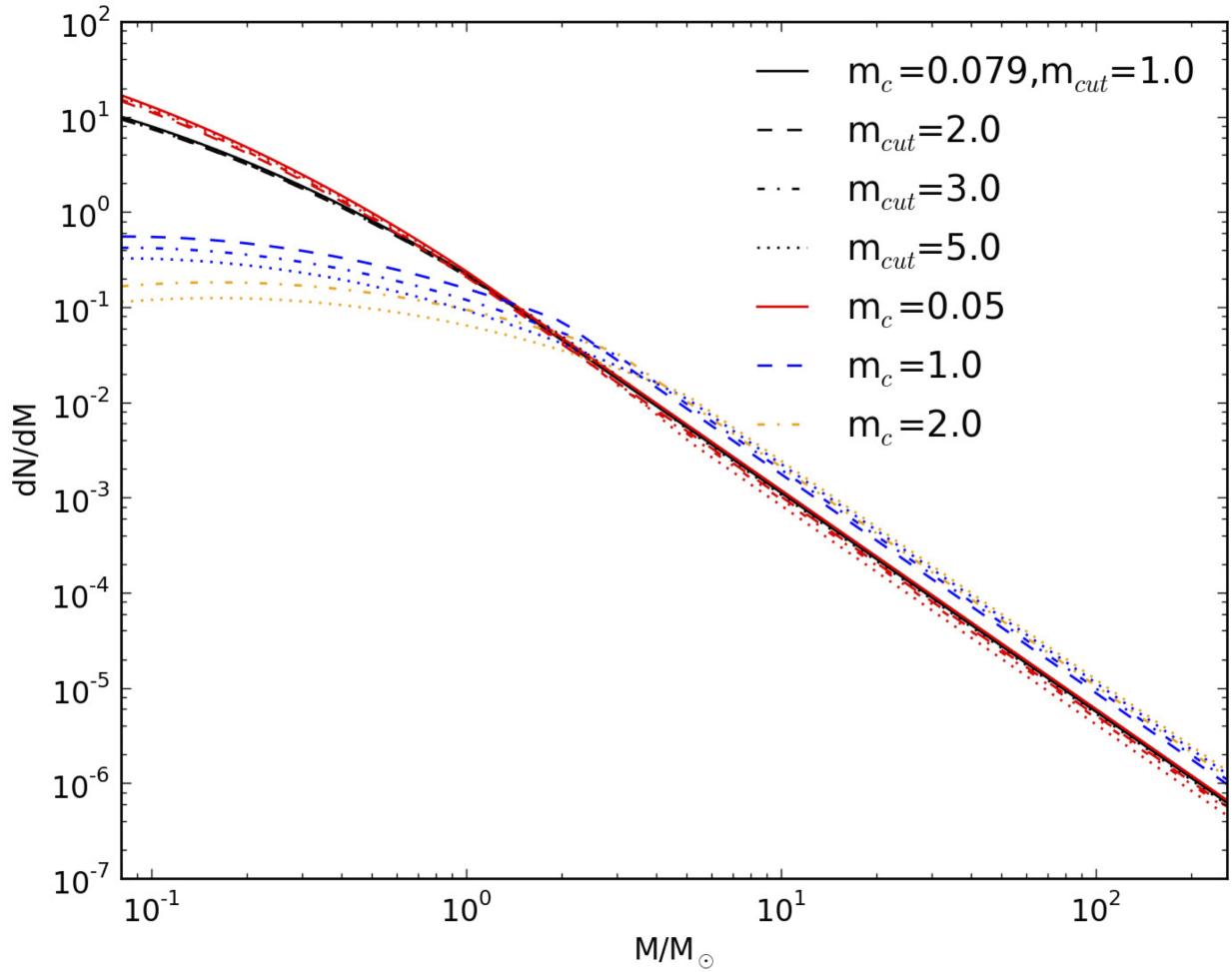


Figure 4.10: The characteristic mass, m_c , and mass cut, m_{cut} , between the log-normal and power-law function of the Chabrier IMF is varied, while keeping the overall normalization of the IMF constant. We explore the implications of varying these values on the IMF-weighted yields of AGB stars.

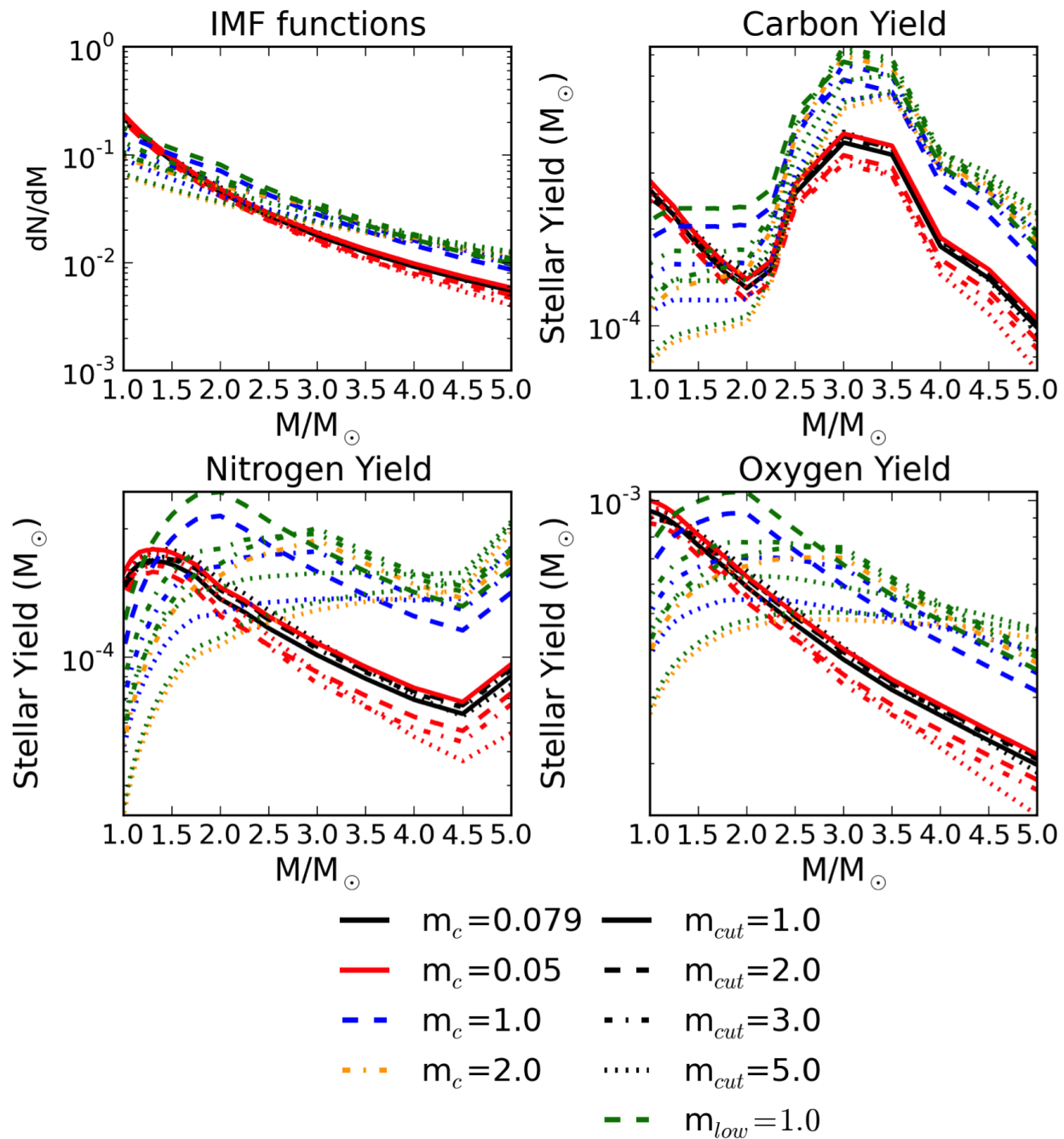


Figure 4.11: The first panel displays IMF forms of Figure 4.10 in the mass range of AGB stars. All IMFs are normalized to $1 M_{\odot}$ in the range 0.08 to $260 M_{\odot}$, except for the green lines, which have a lower mass limit of $1 M_{\odot}$. When the AGB stellar yields of Karakas (2010) are weighted with each IMF, we see variation in stellar ejecta up to 0.5 dex.

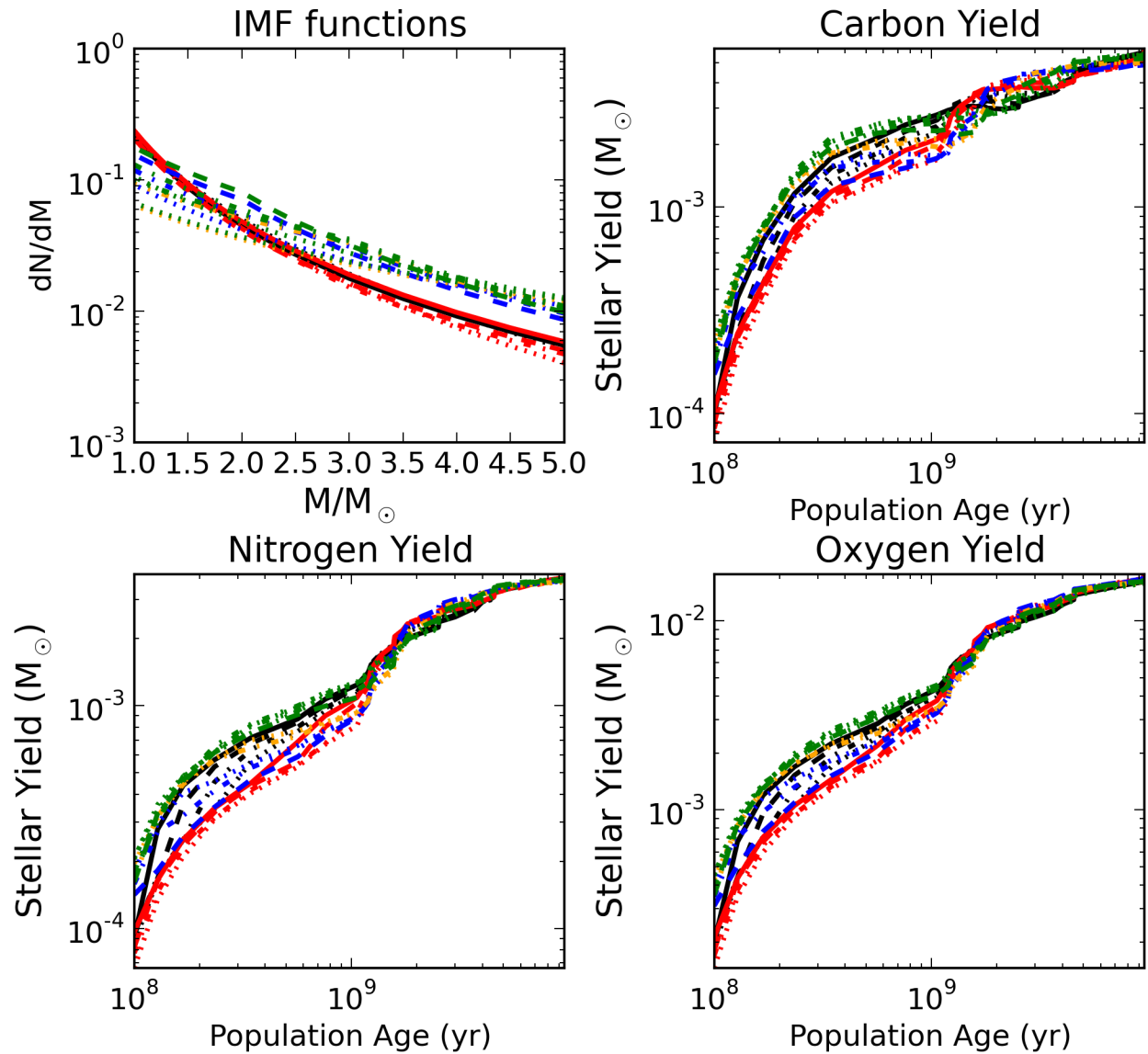


Figure 4.12: The first panel displays IMF forms of Figure 4.10 in the mass range of AGB stars. All IMFs are normalized to $1 M_{\odot}$ in the range 0.08 to $260 M_{\odot}$, except for the green lines, which have a lower mass limit of $1 M_{\odot}$. When the cumulative AGB stellar yields of Karakas (2010) are weighted with each IMF, we see significant variations in the chemical history. See Figure 4.11 for the legend.

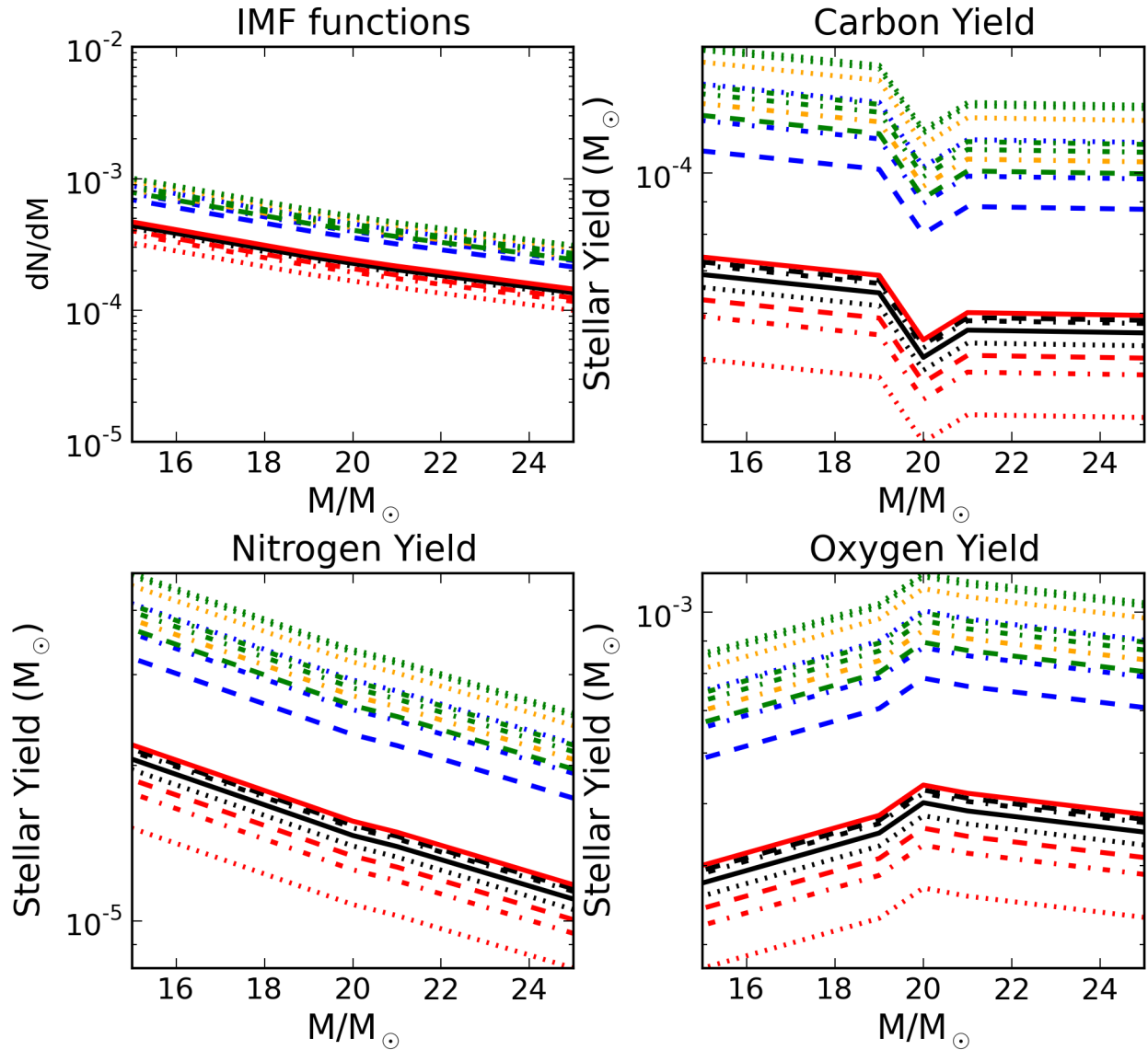


Figure 4.13: The first panel displays IMF forms of Figure 4.10 in the mass range of SNII. All IMFs are normalized to $1 M_{\odot}$ in the range 0.08 to $260 M_{\odot}$, except for green lines, which have a lower mass limit of $1 M_{\odot}$. When the SNII stellar yields of Rauscher et al. (2002) are weighted with each IMF, we see variation in stellar ejecta up to 1.0 dex. See Figure 4.11 for the legend.

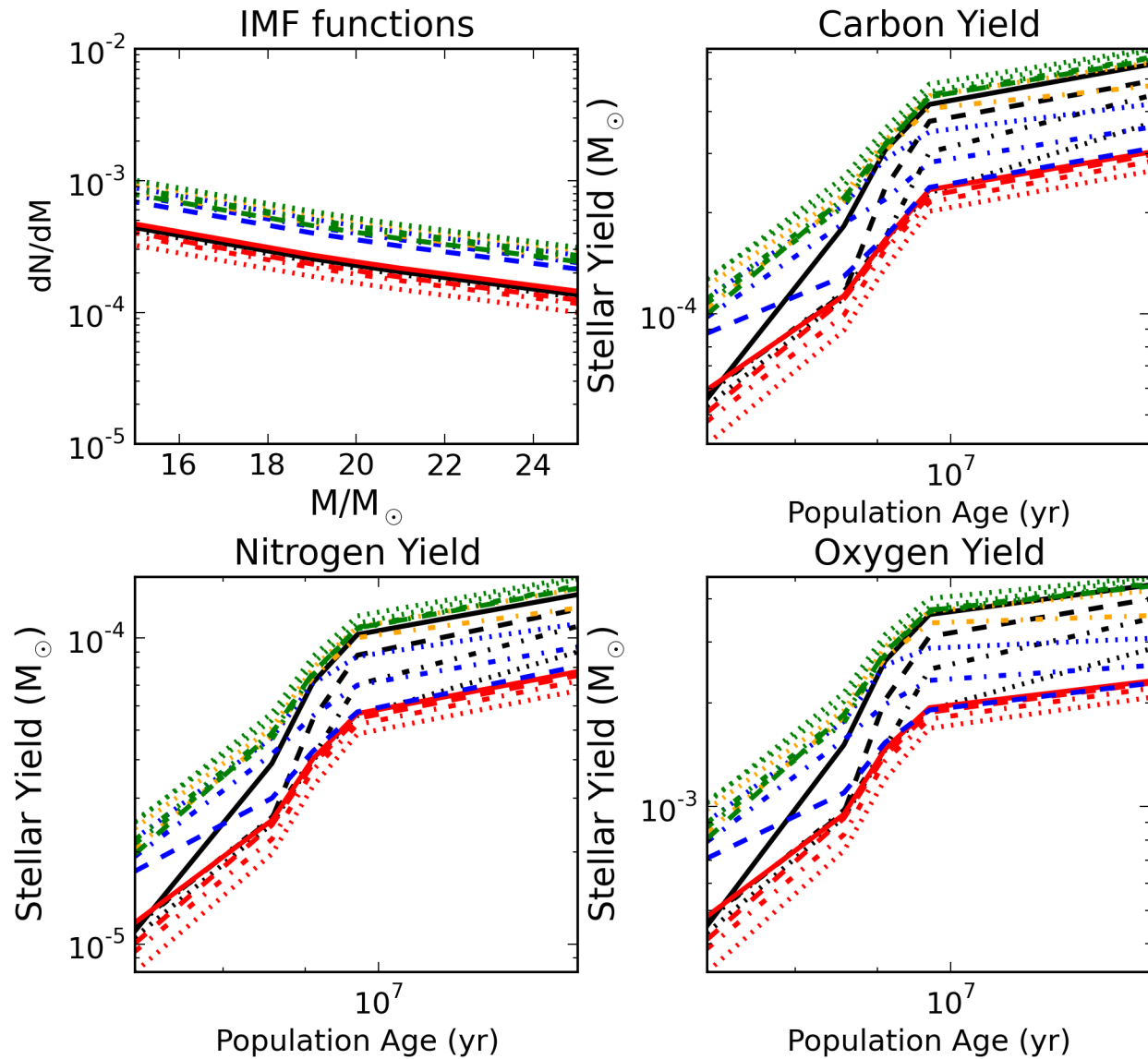


Figure 4.14: The first panel displays IMF forms of Figure 4.10 in the mass range of SNII. All IMFs are normalized to $1 M_{\odot}$ in the range 0.08 to $260 M_{\odot}$, except for the green lines, which have a lower mass limit of $1 M_{\odot}$. When the SNII stellar yields of Rauscher et al. (2002) are weighted with each IMF, we see significant variations in the chemical history. See Figure 4.11 for the legend.

distinct IMFs. The “local” IMF is the Chabrier IMF with the low characteristic mass of $0.079 M_{\odot}$, while the “high-mass” IMF has a characteristic mass of $2.0 M_{\odot}$. Over the history of the SSP, the high-mass IMF produces more C, N, O, and Mg with respect to Fe than the low-mass IMF SSP.

4.2.2 Varying the Stellar Yields

Each panel in Figure 4.16 shows a side-by-side comparison of the IMF-weighted yields of carbon from two sources of AGB yields. The first two panels show one yield source for all 5 choices of IMF. Rows 2 through 6 show each yield source overplotted for a single IMF choice. The shaded region denotes the spread of the ejected mass of the corresponding yield source due to the IMF choice. The ejected mass includes the mass of element that is not processed, in addition to that which is newly created. Each panel in Figure 4.17 shows the same comparison for a set of three SNII yield sets. This exercise has been repeated for each element in our set with available yields. Please see Appendix A for the full set of figures. If the spread due to the IMF choice is larger than the spread between the two yield sources, we may be able to discern between IMFs from observations. If the yield source spread is larger than the IMF spread, yield uncertainties make it impossible to extract the formation environment from observations. This is the case for carbon, the most poorly constrained of the chemical yields from stellar-nucleosynthetic calculations. In contrast, nitrogen (see Figure 4.18) is well understood and can be used as a tracer of the IMF in stellar populations.

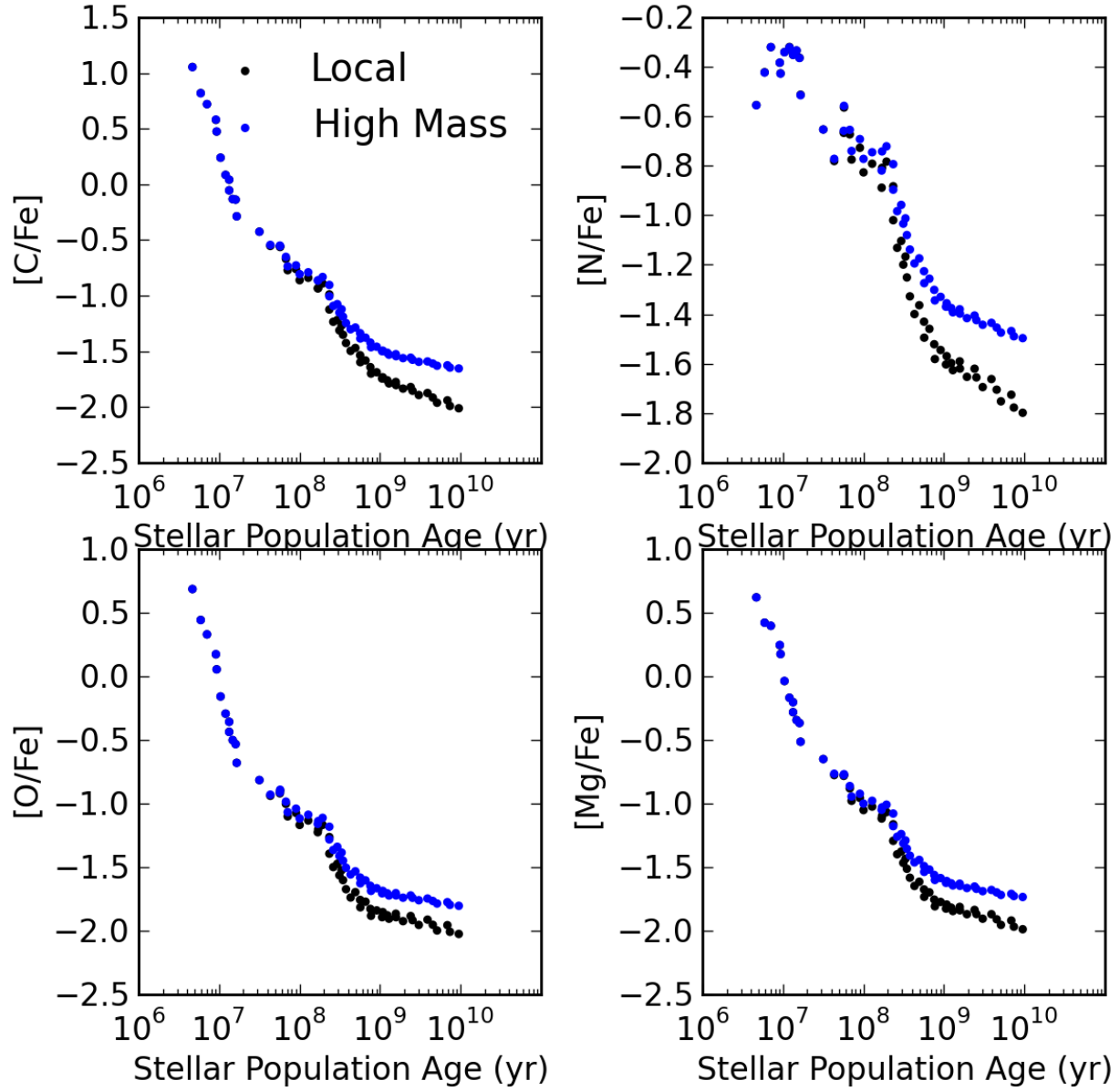


Figure 4.15: The history of $[C/Fe]$, $[N/Fe]$, $[O/Fe]$, and $[Mg/Fe]$ for two distinct IMFs. The “local” IMF is the Chabrier IMF with the low characteristic mass of $0.079 M_{\odot}$, while the “high-mass” IMF has a characteristic mass of $2.0 M_{\odot}$.

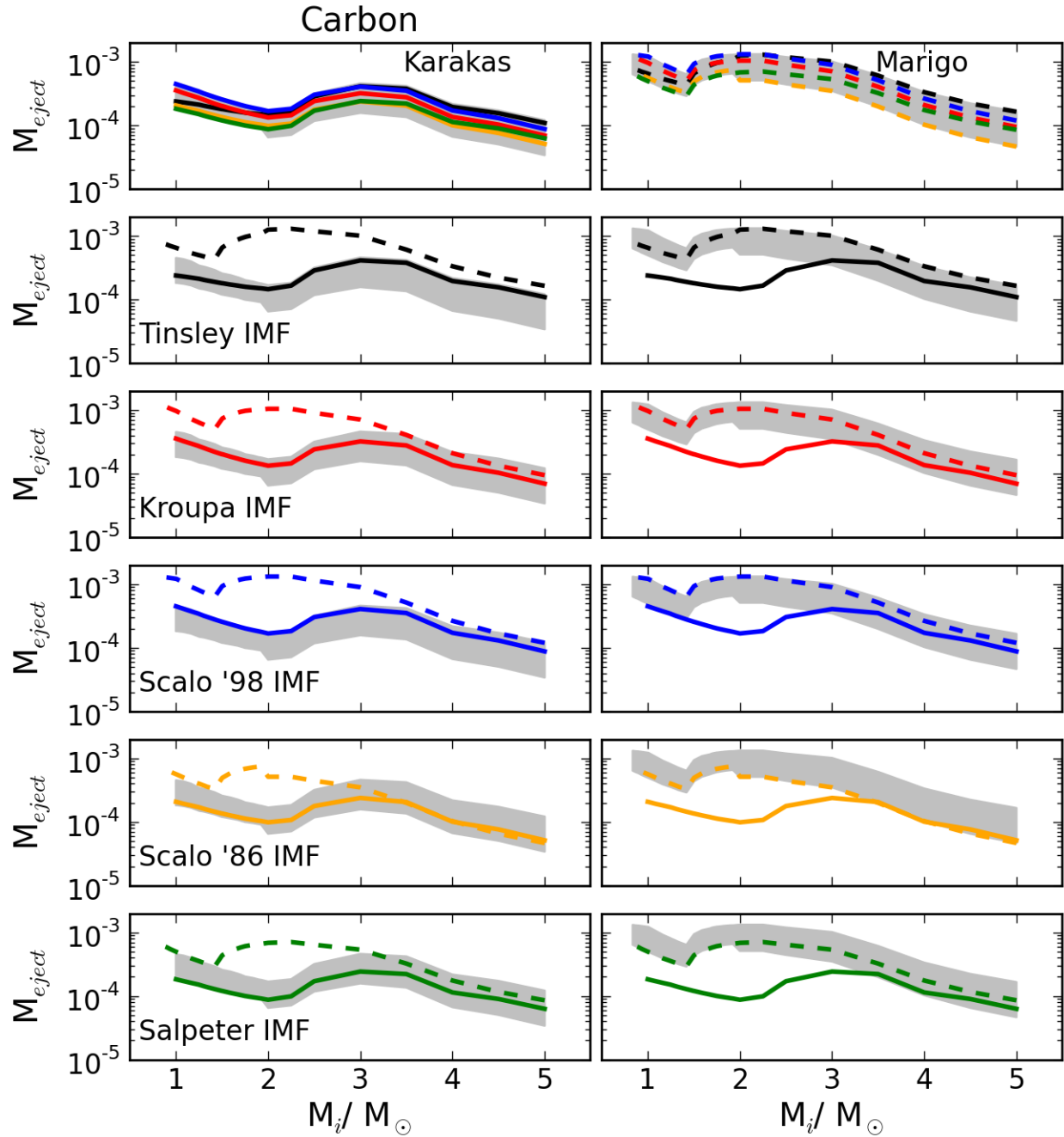


Figure 4.16: Each frame shows a side-by-side comparison of IMF-weighted Carbon yields from two sources, Karakas (2010) and Marigo (2001). First two panels show one yield source for all 5 choices of IMF. Rows 2 through 6 show each yield source overplotted for a single IMF choice. The shaded region denotes the spread of ejected mass of the corresponding yield source due to IMF choice. If the spread due to IMF choice is larger than the spread between two yield sources, we may be able to discern between IMFs from observations. If the yield source spread is larger than the IMF spread, yield uncertainties make it impossible to extract the formation environment from observations. See Section 3.2 for the functional forms.

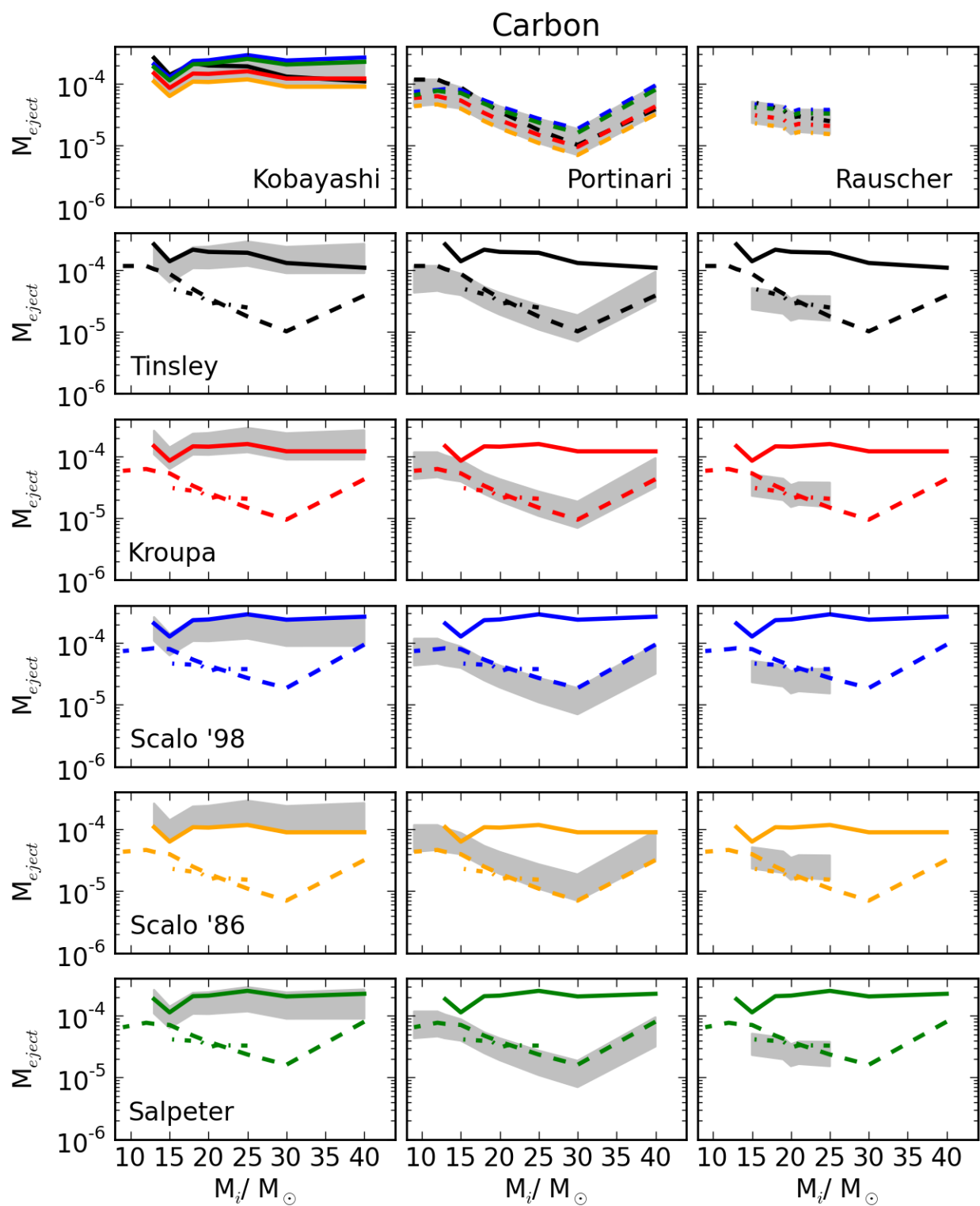


Figure 4.17: Same as Figure 4.16, but for the SNII yields of Kobayashi et al. (2006), Portinari et al. (1998), and Rauscher et al. (2002)

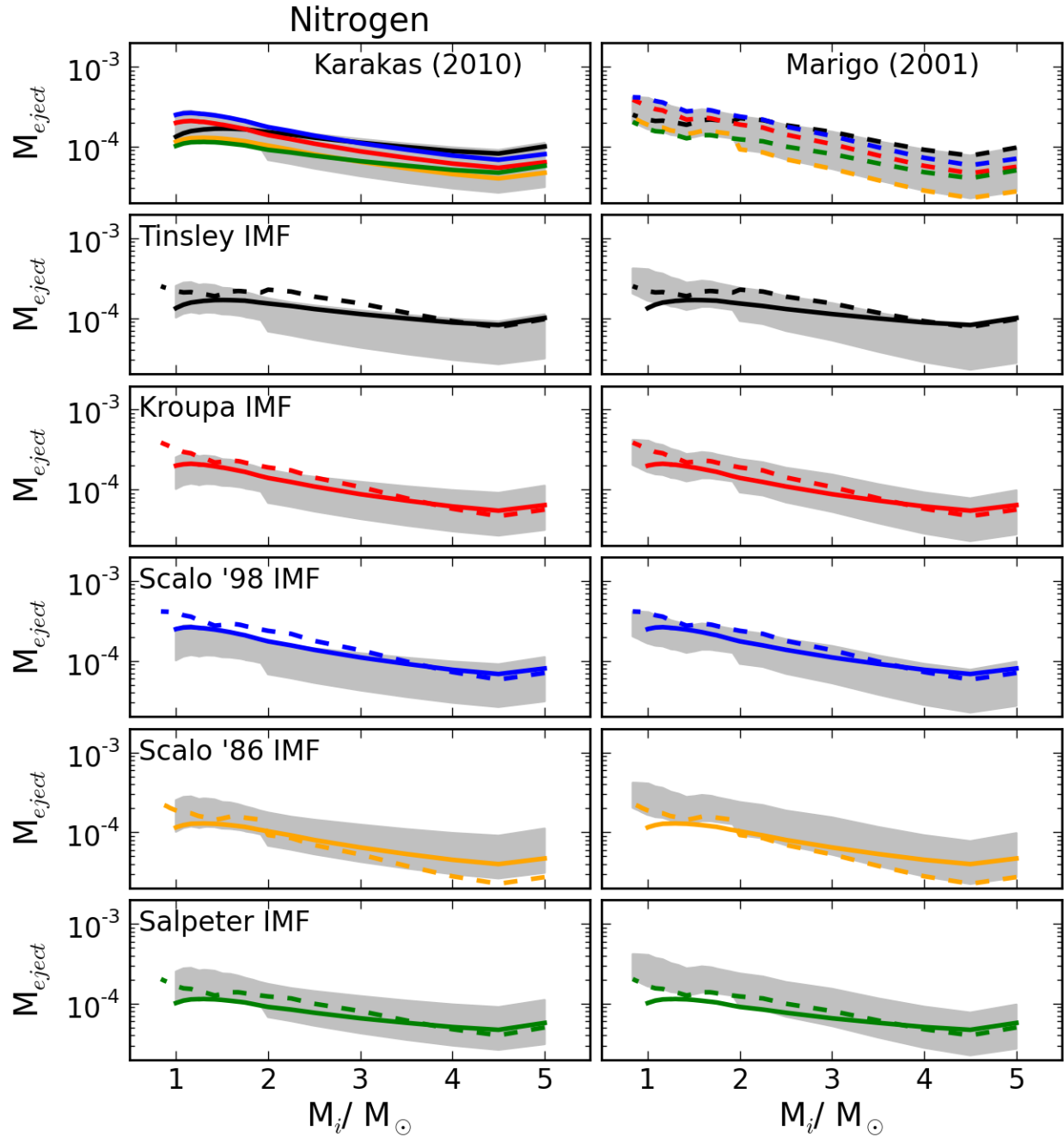


Figure 4.18: Each frame shows a side-by-side comparison of IMF-weighted Nitrogen yields from two sources, Karakas (2010) and Marigo (2011). First two panels show one yield source for all 5 choices of IMF. Rows 2 through 6 show each yield source overplotted for a single IMF choice. The shaded region denotes the spread of ejected mass of the corresponding yield source due to IMF choice. If the spread due to IMF choice is larger than the spread between two yield sources, we may be able to discern between IMFs from observations. If the yield source spread is larger than the IMF spread, yield uncertainties make it impossible to extract the formation environment from observations. See Section 3.2 for the functional forms.

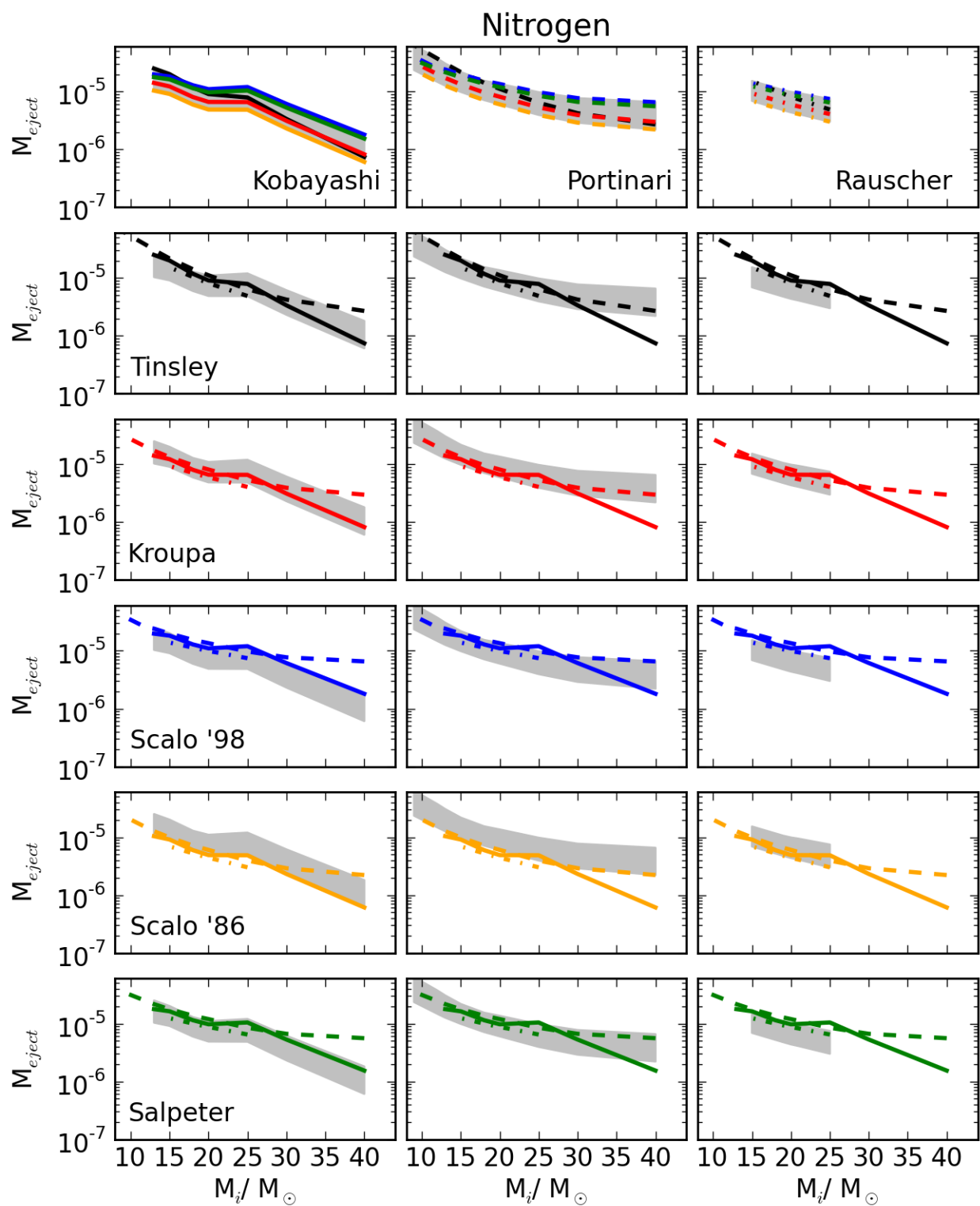


Figure 4.19: Same as Figure 4.16, but for the SNII Nitrogen yields of Kobayashi et al. (2006), Portinari et al. (1998), and Rauscher et al. (2002)

4.3 Implications for Numerical Models

We have provided a critical examination of publicly-available nucleosynthetic yield data from stellar evolution and nucleosynthesis simulations, spanning a wide range of stellar masses and metallicities, and by different authors. Our ultimate goal is to model GCE in the broad scope of cosmological hydrodynamical simulations, which means that we must synthesize these yield sets into a coherent model for chemical feedback. No single study covers all stars from brown dwarfs to the most massive giants, or all metallicities from the extremely metal-poor to the metal-rich case, but one can attempt to combine datasets to obtain maximal coverage of the parameter space of interest. The approximations made as a part of this process can lead to substantial uncertainties, and reduce the reliability of GCE models as predictors of stellar abundance patterns in the Galaxy.

An optimal set of stellar yields would be computed with the same input physics for a wide range of initial masses spanning ~ 0.08 to $260 M_{\odot}$, and would cover initial metal content from zero to a few times solar. This set should take into account all significant processes, which would affect the surface composition of stars during the entire stellar lifetime, such as hot bottom burning, formation of the ^{13}C pocket, rotational mixing, mass-loss rates, nuclear reaction rates, and SNe processes. As such a set of models may not be practical, given the specialized nature of most stellar evolution codes, we can drive down systematic uncertainties by understanding the effect that insufficient data has on the resulting GCE models.

4.3.1 Effects of Coarse Mass Grids

Within a given published set of yields, it is reasonable to interpolate between masses. However, problems arise when patching together yields of entirely different stellar mechanisms.

The gap between intermediate-mass and high-mass stars, roughly 8 to 11 M_{\odot} or 6 to 13 M_{\odot} , is particularly troublesome, due to the uncertain nature of sAGB stars. Taking the IMF into consideration, these stars are responsible for $\sim 30\%$ of He-production. On the high-mass end, many yield sets terminate after 40 M_{\odot} , while a complete sampling of the IMF requires extrapolation up to 260 M_{\odot} . Figure 4.20 demonstrates the problem which arises from coarsely gridded yield data.

The yields input to cosmological simulations are interpolated within the individual sets of AGB yields, SNII yields, and SNIa yields. We can degrade the data by removing half of all available yields (equally split between each major stellar component) and calculate the fractional change in the overall ejected mass of a specific element; $(M_{ej}^{full} - M_{ej}^{half}) / M_{ej}^{full}$. This exercise is illustrated in Figure 4.22. A negative change means a net over-production of the element due to smoothing over the degraded data, while a positive change means a net under-production of the element. We see, with each of carbon, nitrogen, and oxygen, over- and under-productions up to 5% due to this simple exercise. It is unknown how much our calculations of chemical enrichment history will improve with additional data points, since we can only remove rather than create inputs.

4.3.2 Effects of Coarse Metallicity Grids

Models used to compute yields implicitly assume relative abundances for heavy elements are initially solar. A full treatment would calculate yields tabulated in a space with dimensionality equal to the number of elements. Practical considerations require a discrete set of initial stellar abundances, typically characterized by an overall metal fraction or metallicity. In this work, as is commonly done, we consider only published yields for a subset of initial stellar metallicities. We set the solar value to $Z=0.02$, sub-solar to $Z=0.004$ ($0.2 Z_{\odot}$), and

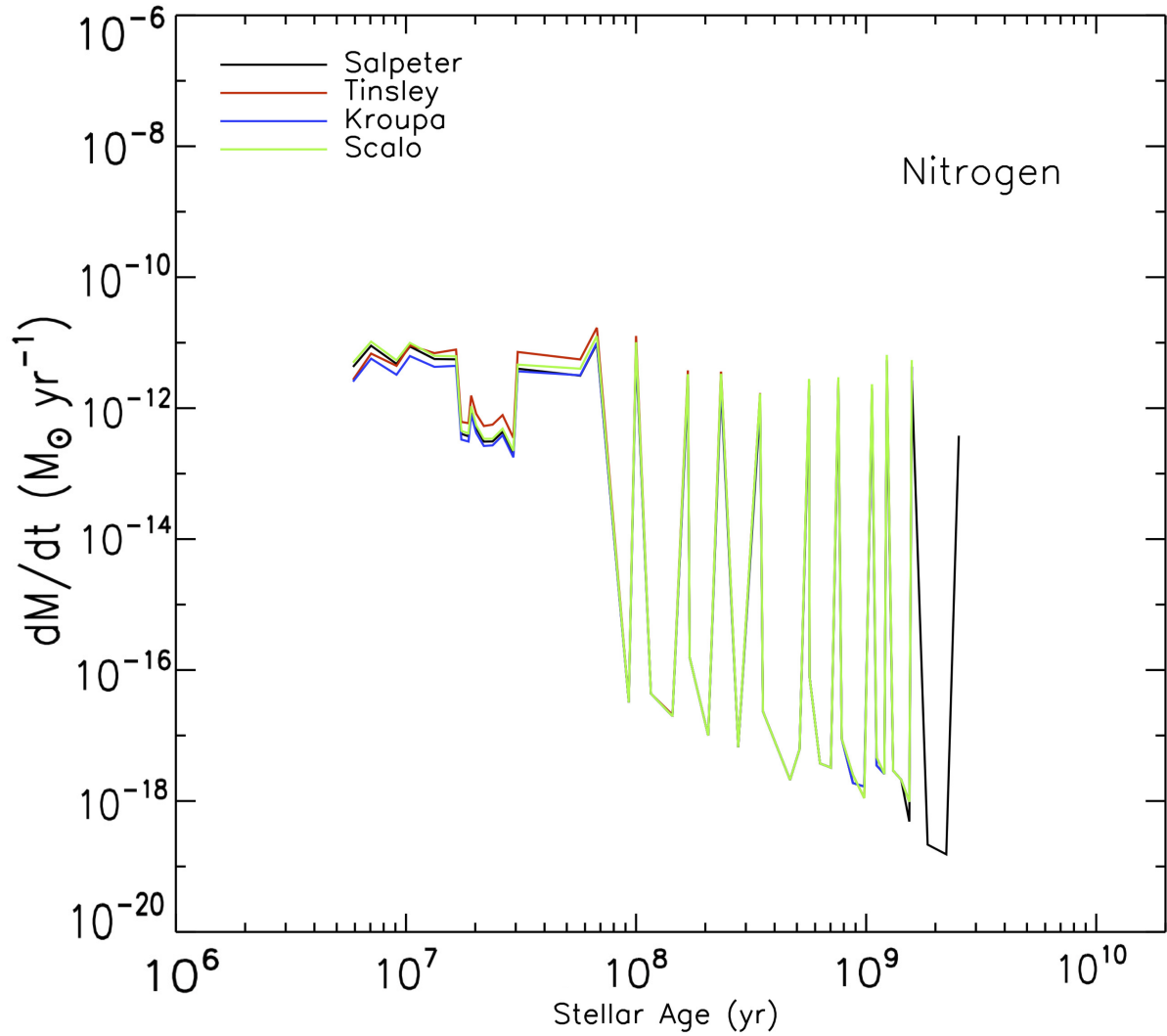


Figure 4.20: An illustration of the problem of coarse mass grids with Nitrogen yield data. When elements are only ejected at specific intervals (e.g., when a $10 M_{\odot}$ star dies, then when a $15 M_{\odot}$ star dies), there are regions in time where mass should be ejected, but is ignored.

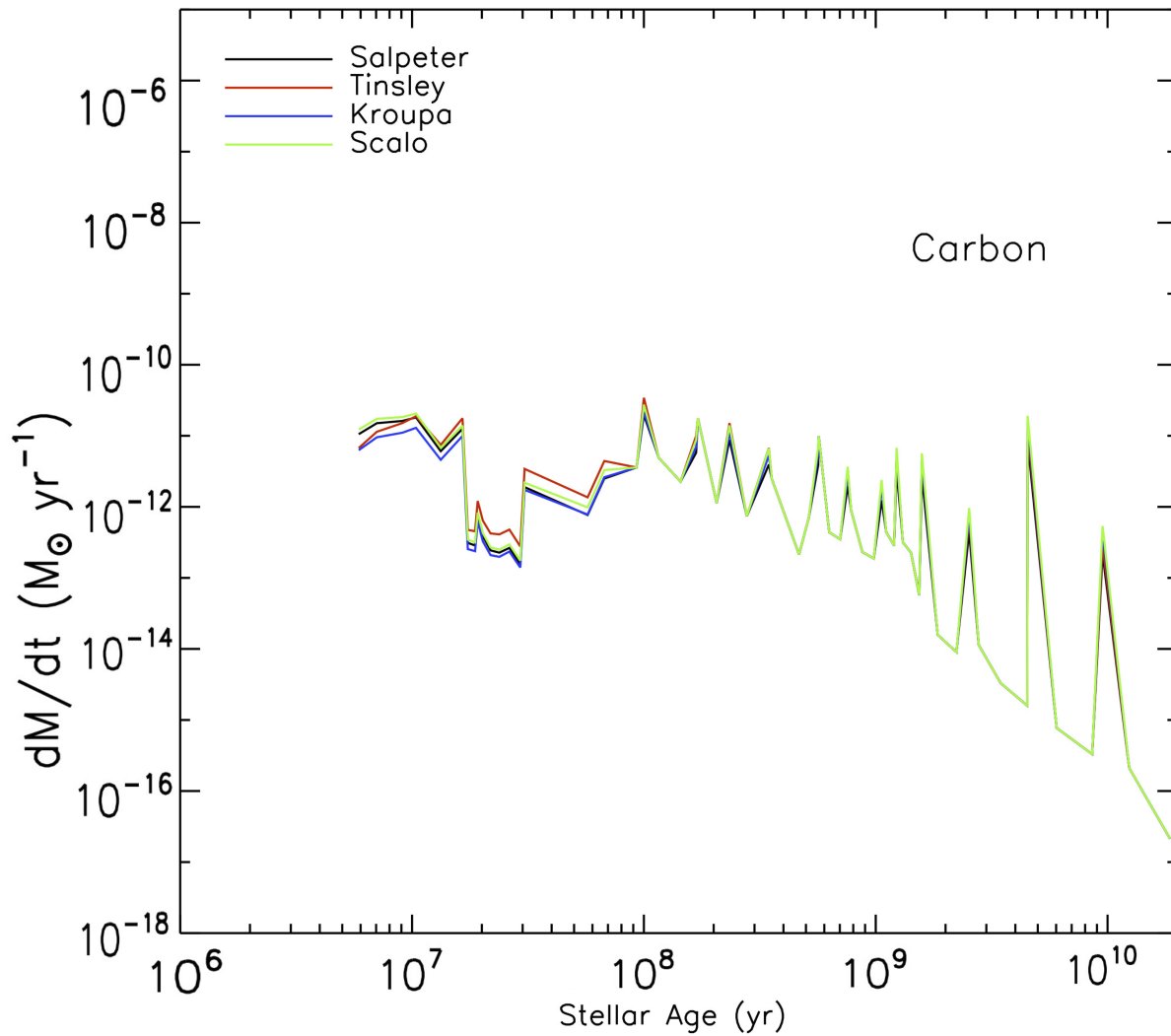


Figure 4.21: An illustration of the problem of coarse mass grids with Carbon yield data. When elements are only ejected at specific intervals (e.g., when a $10 M_{\odot}$ star dies, then when a $15 M_{\odot}$ star dies), there are regions in time where mass should be ejected, but is ignored.

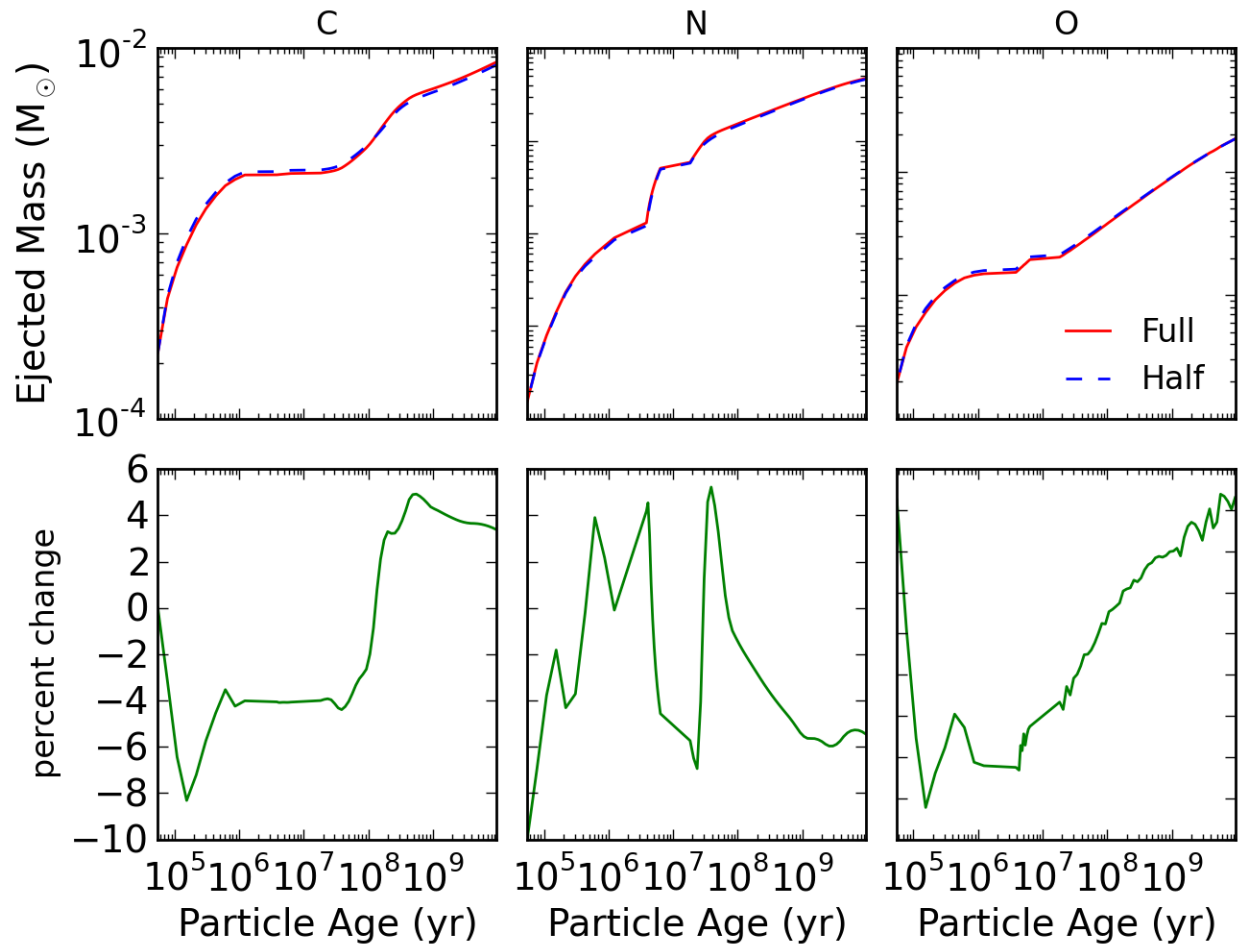


Figure 4.22: The top panel shows the integrated chemical history of carbon, nitrogen, and oxygen over the course of a simple stellar population lifetime. The solid red line shows the chemical history using the full set of available yields for AGB, SNII, and SNIa stars while the blue dashed line is the same calculation performed with the yield data degraded by 50 percent. The bottom panel shows the fractional change between the two calculations. A negative change means a net over-production of the element due to smoothing over the degraded data, while a positive change means a net under-production of the element.

super-solar to $Z=0.05$ ($4 Z_{\odot}$). While higher and lower metallicity yields are available from some groups, these values were the only ones consistent across the entire range of stellar nucleosynthetic sites.

For most nuclides, the yields computed for massive stars of solar metallicity by different authors are in agreement, within a factor of two. The discrepancies among different groups are more severe towards lower metallicities, not only for secondary elements (as expected), but also for some primary elements whose nucleosynthesis depends on earlier stellar evolutionary processes such as mass loss and mixing. In addition, it has been suggested that the explosion energy of core collapse supernovae is a function of metallicity (Nomoto et al., 2006). A lack of nucleosynthetic yield sets with sufficiently large metallicity ranges or non-scaled-solar initial values precludes the possibility of exploring this further at present.

Chapter 5

Post-Processing Cosmological Simulations with Chemical Evolution Models

Our model of galactic chemical evolution has been used to post-process data from the Enzo simulation run by Wise et al. (2012). The purpose of the calculation was to study the formation of the first metal-enriched galaxies. We have chosen to post-process these simulations to explore in greater detail the nucleosynthetic evolution of the stellar populations and interstellar/intergalactic medium, and to compare directly to the chemical abundances of the Milky Way stellar halo and dwarf spheroidal galaxy stellar populations.

5.1 Simulation Setup

The simulation modeled a comoving volume of 1 Mpc/h with a root grid of 256^3 cells. The same number of dark matter particles were used, resulting in a particle mass of $1840 M_{\odot}$ and ensuring that the smallest halos of interest (so called “mini halos”) are resolved by at least 100 dark matter particles. The simulation was initialized at $z = 130$ with cosmological parameters from the seven year Wilkinson Microwave Anisotropy Probe (WMAP7); $\Omega_M =$

0.266, $\Omega_\Lambda = 0.734$, $\Omega_b = 0.0449$, $h = 0.71$, $\sigma_8 = 0.81$, and $n = 0.963$ (Komatsu et al., 2011). The simulation was stopped at $z = 7$ to prevent large scale modes from entering the nonlinear growth regime.

Star formation was tracked independently for both metal enriched, Pop II, and primordial, Pop III, stars which were distinguished by metallicity alone where Pop II stars were formed from gas with $[Z/H] > -4$. Pop II star formation proceeded according to the prescription set by Wise & Cen (2009) where each star particle represents a single star. In this model, a star particle forms when a cell has all of the following has been met:

1. An overdensity of 5×10^5 ($\sim 10^3 \text{ cm}^{-3}$ at $z = 10$),
2. A converging gas flow ($\nabla \cdot \mathbf{v}_{\text{gas}} < 0$), and
3. A molecular hydrogen fraction $f_{\text{H}_2} > 5 \times 10^{-4}$.

If multiple cells meet the star particle formation criteria within 1 pc, only one Pop III star particle with the center of mass of these flagged cells is formed to ensure that one massive star is created per metal-free molecular cloud. Stellar mass is determined by randomly sampling from an IMF with a functional form of

$$f(\log M)dM = M^{-1.3} \exp \left[- \left(\frac{M_{\text{char}}}{M} \right)^{1.6} \right] dM. \quad (5.1)$$

After the star particle forms and its mass is randomly sampled from the IMF, an equal amount of gas is removed from the computational grid in a sphere that contains twice the stellar mass and is centered on the star particle. The star particle acquires the mass-weighted velocity of the gas contained in this sphere.

Pop II star formation also follows Wise & Cen (2009) without condition 3 (described

above). Unlike Pop III stars where a star particle represents a single star, Pop II star particles represent a stellar ensemble with stellar masses distributed according to an assumed IMF. Once a star particle is formed, the sphere surrounding it is given a uniform density and temperature to approximate the conditions of an HII region. Any potential stars within 10 pc of each other are merged as with the Pop III stars. They set the minimum mass of a star particle to $m_{\star,\min} = 1000 M_{\odot}$. If the initial mass does not exceed $m_{\star,\min}$, the star particle does not provide any feedback and continues to accrete until it reaches $m_{\star,\min}$. Typical halos from this simulation are shown in Figure 5.2. The first row shows gas temperature for a halo with intense star formation (top) and low star formation (bottom). Subsequent rows show gas density and metallicity. The measured global star formation rate for both Pop II and Pop III stars is shown in Figure 5.1. The Pop III rates are nearly constant at a rate of $5 \times 10^{-5} M_{\odot} \text{ yr}^{-1} \text{ Mpc}^{-3}$ after 350 Myr while formation of Pop II stars continues to increase exponentially.

5.2 Chemical Enrichment

Four chemical species are tracked in this model: hydrogen, carbon, magnesium, and iron. $[\text{Fe}/\text{H}]$ is a standard metric of metallicity, while magnesium is the most easily observed of the alpha elements, and provides a relatively reliable tracer of the entire family of alpha elements. The recent characterization of a class of carbon-enhanced metal poor (CEMP) stars (Carollo et al., 2012) makes carbon an element of particular interest in studying galactic chemical evolution.

The fundamental assumption made in the chemical enrichment from Population III stars is that they end their lives as Type II SNe (SNII). In an effort to remain agnostic about the

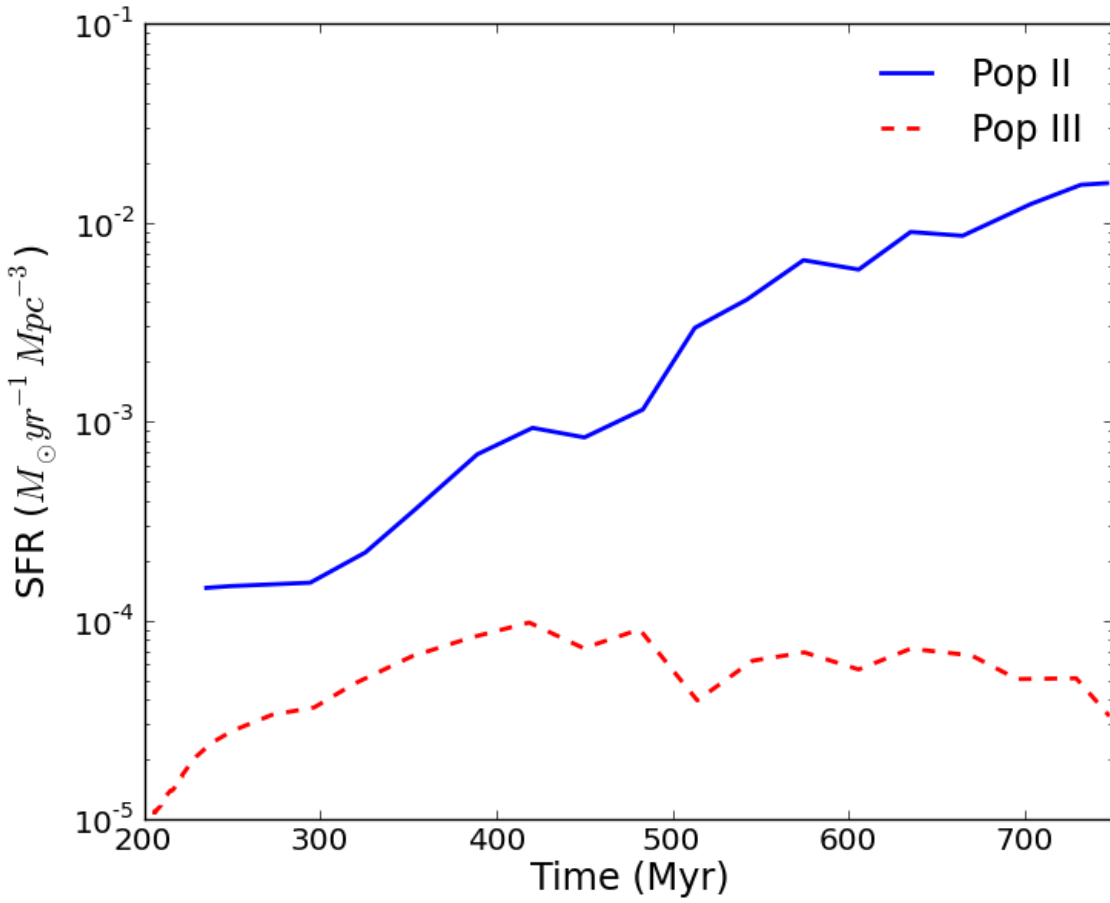


Figure 5.1: The global star formation rate of Pop II (blue, solid) and Pop III (red, dashed) stars in the Enzo simulation.

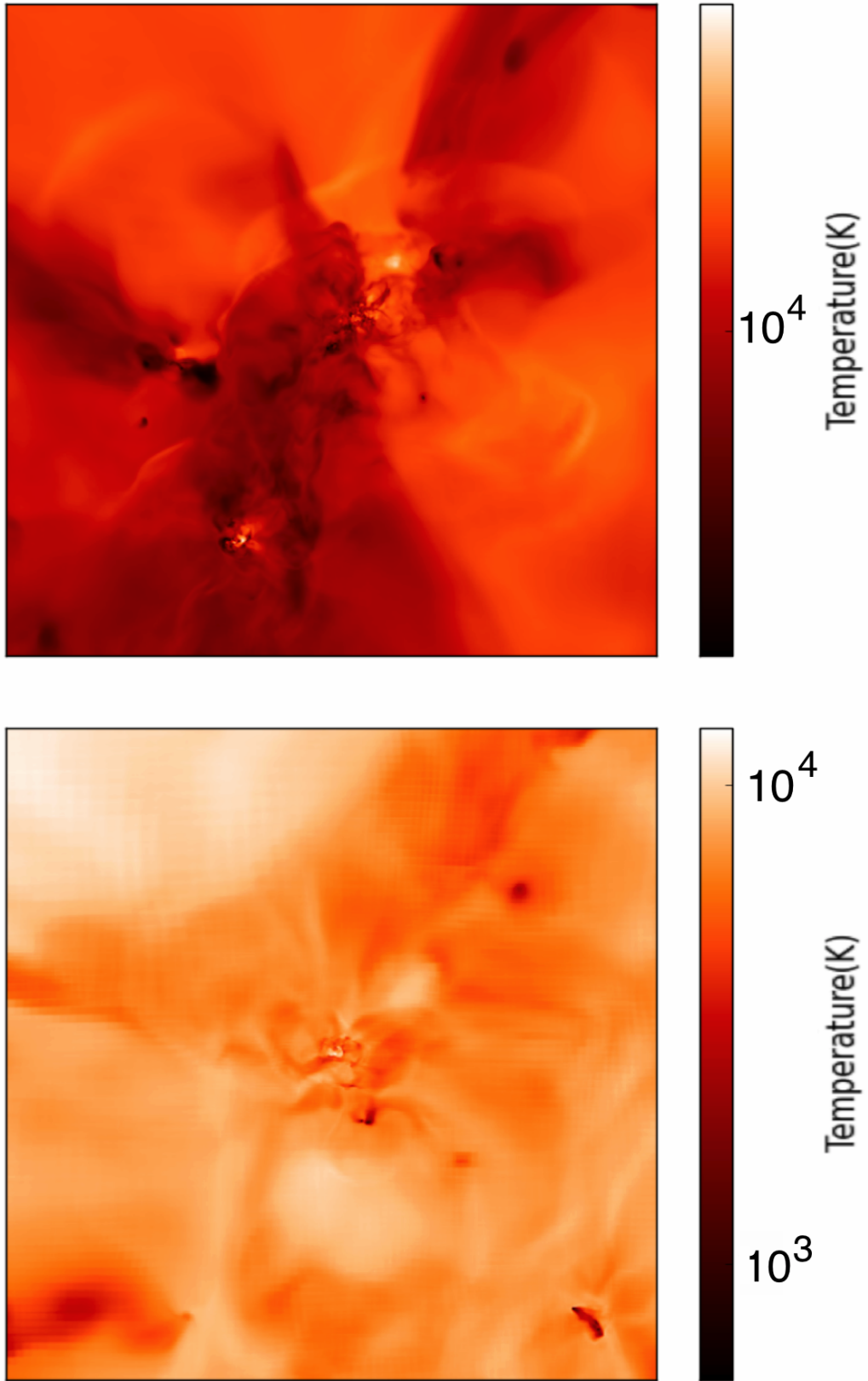


Figure 5.2: Temperature for a halo with intense star formation (top) and low star formation (bottom) at $z \approx 7$.

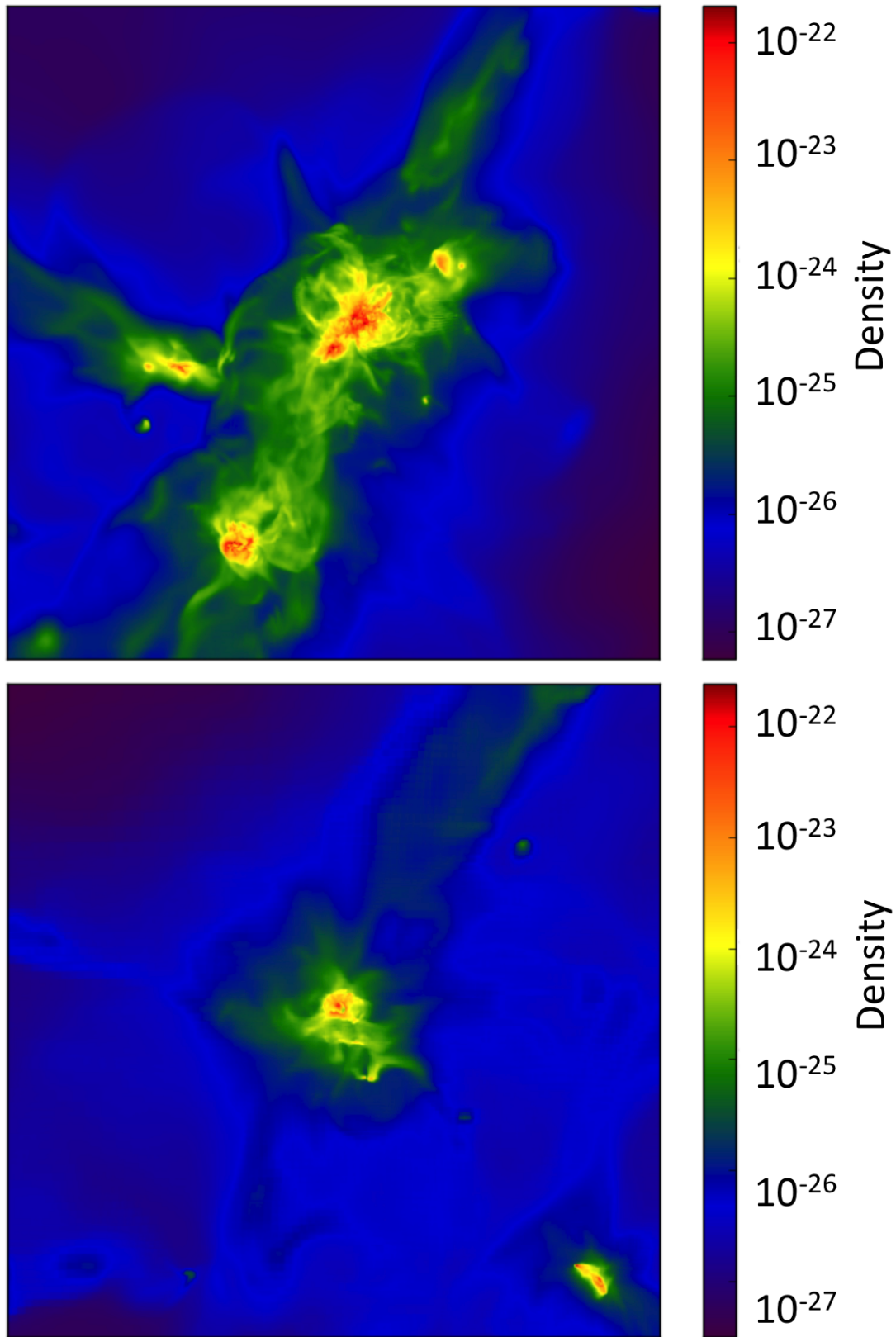


Figure 5.3: Density for a halo with intense star formation (top) and low star formation (bottom) at $z \approx 7$.

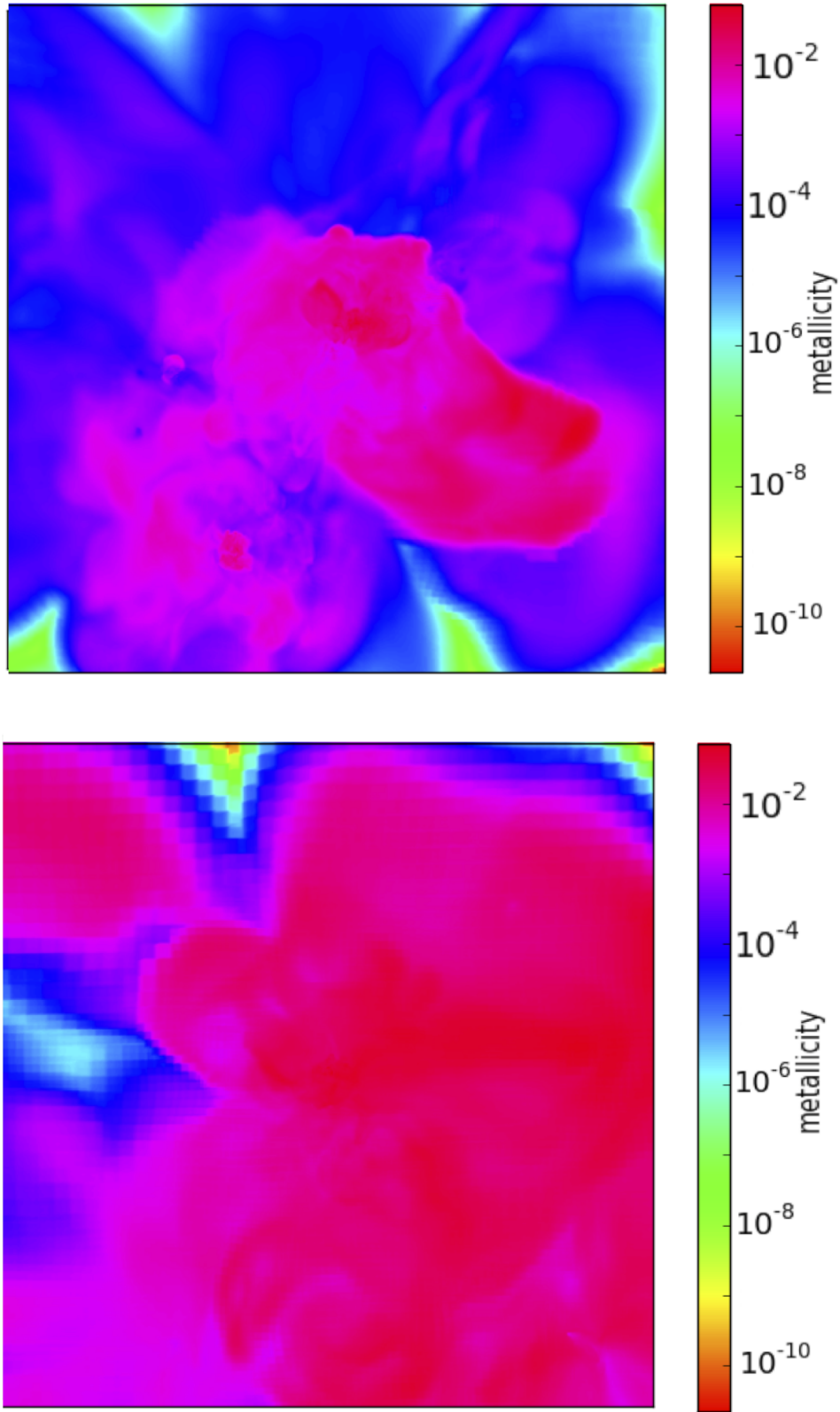


Figure 5.4: Metallicity for a halo with intense star formation (top) and low star formation (bottom) at $z \approx 7$.

Pop III initial mass function (IMF) while still allowing for variability in initial stellar mass, the mass of each primordial star that is formed is randomly selected with equal probability from all masses $30 - 100 M_{\odot}$ for which there are available yields. Each star returns a mass of gas and metals to the interstellar medium (ISM) equal to the selected yields multiplied by a multiplicity factor (taken in this work to be 1.2). Material is further ejected from the halo to the intergalactic medium (IGM) following the model of Tumlinson (2006), with the full details of the halo ejection model given in Section 5.3. Ejection of material from the halo as a result of SNe is not limited to only SN products, but they are ejected preferentially. After a Pop III star is formed, the delay time is determined, and this halo will not be capable of forming chemically enriched stars until that time has passed. It will be possible for it to form stars if it merges with a halo that is already forming chemically enriched stars.

When a chemically enriched halo has passed the delay time following Pop III star formation it begins to form stars at every integration step. 100 such steps are used to traverse each simulation data output (we note that the final result is insensitive to the choice of number of integration steps). At every timestep a mass of stars is formed at a rate proportional to the mass of gas available in the halo, and the reservoir of halo gas is decremented by the mass of stars that is formed. The mass of metals in the ISM is decremented proportionally as well. The stars that are formed have the metallicity of the ISM gas at the time of formation. This is used to determine which metallicity dependent feedback table will be used to return material from the stellar population to the ISM and to eject material to the IGM.

The stellar population in each halo is distributed into 100 age bins to allow for time-dependent chemical and kinetic feedback. As star formation is taken to be continuous in chemically enriched halos, this gives a much better representation of the chemical enrichment history. At each integration timestep, the stellar population first ejects metals and gas to

the ISM. The ejection data is in the units of solar masses of material per solar mass of stars per year. The stellar mass in each age bin returns material according the feedback data for a simple stellar population of that age, multiplied by the integration timestep. This is done for every stellar age bin at each integration timestep, and the stellar mass in each age bin is decremented by the mass of material ejected from it. An identical mechanism is used to determine the number of SNe that occur in the halo during each timestep, again using data dependent on the age and metallicity of the stellar population. The SNe rate data is given in units of SNe per solar mass of stars per year, and the total in the halo is taken to be the sum of the products of the stellar mass in each age bin with the integration timestep. The SNII rates as a function of stellar population age are determined by convolving the IMF mass distribution for stars of mass 12 - 100 M_{\odot} with their associated lifetimes from the Raiteri stellar age formula (see Section 3.3). After material has been ejected from the stellar population to the ISM, the number of SNe that was determined to occur in this timestep is used to eject material from the halo to the IGM. This again preferentially ejects SNe products and follows the prescription outlined in Section 5.3. Once a simulation output has been fully traversed in time, halo mergers are tracked and the ISM gas mass, ISM metal species masses, stellar metal species masses, and age distribution of the stellar mass in each halo is inherited by the child halos in proportion to the fraction of the parent halo mass that the child halo inherited.

5.3 Halo Supernova Ejection

The prescription for ejection of material via supernovae (SNe) from a halo to the intergalactic medium (IGM) is based on several quantities: the number of SNe that occurred; the

mass of gas ejected to the interstellar medium (ISM) by SNe, M_{gas}^{ISM} ; the mass of species gas Z ejected to the ISM by SNe, M_Z^{ISM} ; and the physical parameters of the halo, specifically the mass, M_{halo} , and radius, r_{halo} . The first step of this process is to determine the mass of gas ejected from the halo to the IGM as a result of SNe, M^{IGM} . This is accomplished following Tumlinson (2006), by comparing the energy imparted to the halo gas by all the SNe that went off during the current timestep to the kinetic energy of gas moving at the halo escape velocity, v_{esc} ,

$$E_{SN} = E_{wind} = \frac{1}{2} M_{gas}^{IGM} v_{esc}^2. \quad (5.2)$$

Solving equation 5.2 for M_{gas}^{IGM} and using the definition that the escape velocity is twice the circular orbital velocity allows for the calculation of the M_{gas}^{IGM} in terms of the SNe energetics and the halo physical properties.

$$M_{gas}^{IGM} = \frac{2E_{SN}}{v_{esc}^2} \quad (5.3)$$

$$v_{circ} = v_{esc}/2 = \sqrt{\frac{GM_{halo}}{r_{halo}}} \quad (5.4)$$

Combining these two equations gives M_{gas}^{IGM} as,

$$M_{gas}^{IGM} = \frac{E_{SN} r_{halo}}{2GM_{halo}}. \quad (5.5)$$

The energy imparted to the wind by SNe can be parameterized as,

$$E_{SN} = N_{SN} \epsilon_{SN} E_{51} \quad (5.6)$$

where N_{SN} is the number of SNe that occurred during the current timestep, ϵ_{SN} is the

efficiency with which the SNe energy is converted to the kinetic energy of the gas (taken to be 0.15%, as in Tumlinson (2006)), and E_{51} is the energy of a single SN in units of 10^{51} erg. Using this parameterization along with equation 5.5 allows for the calculation of M_{gas}^{IGM} in M_{\odot} as,

$$M_{gas}^{IGM} = 3.896 \times 10^8 \frac{N_{SN} \epsilon_{SN} E_{51} r_{halo}}{GM_{halo}}, \quad (5.7)$$

where M_{halo} is in units of M_{\odot} , r_{halo} is in Mpc, and G is in cgs units.

Once M_{gas}^{IGM} has been determined, the mass of species Z in the ISM, M_Z , is updated in one of two ways depending on whether M_{gas}^{IGM} is greater or less than M_{gas}^{ISM} . If M_{gas}^{IGM} is greater than M_{gas}^{ISM} , all material ejected by the SNe is taken to have been ejected from the halo. The difference of M_{gas}^{IGM} and M_{gas}^{ISM} is then compared to the total gas mass in the halo, M_{gas} . The gas and metals in the halo are taken to be perfectly mixed, and M_Z is reduced in proportion to the ratio of ejected gas not originated in SNe to the total mass of gas in the halo. Specifically, M_Z is multiplied by the factor,

$$M_Z^{updated} = M_Z \left(1 - \frac{M_{gas}^{IGM} - M_{gas}^{ISM}}{M_{gas}} \right). \quad (5.8)$$

In the second case, if M_{gas}^{IGM} is less than M_{gas}^{ISM} , it is assumed that some of the SNe products remain in the halo and enrich the ISM. M_Z^{ISM} is decremented in proportion to $M_{gas}^{IGM}/M_{gas}^{ISM}$ with the reduced M_Z^{ISM} added to M_Z . Specifically, M_Z is increased by,

$$M_Z^{updated} = M_Z + M_Z^{ISM} \left(1 - \frac{M_{gas}^{IGM}}{M_{gas}^{ISM}} \right). \quad (5.9)$$

5.3.1 Results

Figure 5.5 shows the distribution of stellar mass in $[\text{Fe}/\text{H}]-[\text{Mg}/\text{Fe}]$ space for a fiducial model using a Salpeter IMF and $\text{SFE}= 0.04$. The image shows the distribution at $z = 10$. The central panel shows the distribution of stellar mass in all of the halos in the simulation at $z = 10$. The coloring reflects the amount of stellar mass, normalized to the total stellar mass in the simulation, at that combination of $[\text{Fe}/\text{H}]$ and $[\text{Mg}/\text{Fe}]$. White regions are regions in $[\text{Fe}/\text{H}]-[\text{Mg}/\text{Fe}]$ space where there is no stellar mass. Gray regions have a very small fraction of the total stellar mass, with red having and increasingly large fraction of the mass, up to the most common combination of $[\text{Fe}/\text{H}]$ and $[\text{Mg}/\text{Fe}]$, colored in blue. The top and right panels are histograms of the distribution of stellar mass in $[\text{Fe}/\text{H}]$ and $[\text{Mg}/\text{Fe}]$, respectively, and share their axes and range with the associated axis of the central panel. Taking the right panel as an example, it can be seen that the most common value of $[\text{Mg}/\text{Fe}]$ is 0.3, while the top panel shows that the most common value of $[\text{Fe}/\text{H}]$ is -2.5. The most common value in the central panel does not necessarily line up with the most common value in either of the histograms. The peak of the central panel will show the most common combination of both $[\text{Mg}/\text{Fe}]$ and $[\text{Fe}/\text{H}]$ values, while the histogram will show the most common individual value. Figure 5.6 is of the same style as Figure 5.5, but the y-axis is now $[\text{C}/\text{Fe}]$ rather than $[\text{Mg}/\text{Fe}]$. This figure shows the fiducial model: a Salpeter IMF and $\text{SFE}= 0.04$. The $[\text{Fe}/\text{H}]$ distribution between the two figures is by definition identical.

A more robust assessment of the model data is to compare the metallicity distribution of the stellar population in the simulation with observational data. The Sloan Extension for Galactic Understanding and Exploration (SEGUE) dataset provides spectra of 119,000 stars in the Milky Way halo. A subset of approximately 17,000 nearby stars from SEGUE

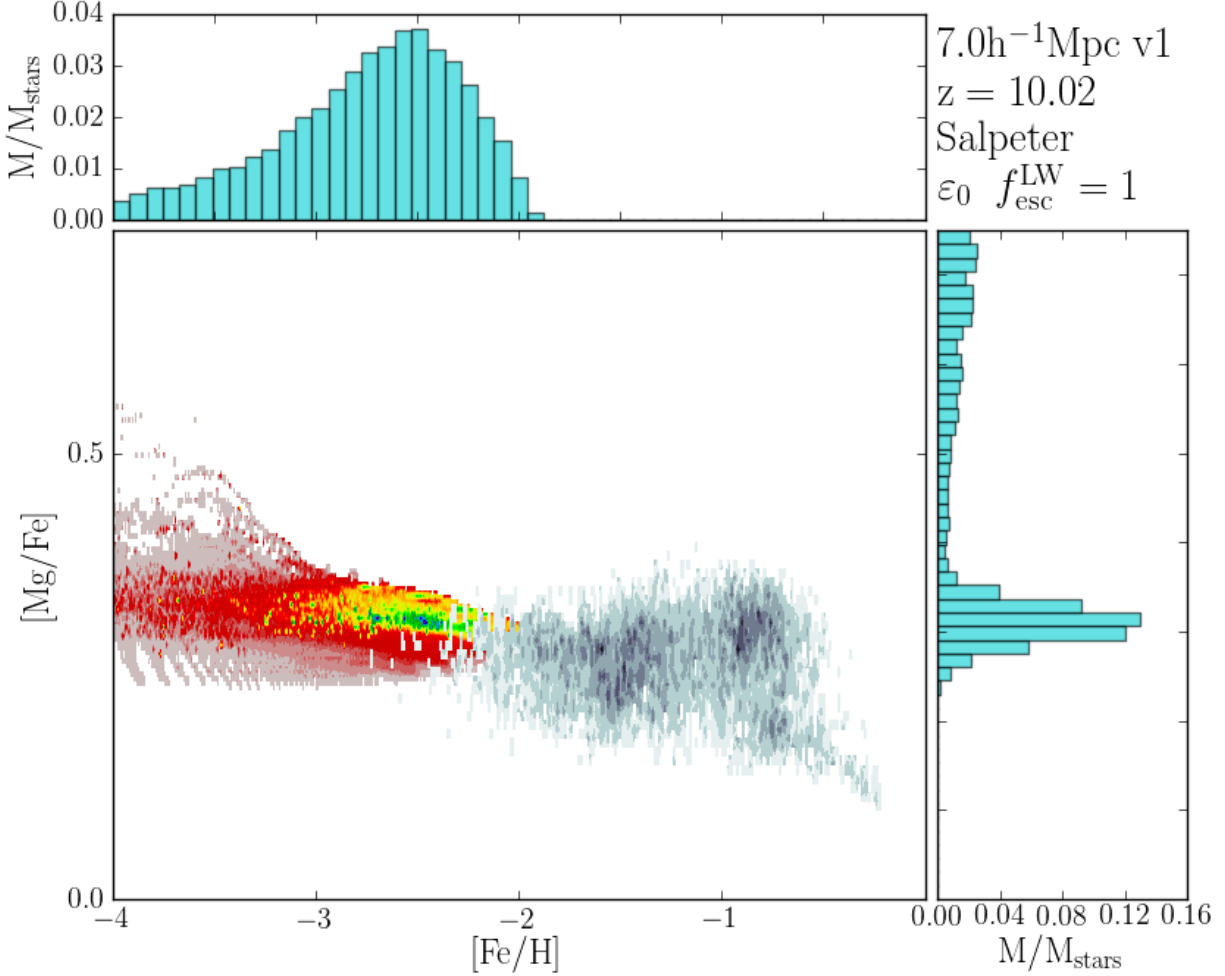


Figure 5.5: $[\text{Fe}/\text{H}]$ - $[\text{Mg}/\text{Fe}]$ distribution of the entire stellar mass in all halos in the simulation at $z = 10$ for the fiducial model with a Salpeter IMF and $\text{SFE}=0.04$. The central panels are the mass-weighted stellar distribution in $[\text{Fe}/\text{H}]$ - $[\text{Mg}/\text{Fe}]$ space. White regions have no stellar mass, gray regions have a small, non-zero amount of stellar mass, while red has more stellar mass, and blue is the most common combination of $[\text{Fe}/\text{H}]$ and $[\text{Mg}/\text{Fe}]$. The top and right panels show the distribution of the stellar mass in only $[\text{Fe}/\text{H}]$ (top) and $[\text{Mg}/\text{Fe}]$ (right), and share the same axes values as the central panel. SEGUE data is plotted in grayscale contours over the model prediction.

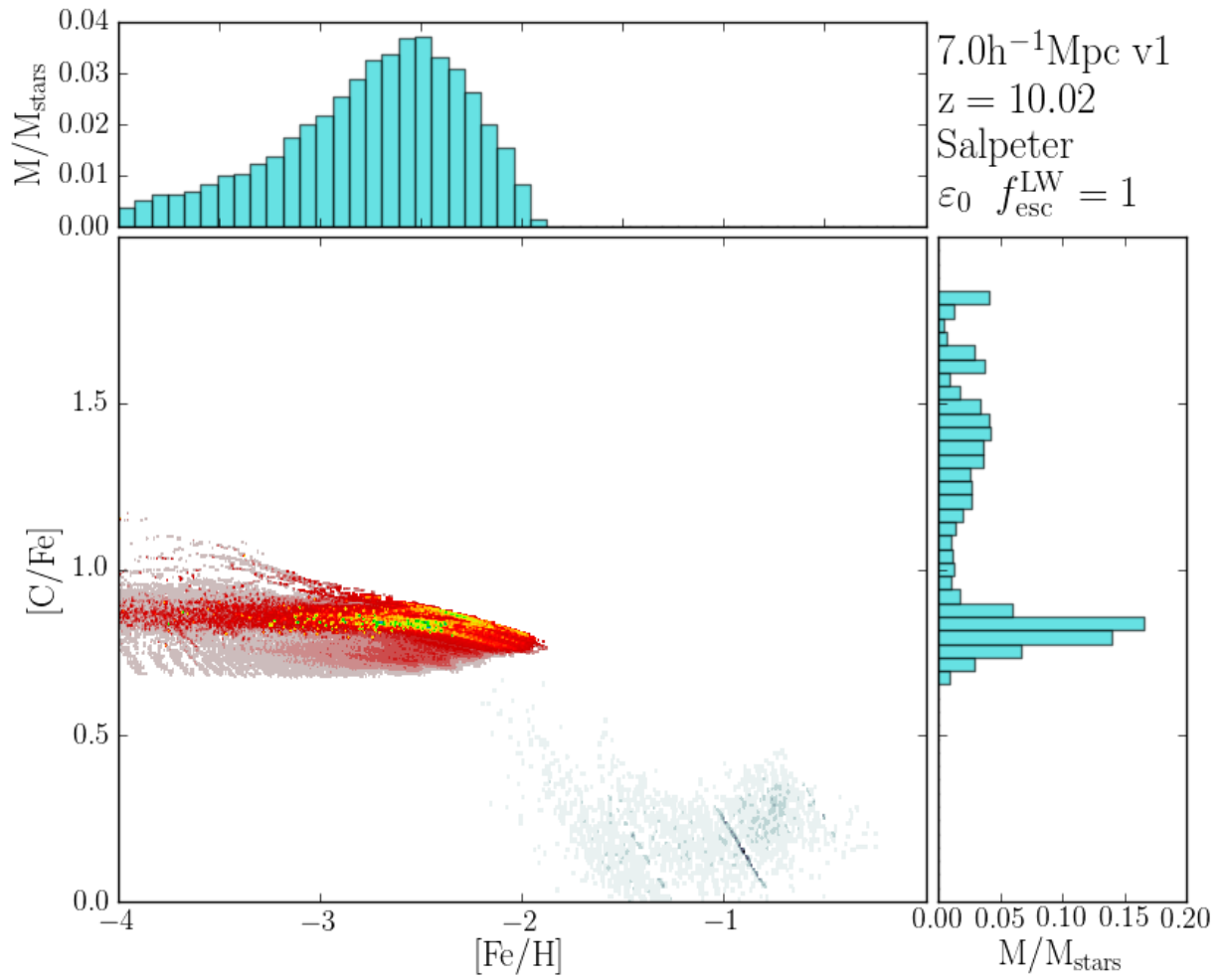


Figure 5.6: Same as figure 5.5 but for $[\text{C}/\text{Fe}]$.

that includes values of $[\text{Fe}/\text{H}]$, $[\text{C}/\text{Fe}]$, and $[\text{Mg}/\text{Fe}]$ was used as a comparison the metallicity distribution produced by each variation of parameters in this model. The SEGUE subset was binned in $[\text{Fe}/\text{H}]-[\text{C}/\text{Fe}]$ space and $[\text{Fe}/\text{H}]-[\text{Mg}/\text{Fe}]$ space to allow for comparison to the mass-weighted metallicity distributions in the same parameter spaces utilized in this model. It bears noting that while mass-weighting was used in analyzing the model data as a crude proxy for luminosity, it was not possible to use an identical method with the SEGUE subset. The binning for the SEGUE data was done only by the number of stars in each metallicity bin. This comparison is thus inexact, but can be used to approximately evaluate the quality of the metallicity distribution produced by the model by examining the relative overlap of the two populations.

Comparing the predictions of the model with the SEGUE dataset reflects the various degrees of success of this model in reproducing the observed metallicity distribution of nearby Milky Way stars. Figure 5.5 shows a region of the stellar $[\text{Fe}/\text{H}]-[\text{Mg}/\text{Fe}]$ distribution from the fiducial model with the subset of SEGUE stars overplotted in grayscale contours. While there is disagreement between the predicted and observed distributions, there is significant overlap. It is also worth noting that the SEGUE dataset in question does not go to as low of a metallicity as the Wise et al. (2012) simulations probe. Additionally, $[\text{Mg}/\text{Fe}]$ is converging to the right value at higher metallicity. This is likely due to our choice of yields and may change as improved models become available. Variations of the model with different IMFs better reproduced the observed metallicity distribution, and are discussed later in this section.

Figure 5.6 is similar to Figure 5.5, but with the y-axis showing $[\text{C}/\text{Fe}]$ rather than $[\text{Mg}/\text{Fe}]$. The agreement between the model prediction and the $[\text{C}/\text{Fe}]$ distribution is significantly worse than the agreement with $[\text{Mg}/\text{Fe}]$. This would indicate that there is some problem

with the way in which we are handling the enrichment of carbon in our models. This could result from the parameters in the model being insufficient to model the physical processes that are important to carbon enrichment, incorrect carbon yields from stellar evolution models, or incorrect models for SNIa delay time or frequency. Model predictions for the $[\text{Mg}/\text{Fe}]$ and $[\text{Fe}/\text{H}]$ distributions can be made to agree well with the SEGUE observations through variation of the IMF and SFE, but $[\text{C}/\text{Fe}]$ cannot be well fit by any combination of parameters in this model. The disagreement of only $[\text{C}/\text{Fe}]$ suggests that the predicted carbon yields are likely the source of this discrepancy.

Using a Kroupa IMF rather than a Salpeter IMF has the effect of broadening the $[\text{Mg}/\text{Fe}]$ distribution and shifting the average to slightly lower values, from $[\text{Mg}/\text{Fe}]=0.303$ with a Salpeter IMF to $[\text{Mg}/\text{Fe}]=0.292$ with a Kroupa IMF. There is very little change in the $[\text{Fe}/\text{H}]$ distribution between these two IMFs. The Kroupa IMF is enhanced in comparison to the Salpeter IMF in the range of approximately $0.3 M_{\odot} < M < 7 M_{\odot}$ (see Figure 3.1), providing more stars that are capable for forming a white dwarf (WD) in the timescales of star formation in this simulation. In addition to being able to produce a WD, the single-degenerate model used in this work also requires an evolved companion, which necessitates an intermediate mass star. The double dependence on intermediate mass stars suggests that the SNIa rate will be very sensitive to the frequency of intermediate mass stars. Figure 5.7 supports this, as the shift in $[\text{Mg}/\text{Fe}]$ to lower values with a Kroupa IMF as compared to a Salpeter IMF can be attributed to enhanced iron production from SNIa.

A Chabrier IMF produces an even greater departure from the $[\text{Fe}/\text{H}]-[\text{Mg}/\text{Fe}]$ distribution of the Salpeter IMF, extending to lower values of $[\text{Mg}/\text{Fe}]$ and higher $[\text{Fe}/\text{H}]$. The decrease in $[\text{Mg}/\text{Fe}]$ can again be attributed to increased SNIa rates arising from an excess of intermediate mass stars over both the Salpeter and Kroupa IMFs. That the decrease is

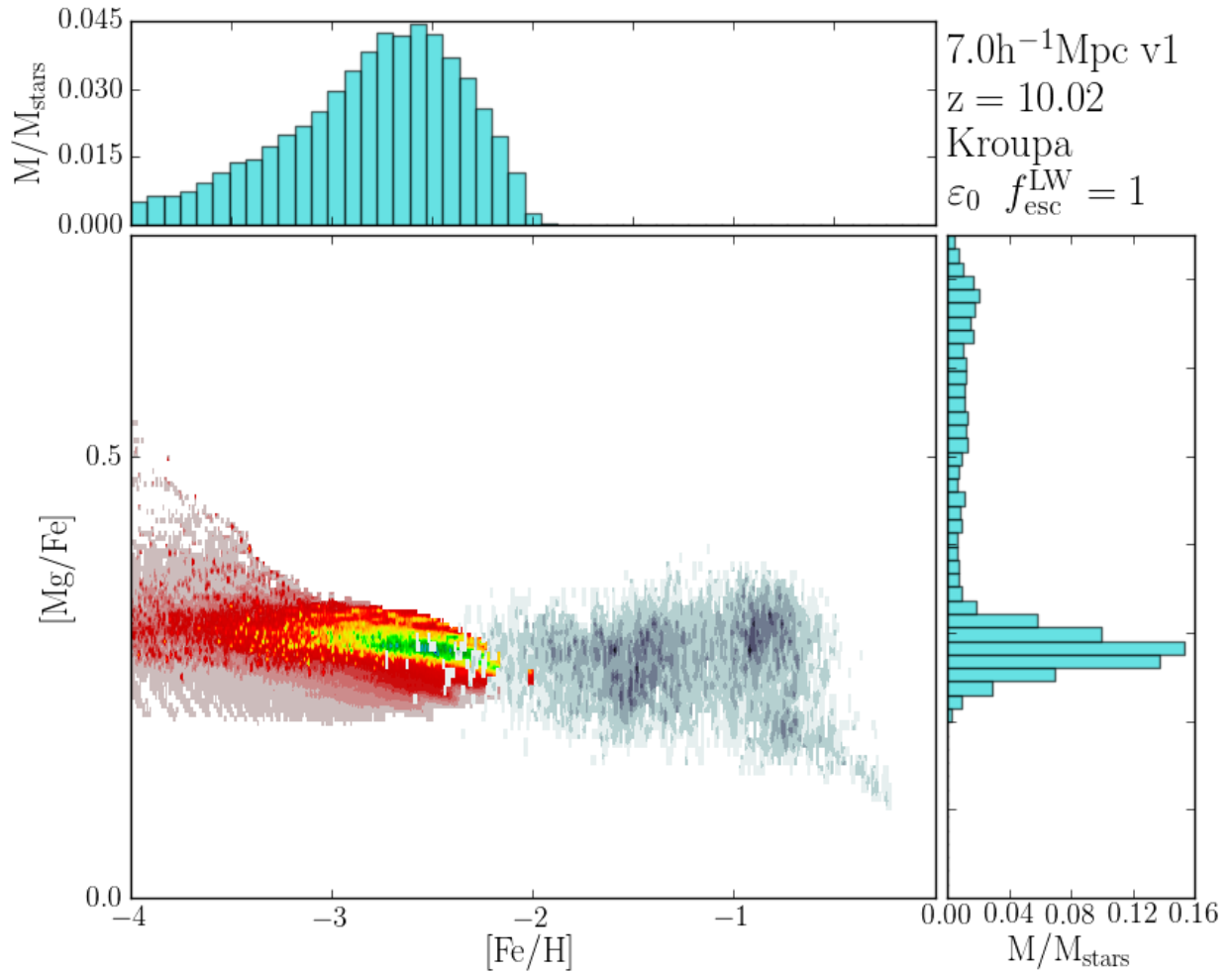


Figure 5.7: $[\text{Fe}/\text{H}]-[\text{Mg}/\text{Fe}]$ distribution of the entire stellar mass in all halos in the simulation at $z = 10$ for the fiducial model with a Kroupa IMF and $\text{SFE}=0.04$. The central panels are the mass-weighted stellar distribution in $[\text{Fe}/\text{H}]-[\text{Mg}/\text{Fe}]$ space. White regions have no stellar mass, gray regions have a small, non-zero amount of stellar mass, while red has more stellar mass, and blue is the most common combination of $[\text{Fe}/\text{H}]$ and $[\text{Mg}/\text{Fe}]$. The top and right panels show the distribution of the stellar mass in only $[\text{Fe}/\text{H}]$ (top) and $[\text{Mg}/\text{Fe}]$ (right), and share the same axes values as the central panel. SEGUE data is plotted in grayscale contours over the model prediction.

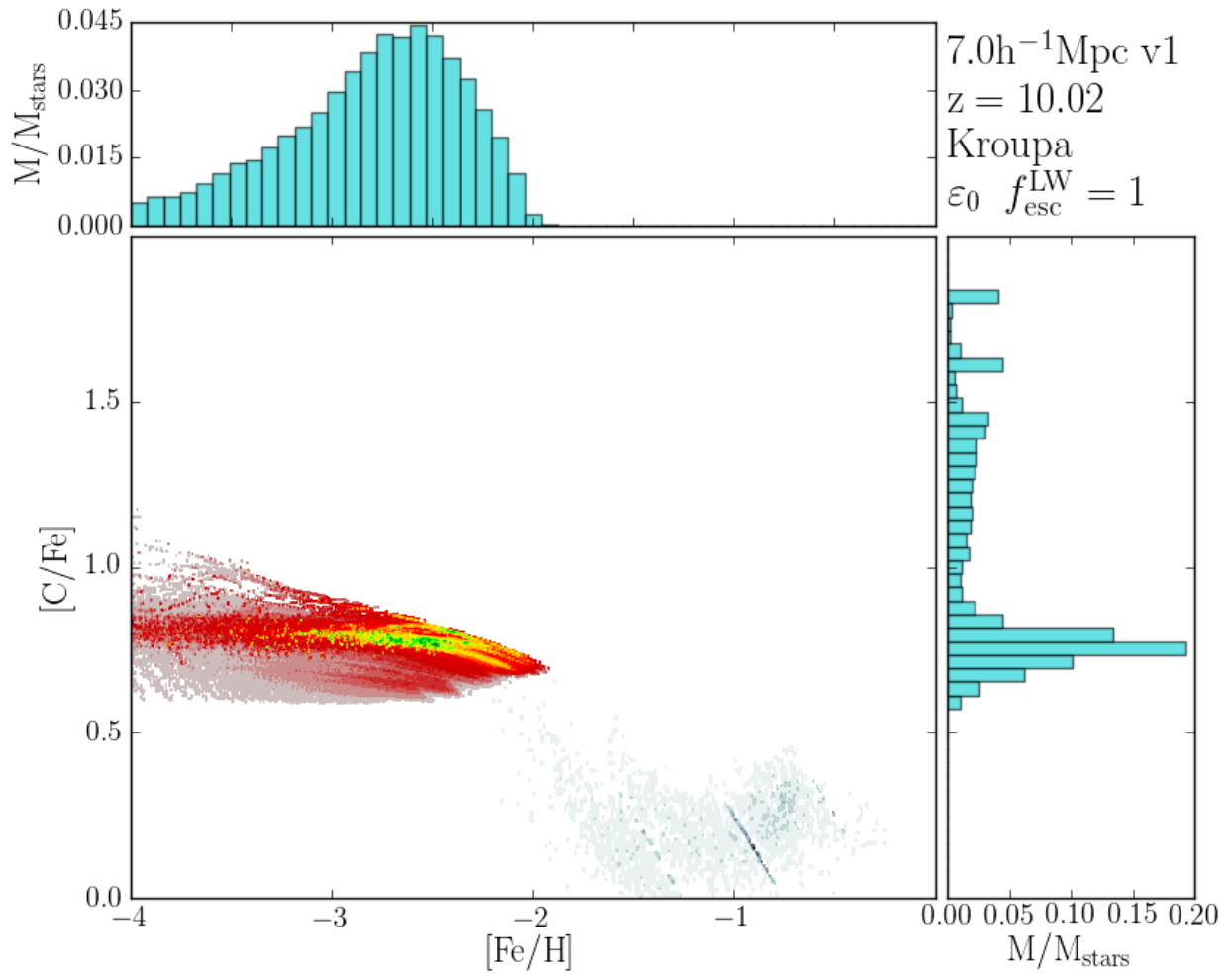


Figure 5.8: Same as figure 5.7 but for $[\text{C}/\text{Fe}]$.

more pronounced than with a Kroupa IMF reflects that the enhancement of intermediate mass stars is greater for a Chabrier IMF than for a Kroupa IMF. Iron is produced in greater relative quantities to both magnesium as hydrogen due to the contribution of SNII from stars with a zero age main sequence (ZAMS) mass greater than $8 M_{\odot}$. The Chabrier IMF has a far higher fraction of high mass stars than either the Salpeter or Kroupa IMFs, and as iron is strongly produced in SNII, increases in the fraction of the stellar population above $8 M_{\odot}$ will significantly boost iron production relative to both hydrogen and alpha elements. The abrupt downturn in the $[\text{Fe}/\text{H}]-[\text{Mg}/\text{Fe}]$ distribution at $[\text{Fe}/\text{H}] = -1.25$ and $[\text{Mg}/\text{Fe}] = 0.3$, shown in Figure 5.9, is in striking qualitative agreement with the similar observed extension to lower $[\text{Mg}/\text{Fe}]$ and higher $[\text{Fe}/\text{H}]$ that is seen in the SEGUE sample.

The $[\text{Fe}/\text{H}]-[\text{C}/\text{Fe}]$ distribution with a Kroupa IMF is shown in Figure 5.8. The Kroupa $[\text{Fe}/\text{H}]$ distribution is similarly unchanged in comparison to a Salpeter IMF as in the $[\text{Fe}/\text{H}]-[\text{Mg}/\text{Fe}]$ distribution. The similarity in high mass stars between the two IMFs results in similar SNII rates, and in turn production of similar ratios of iron to hydrogen. Carbon is produced in intermediate mass AGB stars. As such, the increase in intermediate mass stars in the Kroupa IMF increases the fraction of stars that go through an AGB phase, and in turn increases carbon production relative to iron. This is responsible for pushing the $[\text{C}/\text{Fe}]$ distribution with a Kroupa IMF to higher values than those found with a Salpeter IMF.

The $[\text{Fe}/\text{H}]-[\text{C}/\text{Fe}]$ distribution that arises with a Chabrier IMF is again elevated in $[\text{Fe}/\text{H}]$ compared to the Salpeter IMF as a result of the increased fraction of massive stars that end their lives in SNII, yielding significant iron enrichment. The intermediate mass stars with a Chabrier IMF are boosted in comparison to the Salpeter IMF, which in an identical manner to the Kroupa IMF leads to an increase in $[\text{C}/\text{Fe}]$ over the $[\text{C}/\text{Fe}]$ produced with a Salpeter IMF due to the increased relative yield of carbon from AGB stars. Figures 5.9 and 5.10 show

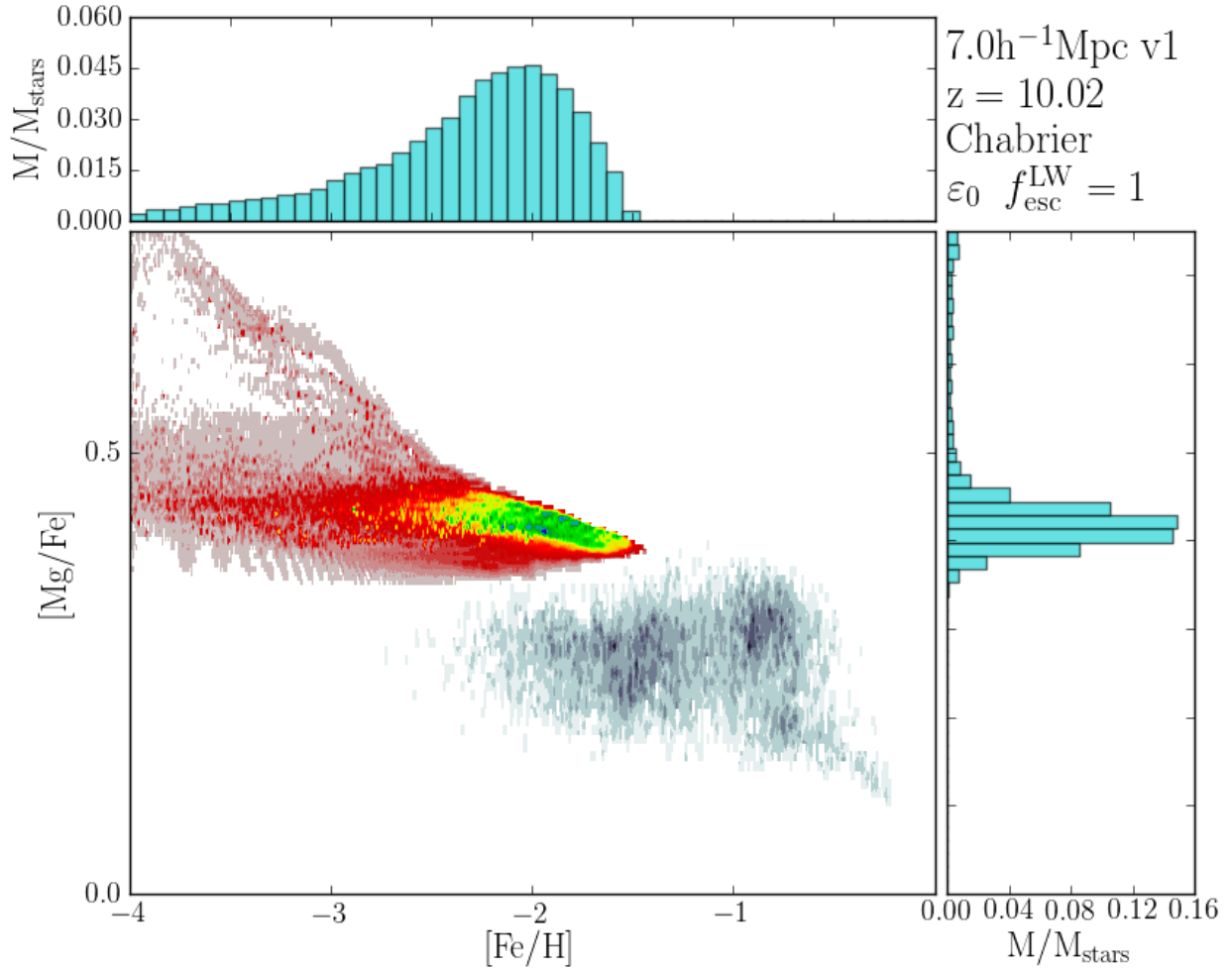


Figure 5.9: Same as figure 5.5 but for a Chabrier IMF.

the impact on the $[\text{Fe}/\text{H}]-[\text{Mg}/\text{Fe}]$ and $[\text{Fe}/\text{H}]-[\text{C}/\text{Fe}]$ distributions.

Comparison between the model predictions of the stellar $[\text{Fe}/\text{H}]$ distribution and that observed by SEGUE shows that the Kroupa IMF more accurately reproduces the observed abundance data than does a Chabrier IMF. While neither IMF perfectly reproduces the SEGUE data, the Kroupa IMF is peaked at a higher $[\text{Fe}/\text{H}]$, has a higher mass-weighted average value, and extends to higher $[\text{Fe}/\text{H}]$ than the Kroupa IMF. All three of these attributes would independently improve the agreement between the Chabrier IMF generated $[\text{Fe}/\text{H}]$ distribution and the SEGUE observations, and taken in aggregate makes a com-

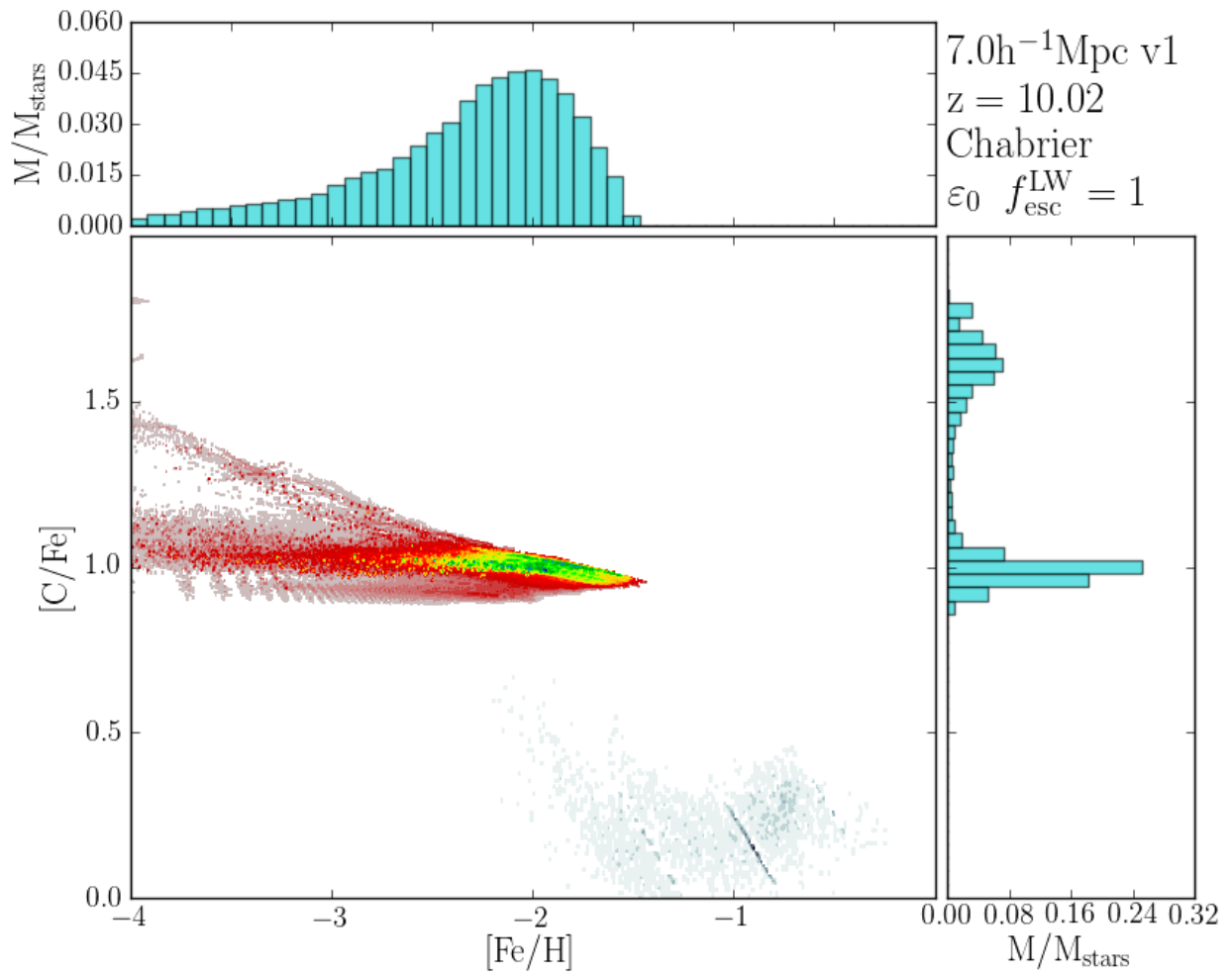


Figure 5.10: Same as figure 5.9 but for $[\text{C}/\text{Fe}]$

elling case that the Kroupa IMF more accurately reproduces observed $[\text{Fe}/\text{H}]$ data than does the Kroupa IMF. No set of parameters in the model were able to reproduce the observed $[\text{C}/\text{Fe}]$ distribution, which we hypothesize is due to issues relating to the modeling of carbon generation in stellar evolution environments.

Chapter 6

Summary and Future Work

High-resolution simulations involving formation of the first stars, their HII regions, the evolution of their resulting supernova remnants, and the mixing of the metal-enriched gas into the next generation of halos, are required to understand the chemical and dynamical evolution of our Galaxy and its progenitors. This drives the fundamental requirements of our chemical evolution model; namely, the ability to model the nucleosynthetic and energetic feedback from stellar populations of highly variable metallicity, and possibly variable IMF, over a period of up to 14 billion years. With this in mind, in this dissertation we have provided a critical examination of available nucleosynthetic stellar yields, and suggest a minimal set of input parameters to model Galactic Chemical Evolution.

In Chapter , we defined the terms necessary for a comparison of published yield sets, and discussed the assumptions, input physics and resulting trends for several stellar environments; AGB stars, Type II and Type Ia supernovae, and hypernovae. In Chapter , we provided the necessary details to incorporate yield sets in models of GCE. In Chapter , we demonstrated a direct application of this model in a simplified form, following the chemical history of isolated stellar populations.

We have suggested tracing the enrichment history of 12 elements (C, N, O, Mg, Ca, Ti, Fe, Co, Zn, Ba, Eu, Sr), which represent the important mechanisms for ISM cooling and nucleosynthetic processes readily observable in nearby stars, and examined the yield

calculations that include these elements.

Differences in the treatment of convection, mixing, mass loss, nuclear-reaction rates, and choice of explosion energy and mass cut lead to SNII yields which can differ by as much as an order of magnitude (see Figure 2.2), but are typically within a factor of two.

Yields of AGB stars are widely available, but the models creating these yields include very different approximations to important input physics. Modern calculations are time consuming, with the inclusion of HBB and partial mixing zones, modeling of numerous thermal pulses, and treatment of the TDU and ^{13}C pocket. Treatment of mass loss can include metallicity effects, and is tuned to match observed luminosity functions. The tumultuous regime of the sAGB stars is most clearly shown by the lack of nucleosynthetic models published. We have only shown one study which takes on this substantial computational expenditure in Section 2.4.3.

While numerous yield sets exist, they tend to omit neutron-capture elements. Uncertain nuclear-reaction rates and the unknown site of the r-process mean we must look to observational abundance patterns to estimate yields.

The yields of SNIa are similar across many studies. The key to a valid model for GCE is to incorporate delay times for the release of metals and energy. We have adopted an analytic model, one commonly used to determine delay times, and that also fits observed SNIa rates.

The ubiquity of the IMF in our Galaxy has been called into question, based on recent observations of metal-poor stars and newly-formed stars. The suggestion of a time varying or environment specific IMF could be explored within the parameters of GCE, however, we have shown that yield differences from one study to another may wash out our ability to explore implications of such variability.

Chapter describes the implementation of a basic chemical evolution model that allows

for comparison against a subset of SEGUE data which includes $[\text{Fe}/\text{H}]$, $[\text{C}/\text{Fe}]$, and $[\text{Mg}/\text{Fe}]$ values (Carollo et al., 2012). Good agreement is found between the $[\text{Fe}/\text{H}]$ - $[\text{Mg}/\text{Fe}]$ distributions of the model and observations. There is poor agreement between the $[\text{C}/\text{Fe}]$ values of the model and observations, though there is qualitative agreement. Presently available observational data do not enable the degeneracy between carbon production in AGB stars and SNIa to be broken, though there is hope to be able to do this in the future. Additionally, the uncertainties in Carbon stellar nucleosynthetic yields currently inhibit our ability to fit observations.

Despite pitfalls in stellar nucleosynthetic yield coverage, we have developed a feedback model for use in cosmological hydrodynamical simulations. Future work will utilize Enzo, an adaptive mesh refinement code (O’Shea et al., 2004; Norman et al., 2007), to trace the chemodynamical history of Milky Way type halos from the onset of star formation to the present day with a range of formation histories. The aim of which will be to understand how merger histories and environments affect the nucleosynthesis of progenitor galaxies and the Milky Way disk itself. Furthermore, we plan to compare the semi-analytic models to a wider range of observational datasets including APOGEE (Allende Prieto et al., 2008), PAndAs (McConnachie et al., 2009), and observations of the Milky Way and Andromeda dwarfs.

Chapter 7

IMF and Yield Variations

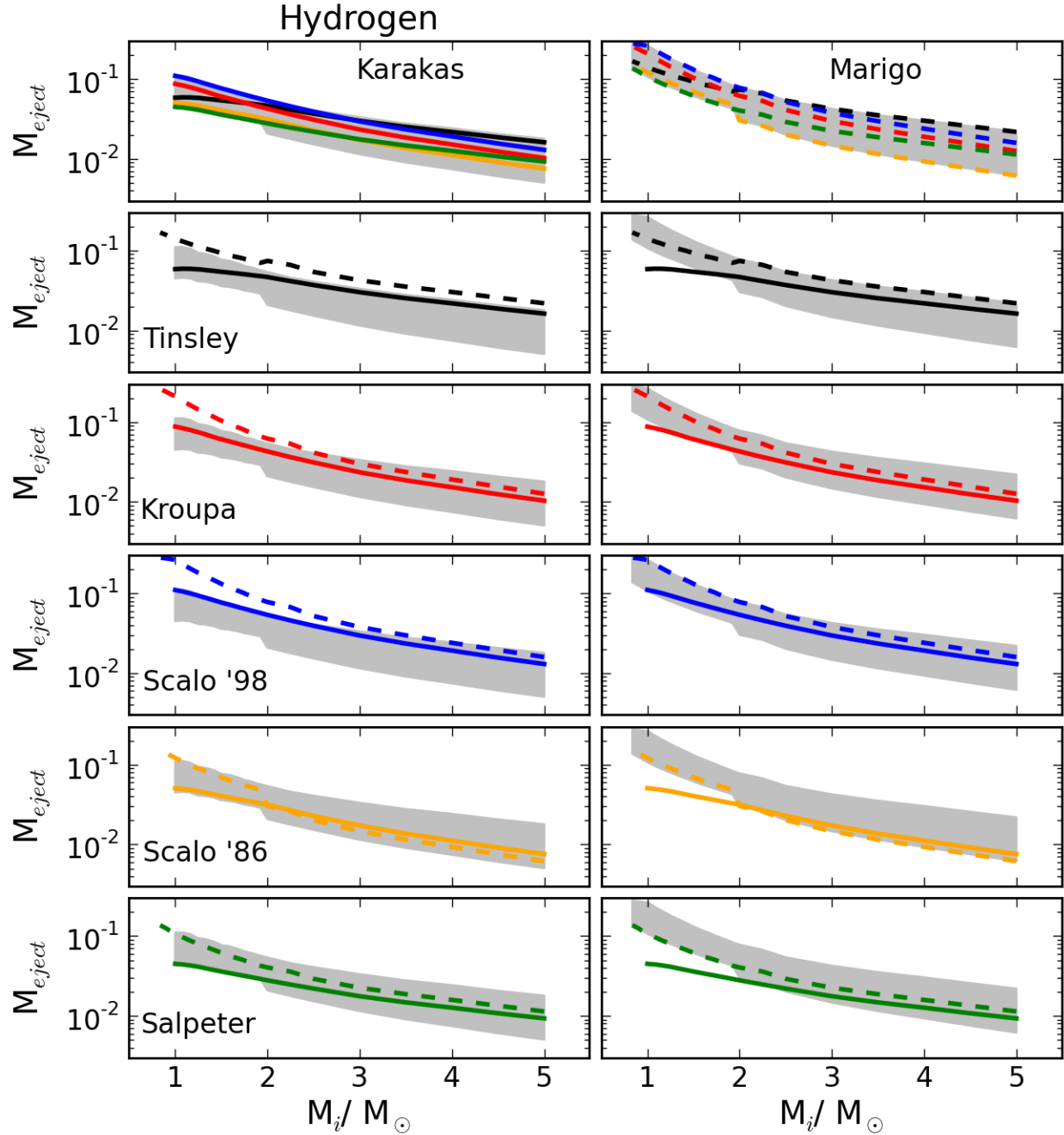


Figure 7.1: Each frame shows a side-by-side comparison of IMF-weighted Hydrogen yields from two sources, Karakas (2010) and Marigo (2001). First two panels show one yield source for all 5 choices of IMF. Rows 2 through 6 show each yield source overplotted for a single IMF choice. The shaded region denotes the spread of ejected mass of the corresponding yield source due to IMF choice. If the spread due to IMF choice is larger than the spread between two yield sources, we may be able to discern between IMFs from observations. If the yield source spread is larger than the IMF spread, yield uncertainties make it impossible to extract the formation environment from observations. See Section 3.2 for the functional forms.

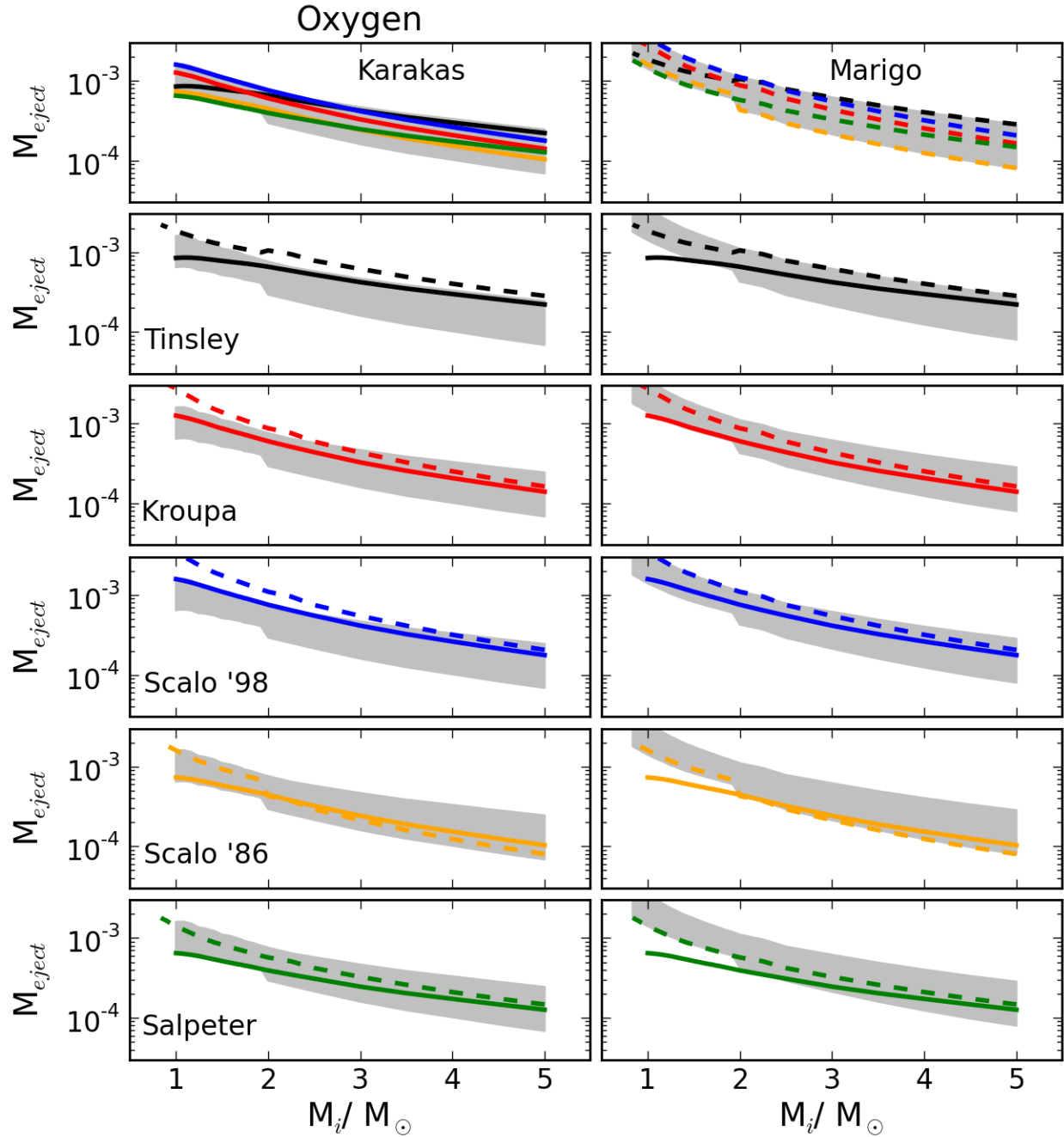


Figure 7.2: Each frame shows a side-by-side comparison of IMF-weighted Oxygen yields from two sources, Karakas (2010) and Marigo (2001). First two panels show one yield source for all 5 choices of IMF. Rows 2 through 6 show each yield source overplotted for a single IMF choice. The shaded region denotes the spread of ejected mass of the corresponding yield source due to IMF choice. If the spread due to IMF choice is larger than the spread between two yield sources, we may be able to discern between IMFs from observations. If the yield source spread is larger than the IMF spread, yield uncertainties make it impossible to extract the formation environment from observations. See Section 3.2 for the functional forms.

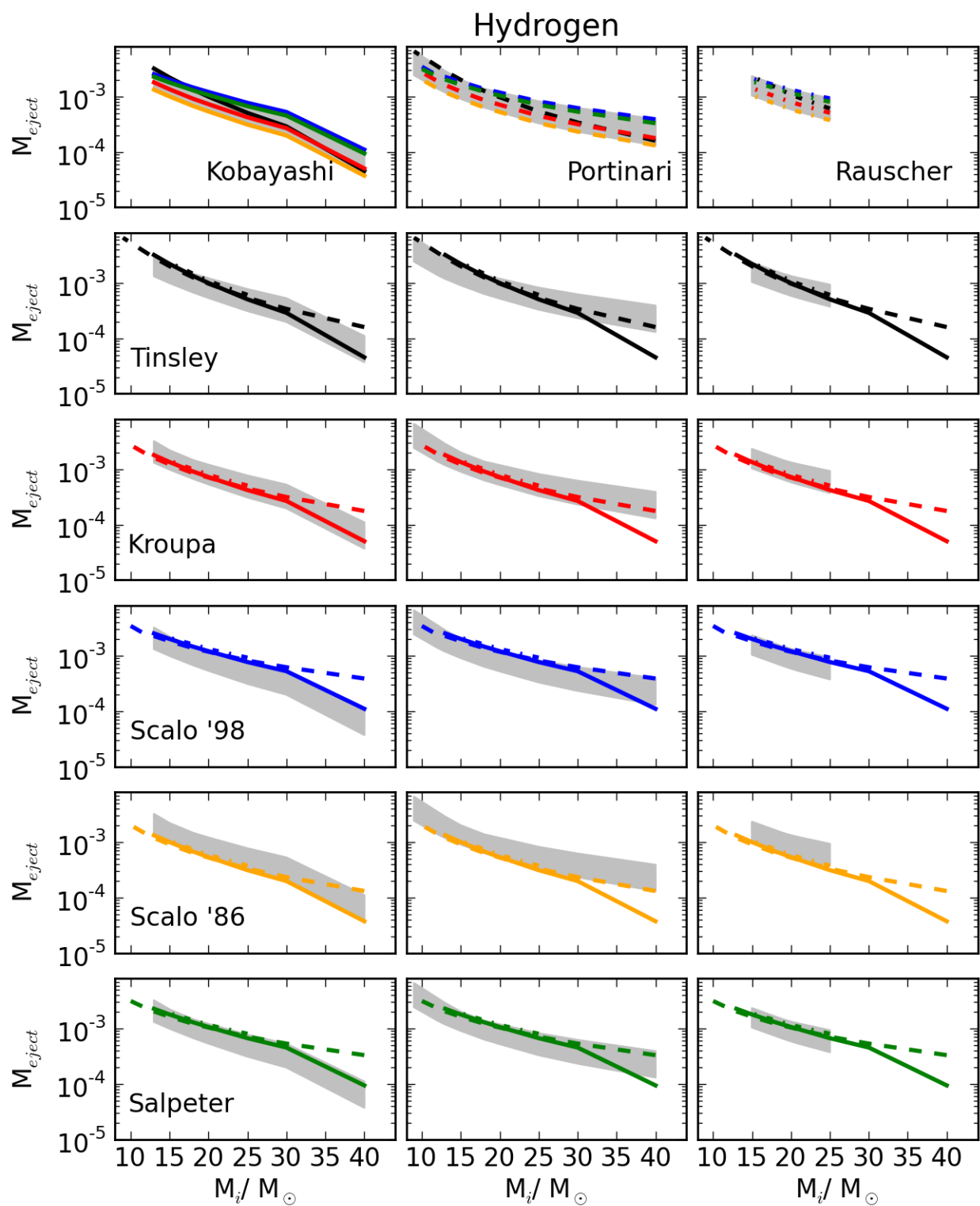


Figure 7.3: Same as Figure 7.1, but for the SNII Hydrogen yields of Kobayashi et al. (2006), Portinari et al. (1998), and Rauscher et al. (2002)

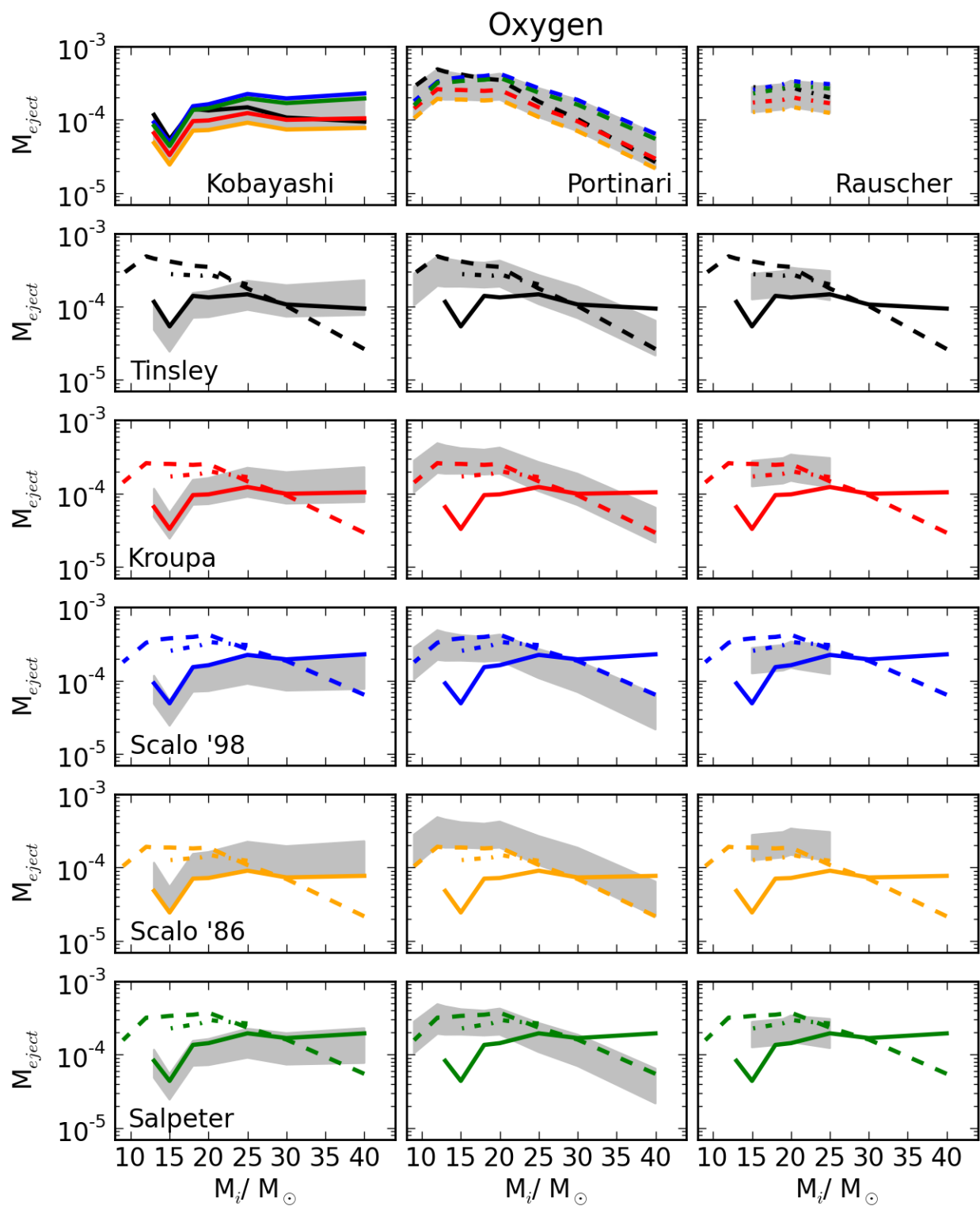


Figure 7.4: Same as Figure 7.1, but for the SNII Oxygen yields of Kobayashi et al. (2006), Portinari et al. (1998), and Rauscher et al. (2002)

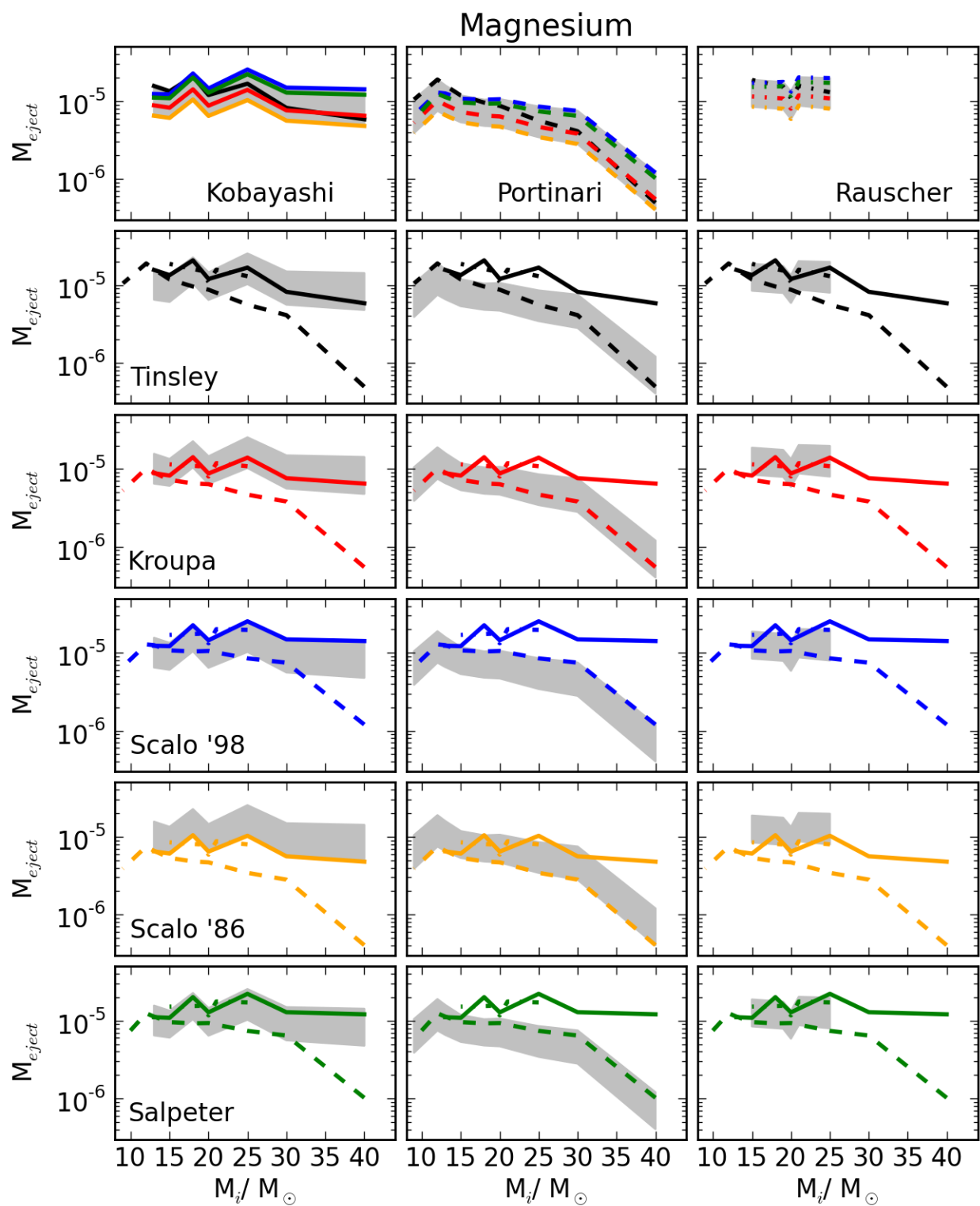


Figure 7.5: Same as Figure 7.1, but for the SNII Magnesium yields of Kobayashi et al. (2006), Portinari et al. (1998), and Rauscher et al. (2002)

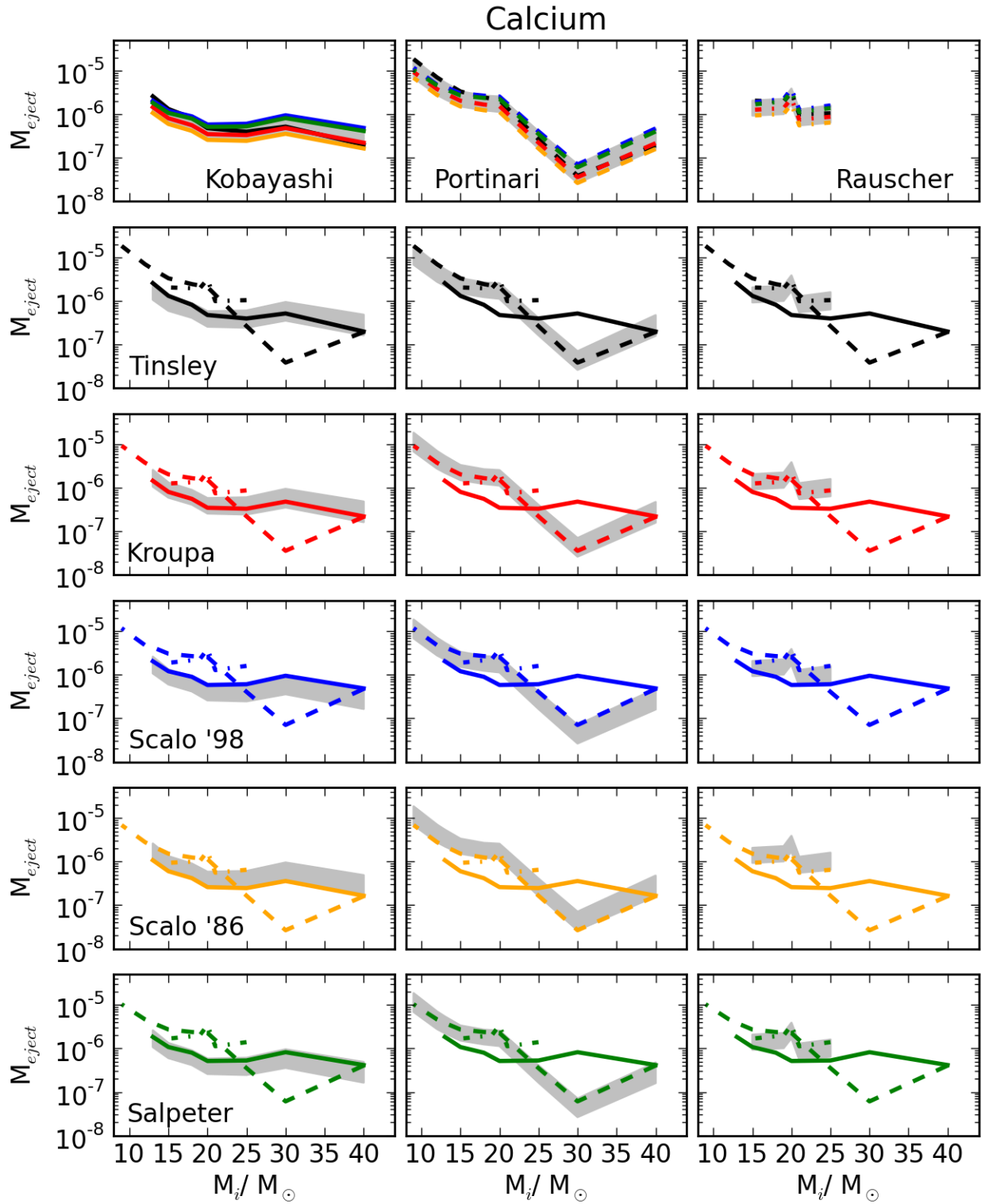


Figure 7.6: Same as Figure 7.1, but for the SNII Calcium yields of Kobayashi et al. (2006), Portinari et al. (1998), and Rauscher et al. (2002)

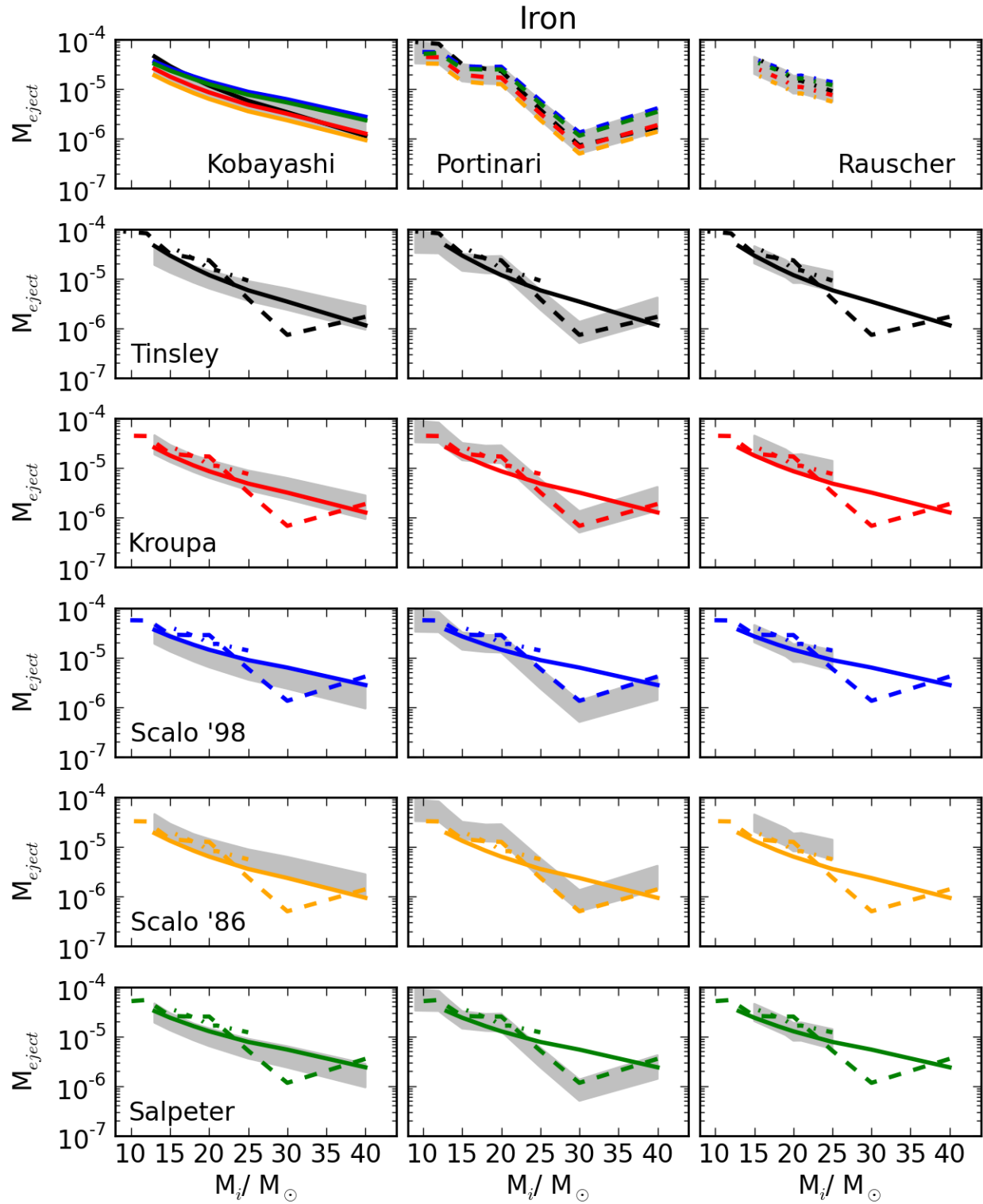


Figure 7.7: Same as Figure 7.1, but for the SNII Iron yields of Kobayashi et al. (2006), Portinari et al. (1998), and Rauscher et al. (2002)

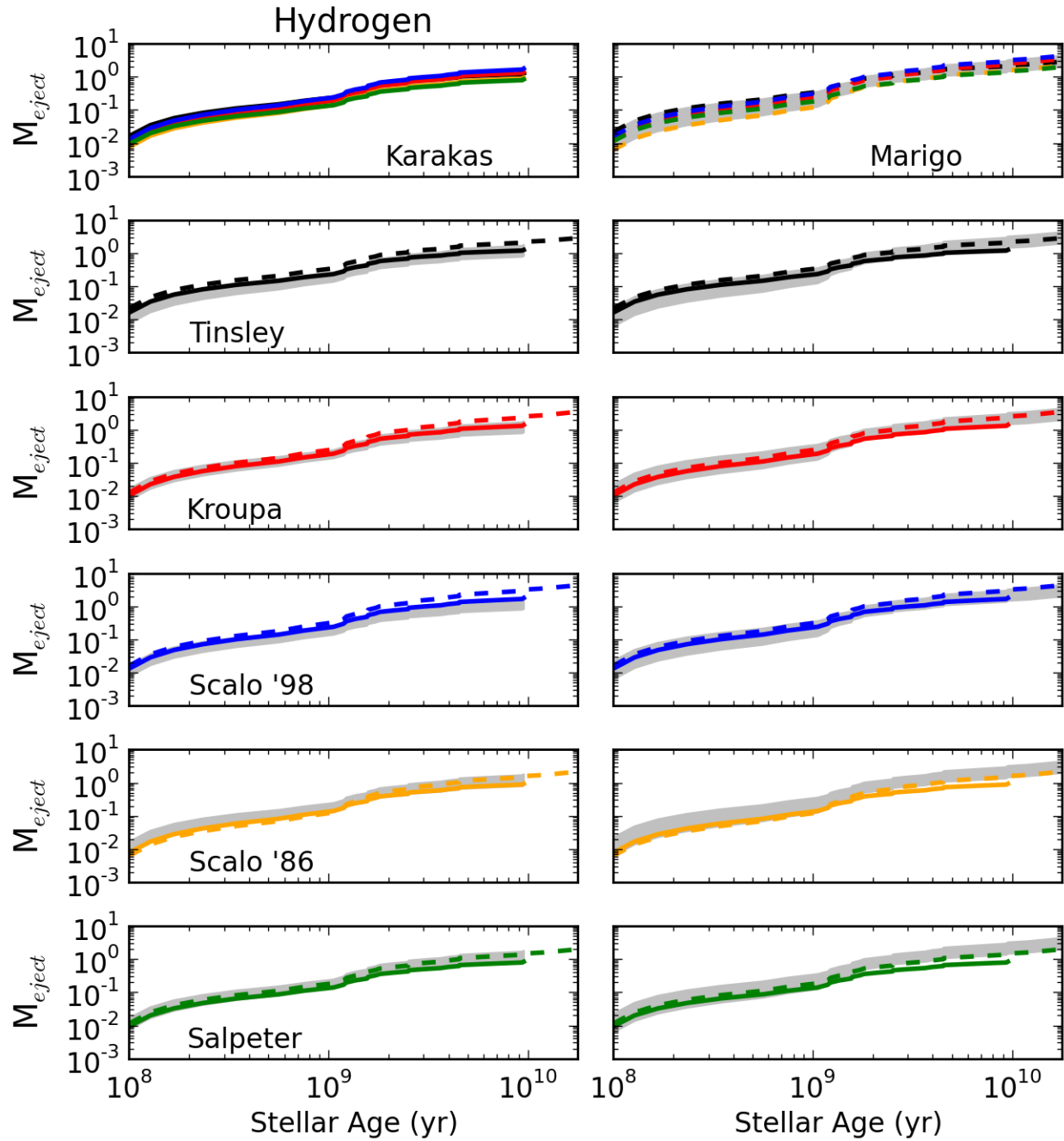


Figure 7.8: Each frame shows a side-by-side comparison of integrated history from Hydrogen yields from two sources, Karakas (2010) and Marigo (2001). First two panels show one yield source for all 5 choices of IMF. Rows 2 through 6 show each yield source overplotted for a single IMF choice. See Section 3.2 for the functional forms.

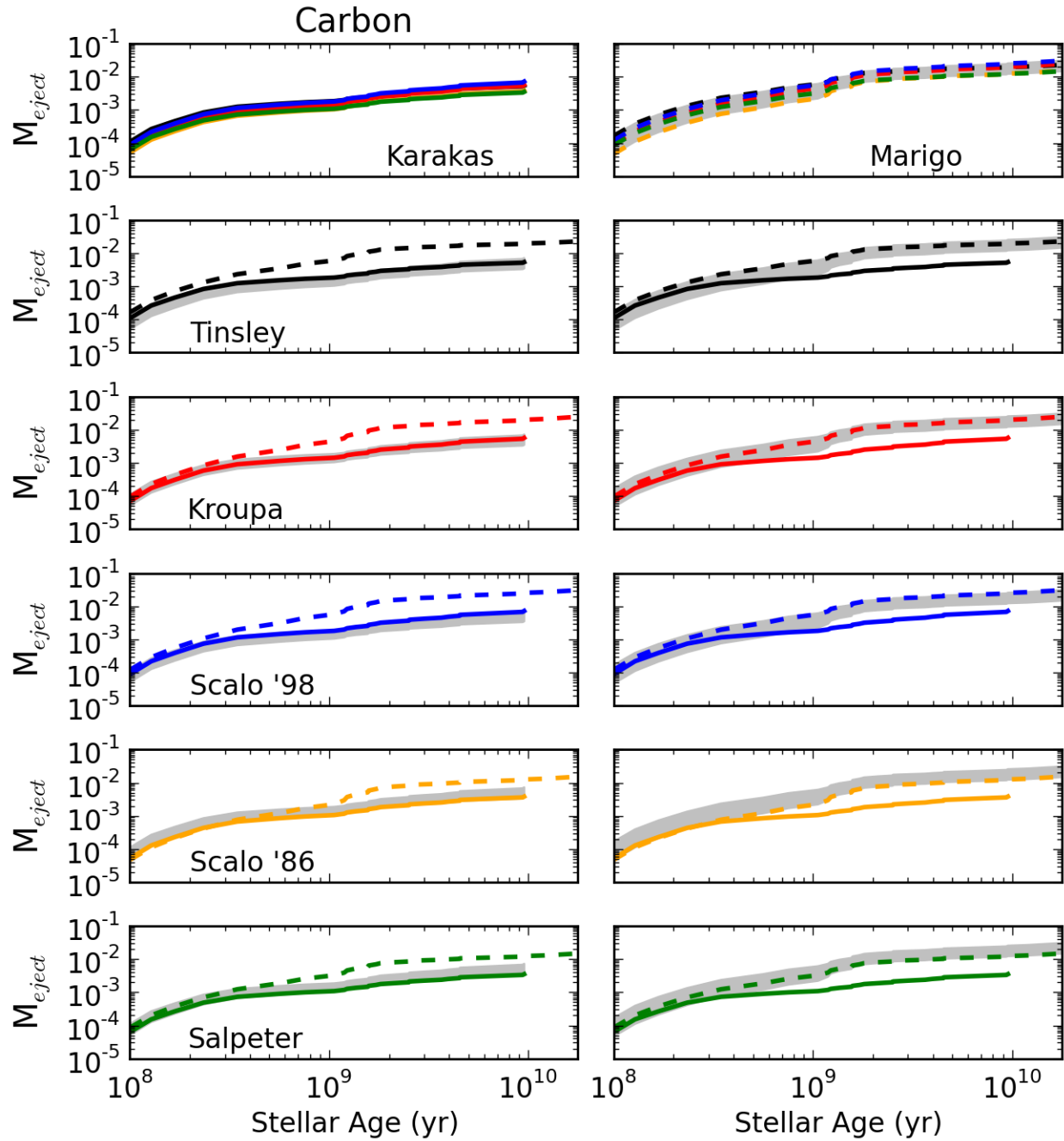


Figure 7.9: Each frame shows a side-by-side comparison of integrated history from Carbon yields from two sources, Karakas (2010) and Marigo (2001). First two panels show one yield source for all 5 choices of IMF. Rows 2 through 6 show each yield source overplotted for a single IMF choice. See Section 3.2 for the functional forms.

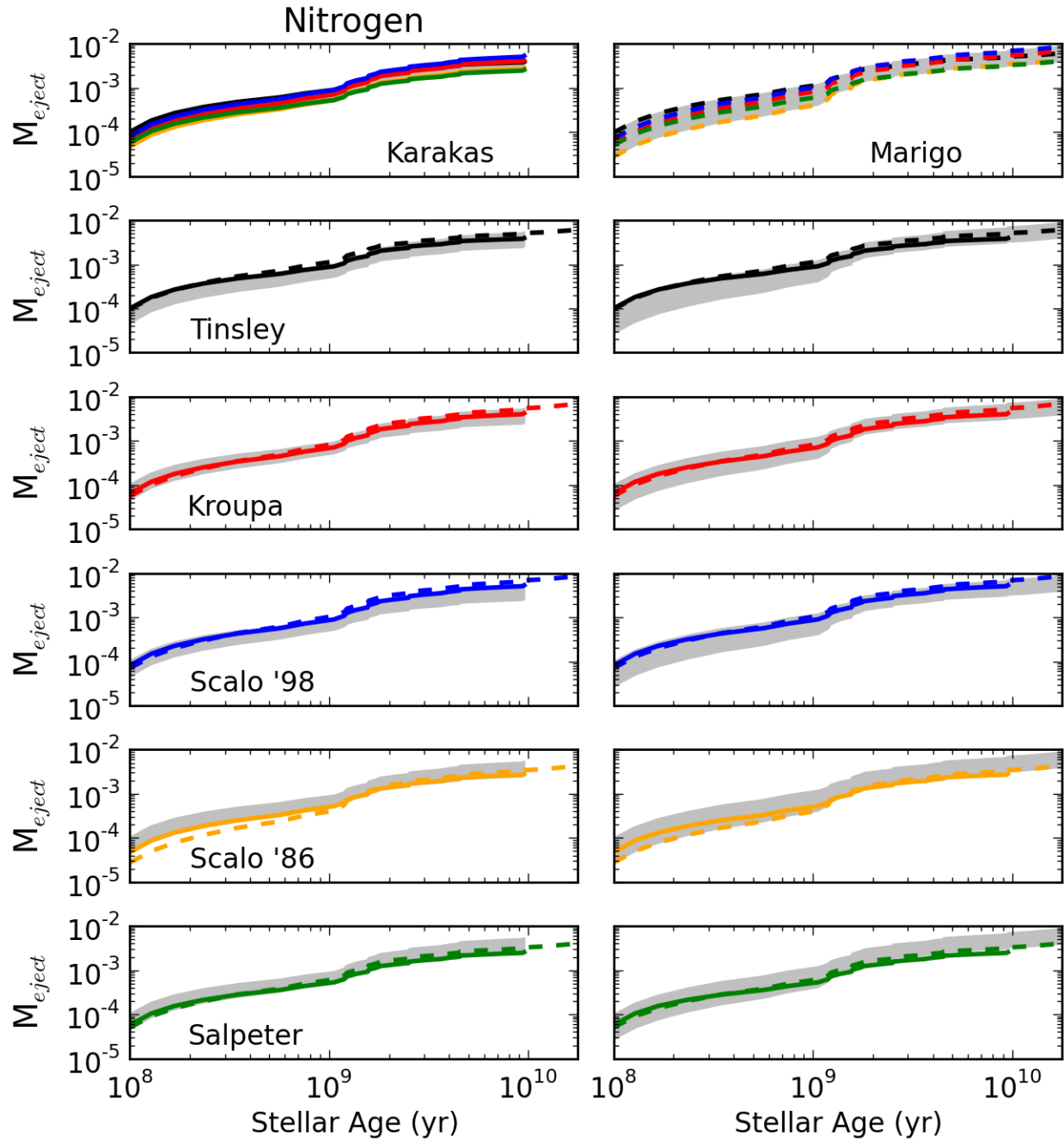


Figure 7.10: Each frame shows a side-by-side comparison of integrated history from Nitrogen yields from two sources, Karakas (2010) and Marigo (2001). First two panels show one yield source for all 5 choices of IMF. Rows 2 through 6 show each yield source overplotted for a single IMF choice. See Section 3.2 for the functional forms.

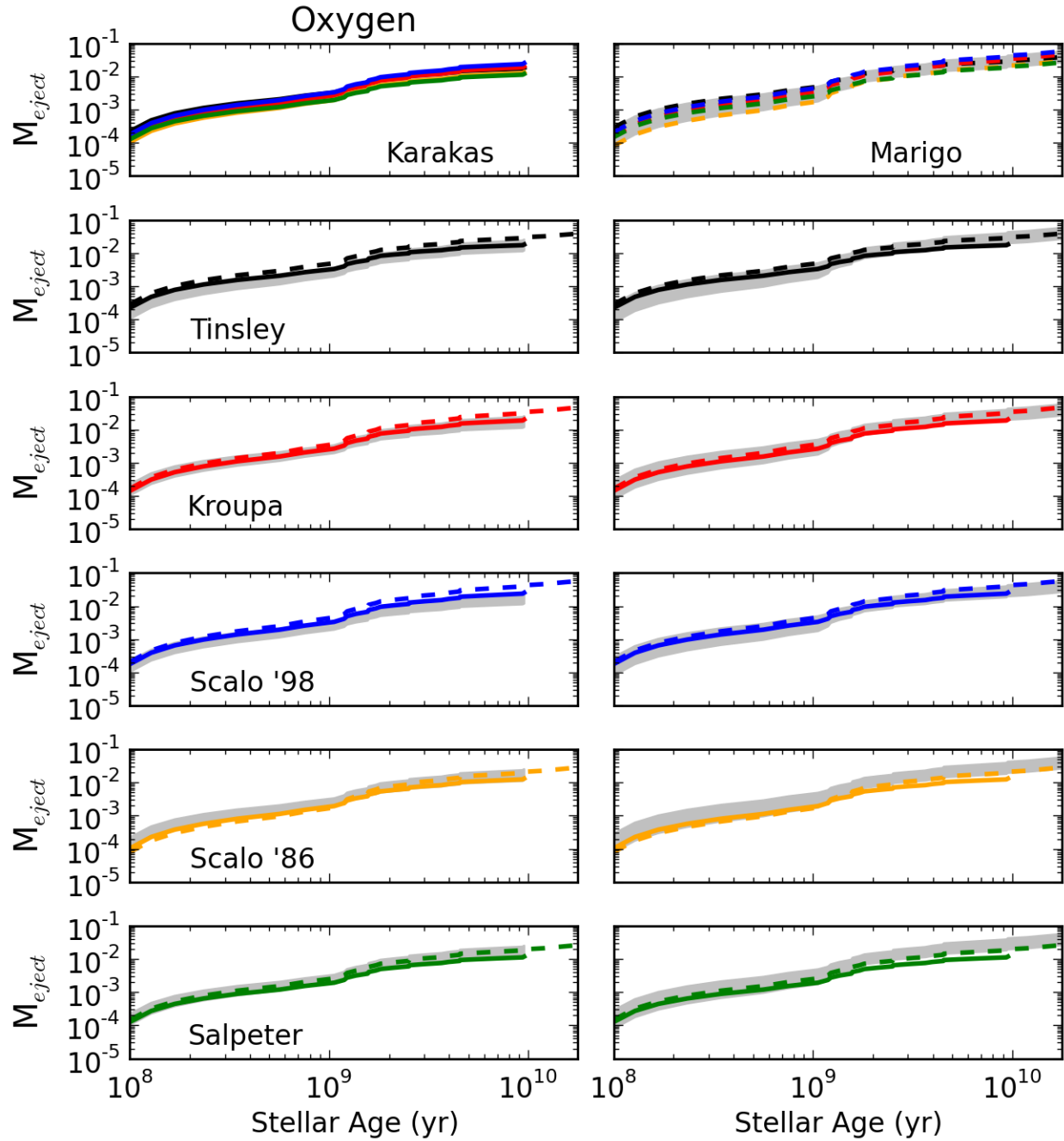


Figure 7.11: Each frame shows a side-by-side comparison of integrated history from Oxygen yields from two sources, Karakas (2010) and Marigo (2001). First two panels show one yield source for all 5 choices of IMF. Rows 2 through 6 show each yield source overplotted for a single IMF choice. See Section 3.2 for the functional forms.

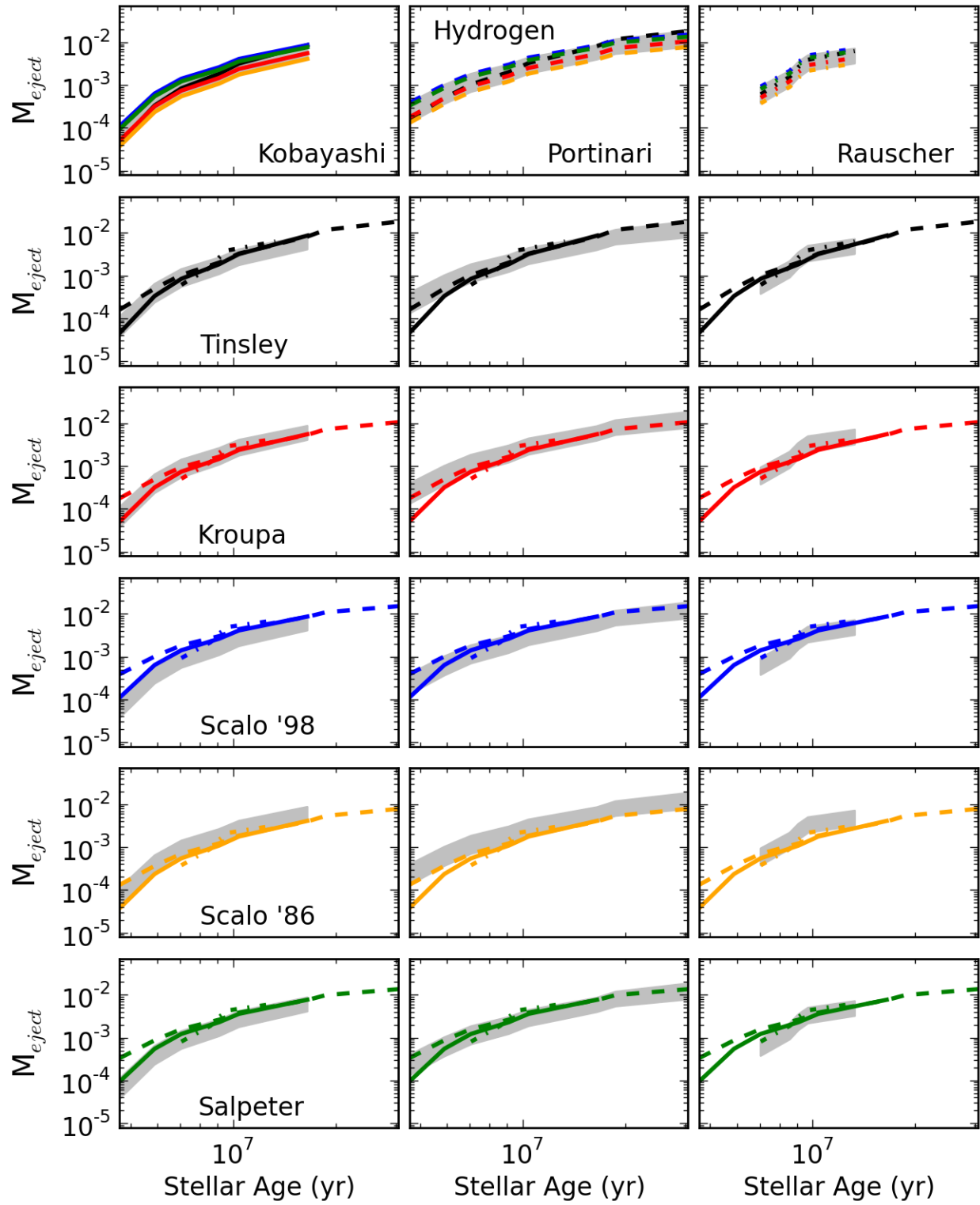


Figure 7.12: Same as Figure 7.8, but for the SNII Hydrogen yields of Kobayashi et al. (2006), Portinari et al. (1998), and Rauscher et al. (2002)

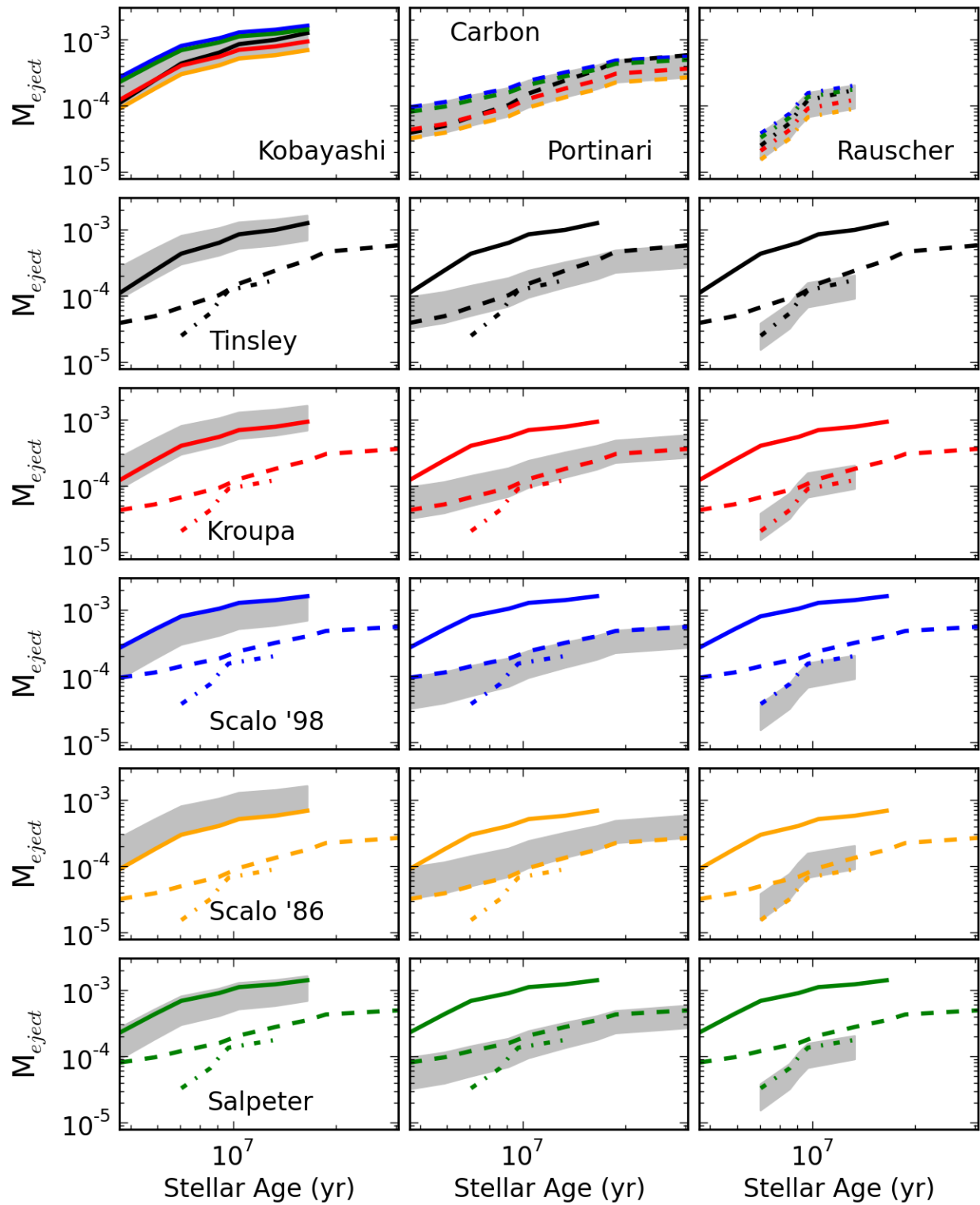


Figure 7.13: Same as Figure 7.1, but for the SNII Carbon yields of Kobayashi et al. (2006), Portinari et al. (1998), and Rauscher et al. (2002)

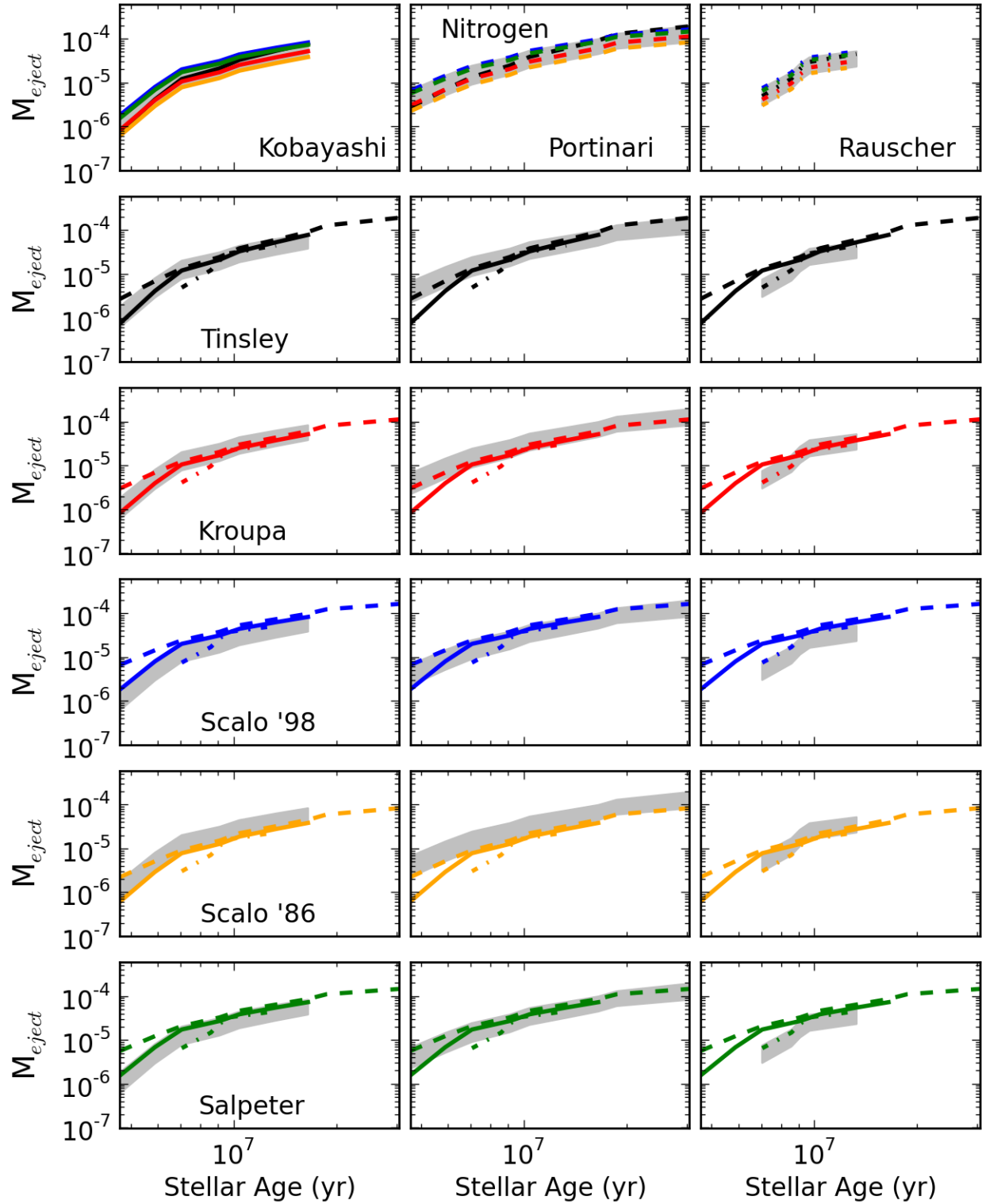


Figure 7.14: Same as Figure 7.1, but for the SNII Nitrogen yields of Kobayashi et al. (2006)

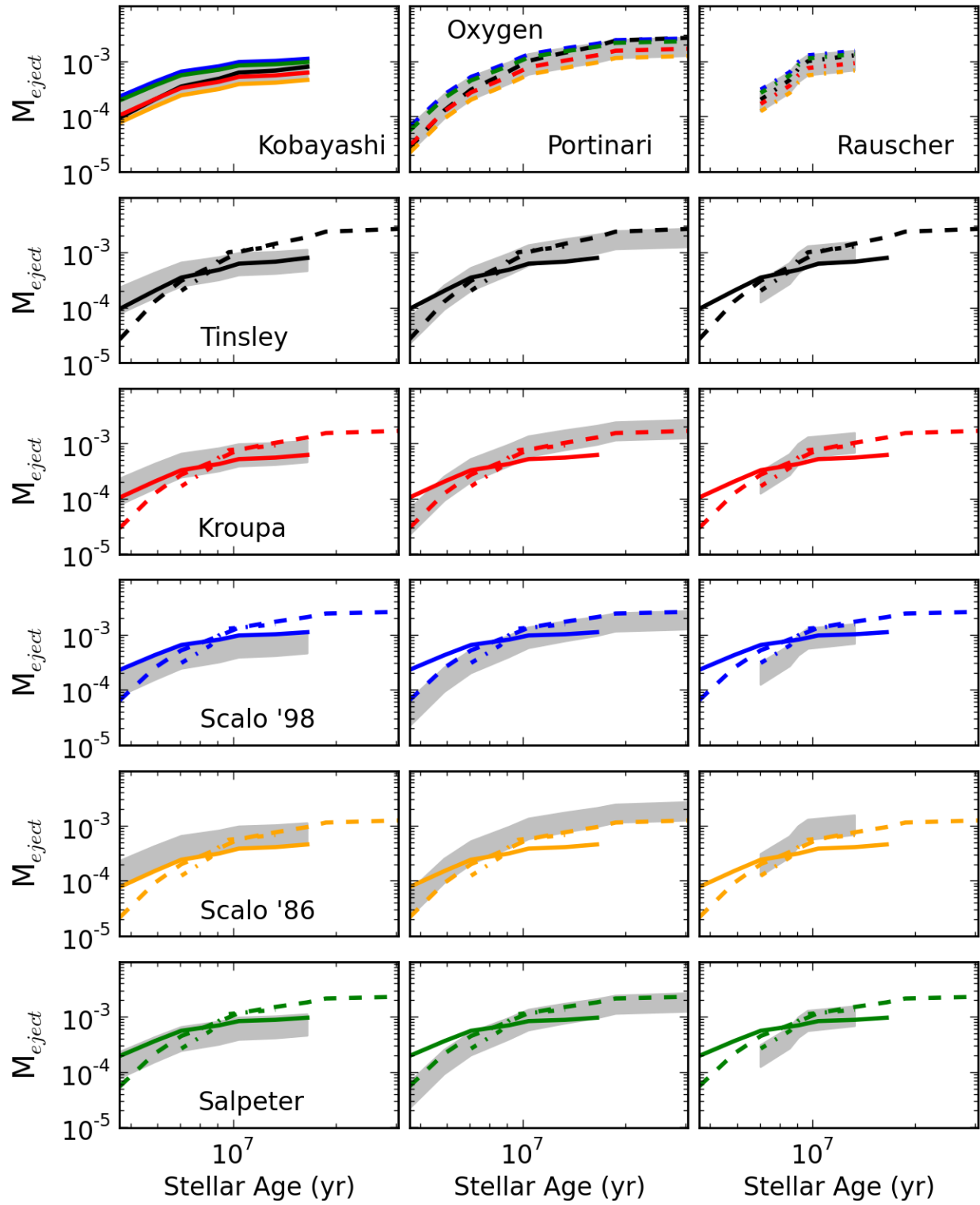


Figure 7.15: Same as Figure 7.1, but for the SNII Oxygen yields of Kobayashi et al. (2006), Portinari et al. (1998), and Rauscher et al. (2002)

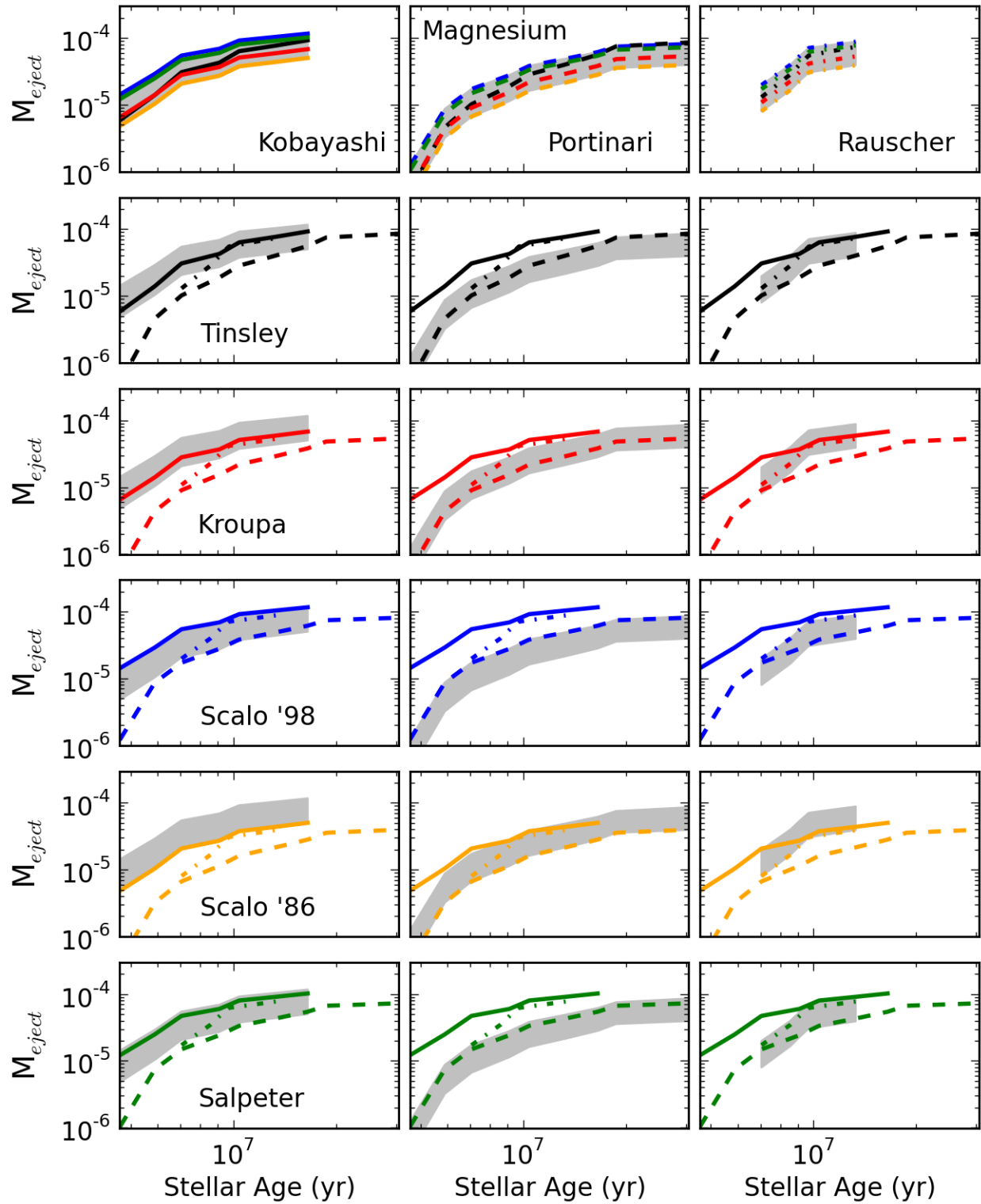


Figure 7.16: Same as Figure 7.1, but for the SNII Magnesium yields of Kobayashi et al. (2006), Portinari et al. (1998), and Rauscher et al. (2002)

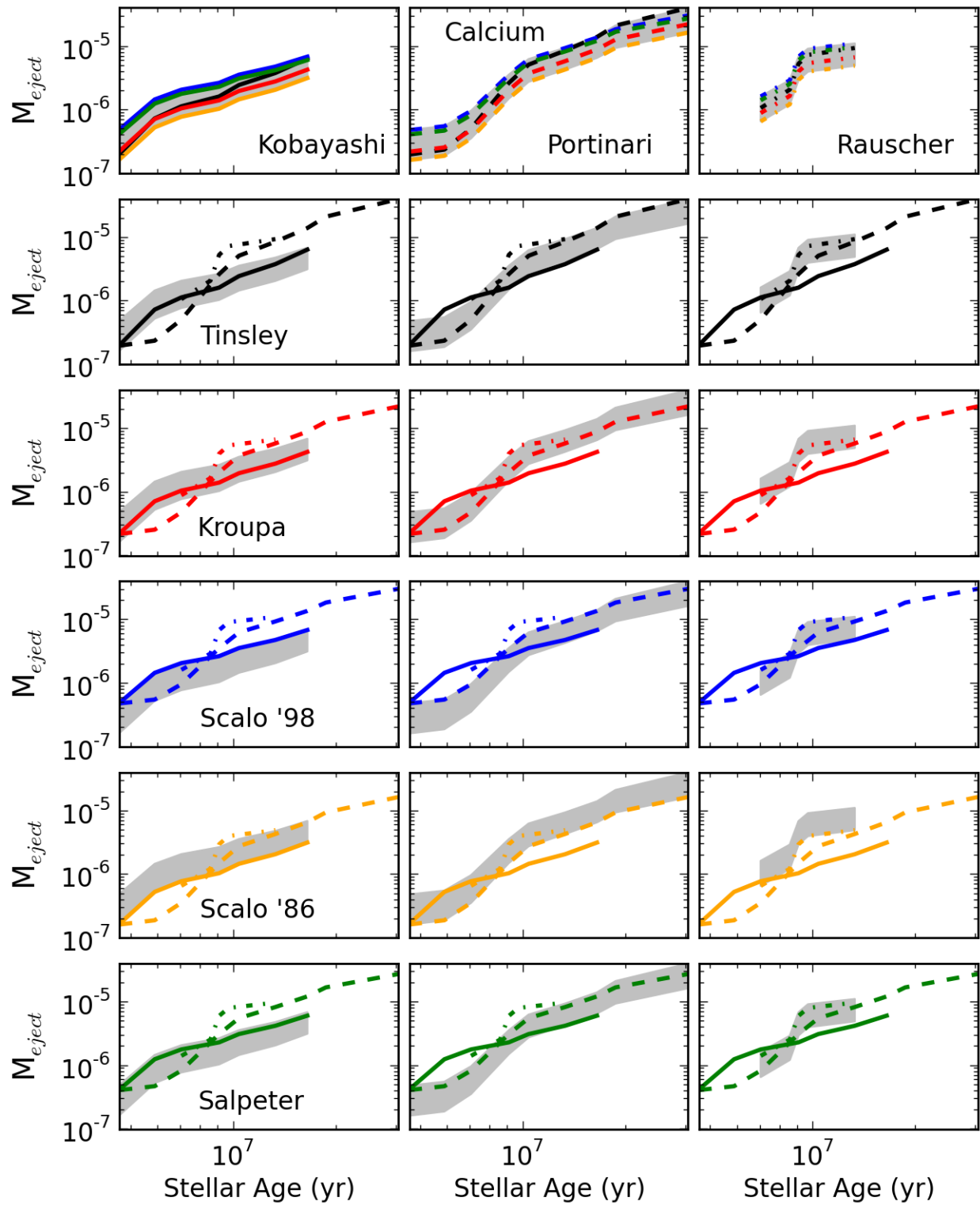


Figure 7.17: Same as Figure 7.1, but for the SNII Calcium yields of Kobayashi et al. (2006), Portinari et al. (1998), and Rauscher et al. (2002)

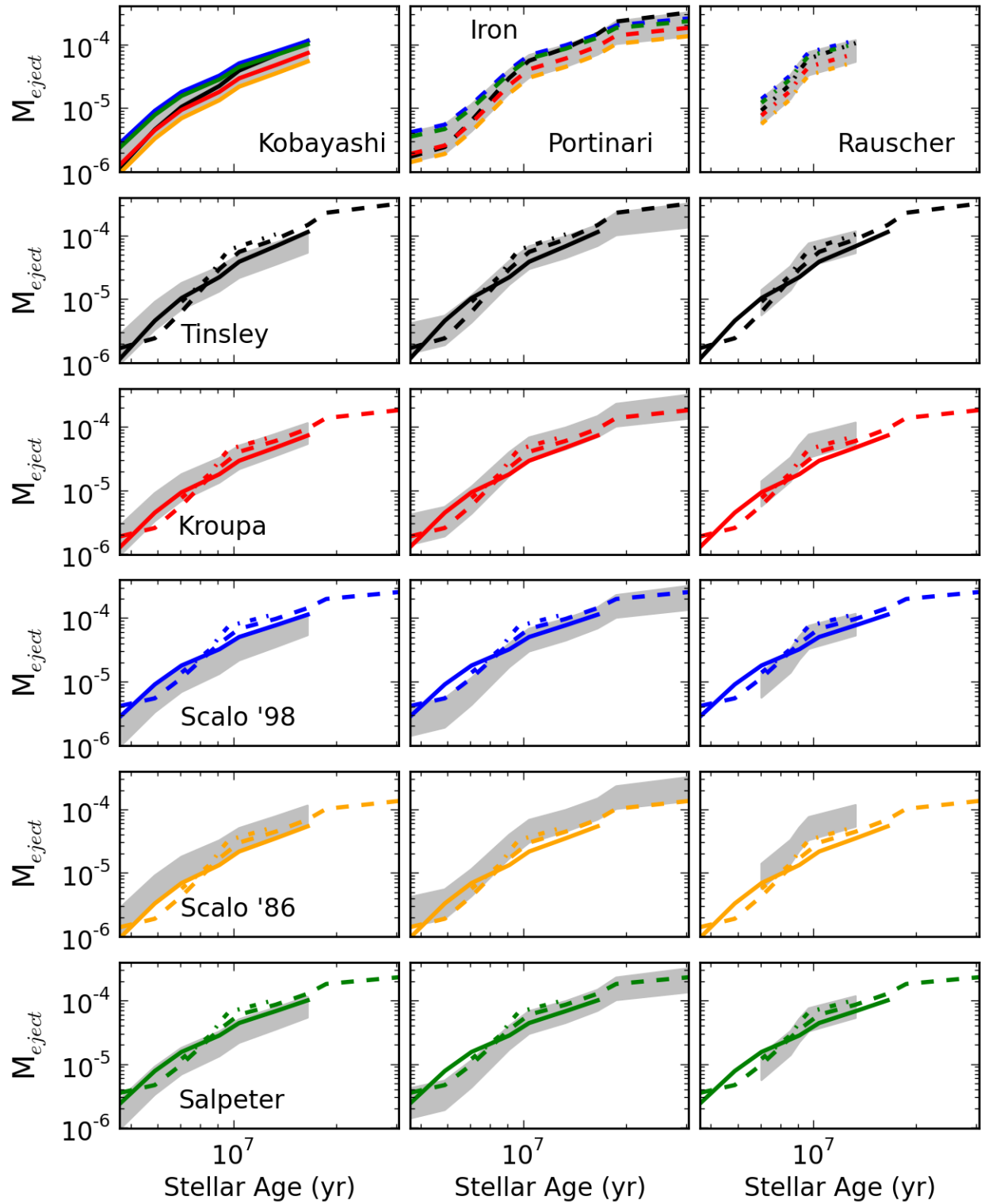


Figure 7.18: Same as Figure 7.1, but for the SNII Iron yields of Kobayashi et al. (2006), Portinari et al. (1998), and Rauscher et al. (2002)

BIBLIOGRAPHY

BIBLIOGRAPHY

Allende Prieto, C., et al. 2008, *Astronomische Nachrichten*, 329, 1018

Arnett, W. D. 1978, *ApJ*, 219, 1008

Baade, W. 1944, *ApJ*, 100, 137

Bastian, N., Covey, K. R., & Meyer, M. R. 2010, *ARA&A*, 48, 339

Beers, T. C. 1999, in *Astronomical Society of the Pacific Conference Series*, Vol. 165, *The Third Stromlo Symposium: The Galactic Halo*, ed. B. K. Gibson, R. S. Axelrod, & M. E. Putman, 202

Beers, T. C., Preston, G. W., & Shectman, S. A. 1985, *AJ*, 90, 2089

—. 1992, *AJ*, 103, 1987

Beers, T. C., et al. 2005, in *IAU Symposium*, Vol. 228, *From Lithium to Uranium: Elemental Tracers of Early Cosmic Evolution*, ed. V. Hill, P. Francois, & F. Primas, 175–183

Bennett, C. L., et al. 2003, *ApJS*, 148, 1

Benson, A. J. 2012, *ArXiv e-prints*, 17, 175

Boesgaard, A. M., & Steigman, G. 1985, *ARA&A*, 23, 319

Burbidge, E. M., Burbidge, G. R., Fowler, W. A., & Hoyle, F. 1957, *Reviews of Modern Physics*, 29, 547

Carollo, D., et al. 2012, *ApJ*, 744, 195

Cayrel, R., et al. 2004, *A&A*, 416, 1117

Chabrier, G. 2003, *PASP*, 115, 763

- Chieffi, A., & Limongi, M. 2004, *ApJ*, 608, 405
- Chiosi, C., & Caimmi, R. 1979, *A&A*, 80, 234
- Christlieb, N. 2003, in *Reviews in Modern Astronomy*, Vol. 16, *Reviews in Modern Astronomy*, ed. R. E. Schielicke, 191
- Dray, L. M., & Tout, C. A. 2003, *MNRAS*, 341, 299
- Dray, L. M., Tout, C. A., Karakas, A. I., & Lattanzio, J. C. 2003, *MNRAS*, 338, 973
- Elmegreen, B. G. 2009, in *The Evolving ISM in the Milky Way and Nearby Galaxies*
- Frebel, A. 2010, *Astronomische Nachrichten*, 331, 474
- Gallino, R., Arlandini, C., Busso, M., Lugaro, M., Travaglio, C., Straniero, O., Chieffi, A., & Limongi, M. 1998, *ApJ*, 497, 388
- Getman, K. V., Feigelson, E. D., Garmire, G., Broos, P., & Wang, J. 2007, *ApJ*, 654, 316
- Gómez, F. A., Coleman-Smith, C. E., O'Shea, B. W., Tumlinson, J., & Wolpert, R. L. 2012, *ApJ*, 760, 112
- Goriely, S., & Mowlavi, N. 2000, *A&A*, 362, 599
- Grebel, E. K., & Gallagher, III, J. S. 2004, *ApJ*, 610, L89
- Hartwick, F. D. A. 1976, *ApJ*, 209, 418
- Helmi, A., et al. 2006, *ApJ*, 651, L121
- Hillebrandt, W., & Niemeyer, J. C. 2000, *ARA&A*, 38, 191
- Hirschi, R., Meynet, G., & Maeder, A. 2005, *A&A*, 433, 1013
- Iwamoto, K., Brachwitz, F., Nomoto, K., Kishimoto, N., Umeda, H., Hix, W. R., & Thielemann, F.-K. 1999, *ApJS*, 125, 439
- Karakas, A., & Lattanzio, J. C. 2007, *PASA*, 24, 103

- Karakas, A. I. 2010, MNRAS, 403, 1413
- Kneller, J. P., & Steigman, G. 2004, New Journal of Physics, 6, 117
- Kobayashi, C., & Nomoto, K. 2009, ApJ, 707, 1466
- Kobayashi, C., Umeda, H., Nomoto, K., Tominaga, N., & Ohkubo, T. 2006, ApJ, 653, 1145
- Komatsu, E., et al. 2011, ApJS, 192, 18
- Komiya, Y., Suda, T., Minaguchi, H., Shigeyama, T., Aoki, W., & Fujimoto, M. Y. 2007, ApJ, 658, 367
- Kroupa, P. 2002, Science, 295, 82
- Limongi, M., & Chieffi, A. 2003, ApJ, 592, 404
- Lodders, K. 2003, ApJ, 591, 1220
- Maeder, A. 1992, A&A, 264, 105
- Marigo, P. 2001, A&A, 370, 194
- Matteucci, F., ed. 2001, Astrophysics and Space Science Library, Vol. 253, The chemical evolution of the Galaxy
- Matteucci, F., & Recchi, S. 2001, ApJ, 558, 351
- McConnachie, A. W., et al. 2009, Nature, 461, 66
- Meynet, G. 2008, in EAS Publications Series, Vol. 32, EAS Publications Series, ed. C. Charbonnel & J.-P. Zahn, 187–232
- Mo, H. J., & White, S. D. M. 2002, MNRAS, 336, 112
- Narayanan, D., & Davé, R. 2012, MNRAS, 423, 3601
- Neill, J. D., et al. 2007, in American Institute of Physics Conference Series, Vol. 924, The Multicolored Landscape of Compact Objects and Their Explosive Origins, ed. T. di Salvo, G. L. Israel, L. Piersant, L. Burderi, G. Matt, A. Tornambe, & M. T. Menna, 421–424

- Nissen, P. E., Chen, Y. Q., Asplund, M., & Pettini, M. 2004, *A&A*, 415, 993
- Nomoto, K., Iwamoto, K., Nakasato, N., Thielemann, F.-K., Brachwitz, F., Tsujimoto, T., Kubo, Y., & Kishimoto, N. 1997, *Nuclear Physics A*, 621, 467
- Nomoto, K., Tominaga, N., Umeda, H., Kobayashi, C., & Maeda, K. 2006, *Nuclear Physics A*, 777, 424
- Norman, M. L., Bryan, G. L., Harkness, R., Bordner, J., Reynolds, D., O'Shea, B., & Wagner, R. 2007, *ArXiv e-prints*
- Orban, C., Gnedin, O. Y., Weisz, D. R., Skillman, E. D., Dolphin, A. E., & Holtzman, J. A. 2008, *ApJ*, 686, 1030
- O'Shea, B. W., Bryan, G., Bordner, J., Norman, M. L., Abel, T., Harkness, R., & Kritsuk, A. 2004, *ArXiv Astrophysics e-prints*
- Portinari, L., Chiosi, C., & Bressan, A. 1998, *A&A*, 334, 505
- Press, W. H., & Schechter, P. 1974, *ApJ*, 187, 425
- Pritchett, C. J., Howell, D. A., & Sullivan, M. 2008, *ApJ*, 683, L25
- Pritzl, B. J., Venn, K. A., & Irwin, M. 2005, *AJ*, 130, 2140
- Raiteri, C. M., Villata, M., & Navarro, J. F. 1996, *A&A*, 315, 105
- Rauscher, T., Heger, A., Hoffman, R. D., & Woosley, S. E. 2002, *ApJ*, 576, 323
- Reeves, H. 1970, *Nature*, 226, 727
- Reimers, D. 1975, *Memoires of the Societe Royale des Sciences de Liege*, 8, 369
- Romano, D., Karakas, A. I., Tosi, M., & Matteucci, F. 2010, *A&A*, 522, A32
- Russell, S. C., & Dopita, M. A. 1990, *ApJS*, 74, 93
- Salpeter, E. E. 1955, *ApJ*, 121, 161

- Santoro, F., & Shull, J. M. 2006, *ApJ*, 643, 26
- Scalo, J. 1998, in *Astronomical Society of the Pacific Conference Series*, Vol. 142, *The Stellar Initial Mass Function (38th Herstmonceux Conference)*, ed. G. Gilmore & D. Howell, 201
- Scalo, J. M. 1986, in *IAU Symposium*, Vol. 116, *Luminous Stars and Associations in Galaxies*, ed. C. W. H. De Loore, A. J. Willis, & P. Laskarides, 451–466
- Scalo, J. M., Despain, K. H., & Ulrich, R. K. 1975, *ApJ*, 196, 805
- Schmidt, M. 1963, *ApJ*, 137, 758
- Schmidt, W., Ciaraldi-Schoolmann, F., Niemeyer, J. C., Röpke, F. K., & Hillebrandt, W. 2010, *ApJ*, 710, 1683
- Shetrone, M. D., Côté, P., & Sargent, W. L. W. 2001, *ApJ*, 548, 592
- Siess, L. 2006, *A&A*, 448, 717
- . 2007, *A&A*, 476, 893
- . 2010, *A&A*, 512, A10
- Smith, B. D., & Sigurdsson, S. 2007, *ApJ*, 661, L5
- Steigman, G. 2005, *Physica Scripta Volume T*, 121, 142
- Steinmetz, M. 2003, in *Astronomical Society of the Pacific Conference Series*, Vol. 298, *GAIA Spectroscopy: Science and Technology*, ed. U. Munari, 381
- Sullivan, M., et al. 2006, *ApJ*, 648, 868
- Sumiyoshi, K., Terasawa, M., Mathews, G. J., Kajino, T., Yamada, S., & Suzuki, H. 2001, *ApJ*, 562, 880
- Talbot, Jr., R. J., & Arnett, W. D. 1973, *ApJ*, 186, 51
- Tinsley, B. M. 1979, *ApJ*, 229, 1046

—. 1980, *Fund. Cosmic Phys.*, 5, 287

Travaglio, C., Gallino, R., Arnone, E., Cowan, J., Jordan, F., & Sneden, C. 2004, *ApJ*, 601, 864

Tumlinson, J. 2006, *ApJ*, 641, 1

Tumlinson, J. 2008, in *American Institute of Physics Conference Series*, Vol. 990, *First Stars III*, ed. B. W. O'Shea & A. Heger, 456–458

—. 2010, *ApJ*, 708, 1398

Umeda, H., & Nomoto, K. 2002, *ApJ*, 565, 385

van den Bergh, S. 1995, *AJ*, 110, 2700

van den Hoek, L. B., & Groenewegen, M. A. T. 1997, *A&AS*, 123, 305

van Dokkum, P. G. 2008, *ApJ*, 674, 29

Vassiliadis, E., & Wood, P. R. 1993, *ApJ*, 413, 641

Wanajo, S., & Ishimaru, Y. 2006, *Nuclear Physics A*, 777, 676

Williams, R. E., et al. 1996, *AJ*, 112, 1335

Wise, J. H., Turk, M. J., Norman, M. L., & Abel, T. 2012, *ApJ*, 745, 50

Woosley, S. E., Heger, A., & Weaver, T. A. 2002, *Rev. Mod. Phys.*, 74, 1015

Woosley, S. E., & Weaver, T. A. 1995, *ApJS*, 101, 181

Yanny, B., et al. 2009, *AJ*, 137, 4377

York, D. G., et al. 2000, *AJ*, 120, 1579